

# **Solar Photoelectrochemical Energy Conversion using Earth- Abundant Nanomaterials**

**by**

**Mark A. Lukowski**

A dissertation submitted in partial fulfillment of  
the requirements for the degree of

Doctor of Philosophy

(Chemistry)

at the

UNIVERSITY OF WISCONSIN-MADISON

2013

Date of final oral examination: July 18, 2013

The dissertation is approved by the following members of the Final Oral Committee:

Song Jin, Associate Professor, Chemistry  
Robert J. Hamers, Professor, Chemistry  
John C. Wright, Professor, Chemistry  
Mark Ediger, Professor, Chemistry  
Kyoung-Shin Choi, Professor, Chemistry

## Preface

# **Solar Photoelectrochemical Energy Conversion using Earth- Abundant Nanomaterials**

**Mark A. Lukowski, Ph.D.**

**University of Wisconsin-Madison 2013**

Using functional nanomaterials to make a meaningful impact in the real world requires an understanding of the structure-property relationships which directly influence the material's performance in its final application. My research has focused on the rational approach to synthesizing earth-abundant nanomaterials with applications in the generation of clean alternative fuels. Using analytical characterization tools and physical property investigations to complete the feedback-loop, we approach the optimization of these functional nanomaterials by aiming to understand their fundamental behavior while maximizing performance. Specifically, this work has revealed a particularly interesting concept where catalytic performance can be enhanced by controlling the phase behavior of the material. The following chapters describe the development of low-cost, earth-abundant layered metal chalcogenides as efficient catalysts for hydrogen evolution, and metal oxides having applications in the photoelectrochemical evolution of oxygen.

Chapter 1 serves as brief introduction to the basic concepts of the hydrogen and oxygen evolution reactions discussed in the general framework of electrocatalysis and photoelectrochemical (PEC) solar cells. A brief review of the pertinent literature lays the foundation of my unique approach to overcome the fundamental challenges limiting the performance of layered metal chalcogenides and hematite for clean fuel generation. Layered

metal chalcogenides are a particularly interesting family of materials that are structurally similar to layers of graphene in graphite. In their bulk forms, two-dimensional sheets are stacked together to form hexagonal structures held together by only weak van der Waals forces.

After developing a unique and highly tunable chemical vapor deposition method for the synthesis of molybdenum disulfide ( $\text{MoS}_2$ ) nanostructures, I used simple intercalation chemistry to induce subtle structural changes which have dramatic effects on the material properties (Chapter 2). In this example, the  $\text{MoS}_2$  nanostructures undergo a semiconductor-to-metallic phase transition. Using intercalation chemistry to influence phase behavior afforded the added advantage of chemically exfoliating the material into single sheets of the targeted metallic phase. Various analytical characterization techniques including diffraction, spectroscopy, and physical properties measurements confirmed the targeted phase transformation. By manipulating the polymorph behavior of  $\text{MoS}_2$ , I was able to significantly enhance the catalytic activity for the hydrogen evolution reaction, as reflected by 43 mV/decade Tafel slope.

The dramatic enhancement in catalytic activity exhibited by these chemically exfoliated  $\text{MoS}_2$  nanosheets is attributed to their modified electronic structure caused by the structural phase change. Moreover, the proliferation of catalytically active sites, simple loss-loss electrical integration of the catalyst, and more facile electrode kinetics further improves the performance. Additionally, I show the enhanced catalytic performance to be stable under extended operation conditions, even though the metallic phase is thermodynamically metastable. These previously unexploited features enable  $\text{MoS}_2$  as a highly competitive hydrogen evolution catalyst that could potentially replace platinum or other rare, expensive metals traditionally used in non-sustainable configurations.

Building upon the MoS<sub>2</sub> groundwork, I further extend my method for enhancing catalytic activity to other layered metal chalcogenides. Chapter 3 focuses on the catalytic performance from chemically exfoliated tungsten disulfide (WS<sub>2</sub>) nanosheets. Despite its structural similarities to MoS<sub>2</sub>, the behavior of WS<sub>2</sub> is surprisingly unique. Although WS<sub>2</sub> nanostructures could still be synthesized directly on conductive substrates like graphite, the violent chemical exfoliation reaction caused the material to delaminate from the substrates. To overcome these new challenges, I optimized our flexible methods to harvest the exfoliated nanosheets. Additionally, I sought to eliminate the cumbersome 48 h intercalation reactions used in the traditional preparation of the metallic nanosheets. This was accomplished using microwave chemistry. Amazingly, electrochemical tests show nearly equivalent catalytic performance for samples prepared in only 20 min using the microwave. More importantly, however, is the unprecedented performance exhibited by the chemically exfoliated WS<sub>2</sub> nanosheets. In a practical sense, the efficiency of a hydrogen evolution catalyst measured by the overpotential required to reach an electrocatalytic current density of 10 mA/cm<sup>2</sup>. Chemically exfoliated metallic WS<sub>2</sub> nanosheets achieve this benchmark at the low overpotential of -147 mV vs. RHE. To the best of our knowledge, this is the lowest reported potential required to reach 10 mA/cm<sup>2</sup> for any non-precious metal electrocatalyst.

Chapter 4 is an all-encompassing account of the detailed development of layered metal chalcogenides. Therein, I show the adaptability and generality of my modular synthetic method which is also used to grow molybdenum diselenide (MoSe<sub>2</sub>), tungsten diselenide (WSe<sub>2</sub>), and rhenium disulfide (ReS<sub>2</sub>). Though not shown here, the general applicability of my designed method has already been exploited by other members within the Jin group who are currently exploring MX<sub>2</sub> materials for novel heterostructures. Additionally, I explore various intercalation

methods used to target the metallic nanosheets of  $\text{MX}_2$  materials. I review the empirically determined strengths and weaknesses of (i) using n-butyllithium intercalation via conventional heating and microwave methods and (ii) employing electrochemically driven reactions within a battery coin cell using  $\text{LiPF}_6$  as a source of lithium. Additionally, I show electrocatalytic performance of the as-grown and chemically exfoliated nanosheets (produced from the different intercalation methods) for  $\text{MoS}_2$ ,  $\text{WS}_2$ ,  $\text{MoSe}_2$ ,  $\text{WSe}_2$ , and  $\text{ReS}_2$ , while emphasizing the most fruitful future directions where our materials can make an immediate impact. In a related appendix (Appendix 3), I show the preliminary electrocatalytic hydrogen evolution performance from cobalt disulfide ( $\text{CoS}_2$ ).  $\text{CoS}_2$  is a structurally distinct (pyrite structure-type) compound that has been previously used for polysulfide reduction, but not much is known about its hydrogen evolution properties. This represents another new direction within the group where we are exploring the overlap in enhanced catalytic activity across different chemistries.

Lastly, I report an improved synthesis for high aspect-ratio hematite nanowires (NWs) and develop a unique post-grown doping method to significantly improve their electrical transport properties (Chapter 5). Hematite, also known as  $\alpha\text{-Fe}_2\text{O}_3$  or rust, is a particularly attractive material with applications as a photoanode in a photoelectrochemical cell. By using shot-peening to increase the density of defects within metal foil growth substrates, my simple and rational thermal oxidation method improves the density and uniformity of hematite NWs while significantly reducing required reaction times (60 min vs. 2 days). Though as-synthesized hematite is a notoriously poor semiconductor, I also developed a simple post-growth method for doping these iron oxide NWs with silicon. Using lithographically defined single NW devices, I confirm the doping method results in a dramatic improvement in electrical conductivity (4 orders of magnitude). Although other practical considerations limit their application as a photoanode,

these general methods and findings have been important in helping to optimize the PEC performance of solution synthesized hematite NWs within the Jin group.

The body of work presented here directly addresses the growing interest in developing alternative energies for clean power generation. By developing a simple but unique method, I have shown that earth-abundant  $\text{MX}_2$  nanosheets are highly competitive catalysts for hydrogen evolution. Additionally, I have also explored the development of cost-effective hematite photoanodes for the photoelectrochemical generation of oxygen. This work represents a strong foundation and provides a flexible approach for the continued research on  $\text{MX}_2$  (and other) materials with broad-ranging properties and applications. Throughout my graduate career, I have strived to develop new and optimized synthetic methods to enable the high-performance of earth-abundant materials by taking an interdisciplinary approach without forsaking the fundamentals governing their behavior.

## Acknowledgements

The journey to earning a Ph.D. is anything but a solitary endeavor. Although the degree is awarded to an individual, a Ph.D. truly belongs to the many people who helped shape its pursuit and shared the unique experiences along the journey.

Most importantly, I thank my family for their unconditional support and encouragement. There is no question that they are the reason why I am in this position today. My sister, Alexa, has been more helpful than she probably realizes and my father, Ted, has set an excellent example of work ethic to which I can only aspire. I owe my mother, Shirley Lukowski, an especially large debt of gratitude. She has always been the most influential person in my life and the source of my motivation. Without a doubt, she is the strongest person I know, and I am proud to say that I am her son. I also owe a great deal of thanks to my grandparents, Roy and Delores Wolf, my Aunt Connie Parker, and my cousins Tim, Cathy, and Lori for helping to take care of me when I was younger.

I also want to extend my sincerest gratitude to my advisor, Song Jin, whose limitless creative energy has motivated me to learn more about science than I ever expected and helped shape me into the scientist I am today. I also owe an enormous amount of thanks to my wonderful undergraduate research advisor, Maria Milletti, who not only gave me the opportunity to be a part of a research group, but also convinced me to pursue a Ph.D. I have no doubt that that my undergraduate research experience was the most important factor in preparing me for graduate school. To that end, I also thank Theodore Provder and John Texter, for their guidance while working under their tutelage at the EMU's Coatings Research Institute. I also owe many thanks to Andrei Kornilov and my co-workers at Cayman Chemical Company in Ann Arbor,

especially Jeffrey Williams and Joe Colombo. Those 16 months I spent working in an industrial lab were amazingly positive and influential.

I have always taken pride in being a part of the Jin Group, thanks in large part to the character of the people with whom I work. I also need to thank my current and former lab-mates who have significantly contributed to my education. Particularly, Dr. Matt Bierman, Dr. Andy Schmitt, Dr. Jeremy Higgins, and Dr. Steve Morin deserve special mention for helping me started when I joined the Jin group. In addition to being exemplary graduate students, these gentlemen are still my close friends with whom I hope to continue personal and professional relationships. I would also like to thank the group members with whom I have collaborated, especially Dr. Rachel Selinsky, Dr. Jeannine Szczech, Jack DeGrave, Matt Faber, Fei Meng, Linsen Li, Audrey Forticaux, and Kyle Czech. I owe a special debt of gratitude to Professor John Wright and Professor Bob Hamers, who have both been amazing sources of fresh ideas and encouragement. I would also like especially thank Andrew Daniel, my outstanding undergraduate who has a bright future ahead of him. I hope your experience and newly acquired skills outweigh any of the hardships endured during my education as a manager. I also want to express my gratitude to Dr. Rob McClain, Tracy Drier, the staff of the machine shop, especially Kendall and Rick, and the staff in the electronics shop who all keep this Department running.

Finally, I thank my closest friends who have made my time in Wisconsin truly memorable. I am especially thankful for Stefanie Massignan, who has made an immeasurable positive impact in the quality of my life, and deserves special recognition for dealing with me through the ups and downs of graduate school. I also want to thank fellow graduate student, Katie Whitaker, with whom I have enjoyed countless conversations, many of which were shared over a few pints of beer. I truly could not imagine my time in Wisconsin without you, and I

wish you all the best luck in the future. I also wish to thank my closest friends, Cailan Harper, Holly Hardge, Gabe Haber, and Tyler Schloss. Though none of you live in Wisconsin, some of the best memories of my time here were forged during your visits. You guys are, and always will be, family to me. Finally, I want to take the opportunity to remember my friend and colleague, Michael McCoy. We all miss you, and although the world isn't the same without you, it's definitely a better place because of the time you were here.

And lastly, thank you to the reader for taking the time to recognize this list of people important to me.

Mark A. Lukowski, 10 July 2013

## Table of Contents

<b>Preface</b>	i
<b>Acknowledgements</b>	vi
<b>Table of Contents</b>	ix
<b>List of Tables</b>	xi
<b>List of Figures</b>	xii
<b>Chapter 1: Concepts of Water Splitting: The Electrocatalytic Hydrogen Evolution Reaction and the Photoelectrochemical Generation of Oxygen using Earth-Abundant Nanomaterials</b>	1
<b>Chapter 2: Enhanced Hydrogen Evolution Catalysis from Chemically Exfoliated Metallic MoS<sub>2</sub> Nanosheets</b>	27
<b>Chapter 3: Exceptional Catalytic Hydrogen Evolution from Metallic WS<sub>2</sub> Nanosheets</b>	55
<b>Chapter 4: The Synthetic Development of Metal Chalcogenides and Exploration of Various Methods to Control their Phase Behavior</b>	79
<b>Chapter 5: Improved Synthesis and Electrical Properties of Si-Doped <math>\alpha</math>-Fe<sub>2</sub>O<sub>3</sub> Nanowires</b>	119
<b>Appendix 1: Supporting Information for Chapter 2</b>	150
<b>Appendix 2: Supporting Information for Chapter 3</b>	160

**Appendix 3: Preliminary Results for the Application of CoS<sub>2</sub> for Hydrogen**

166

Evolution Catalysis

**List of Tables**

<b>Table 4.1.</b> Tabulated structural parameters and physical properties for a representative group of layered metal chalcogenide materials	83
---	----

## List of Figures

<b>Figure 1.1.</b> The Sabatier plot for HER catalysts.	5
<b>Figure 1.2.</b> The role of active edge sites in HER catalysis	9
<b>Figure 1.3.</b> Polymorphism in layered metal chalcogenides	12
<b>Figure 1.4.</b> Schematic illustration of an idealized tandem device for water splitting	14
<b>Figure 1.5.</b> Band-energy diagram for PEC water splitting using a single electrode	16
<b>Figure 1.6.</b> Tandem-cell designs and possibilities	18
<b>Figure 1.7.</b> Strategies to improve the PEC performance of hematite photoanodes	21
<b>Figure 2.1.</b> Structural differences in MoS <sub>2</sub> polymorphs	30
<b>Figure 2.2.</b> The growth of MoS <sub>2</sub> nanostructures on various substrates	35
<b>Figure 2.3.</b> SEM and TEM characterization of as-grown MoS <sub>2</sub> nanostructures	36
<b>Figure 2.4.</b> Raman, PXRD, and CSAFM characterization of as-grown and chemically exfoliated MoS <sub>2</sub> nanosheets	38
<b>Figure 2.5.</b> SEM and TEM characterization of chemically exfoliated MoS <sub>2</sub> nanosheets	41
<b>Figure 2.6.</b> Electrocatalytic performance of 1T-MoS <sub>2</sub> nanosheets and 2H-MoS <sub>2</sub> nanostructures	44
<b>Figure 2.7.</b> Optimizing the electrocatalytic performance of 1T-MoS <sub>2</sub> nanosheets as a function of intercalation conditions	46
<b>Figure 2.8.</b> Electrocatalytic stability of chemically exfoliated MoS <sub>2</sub> nanosheets	49
<b>Figure 2.9</b> Long-term stability studies of 1T-MoS <sub>2</sub> nanosheets	51

<b>Figure 3.1.</b> Experimental approach and characterization of as-grown and chemically exfoliated WS <sub>2</sub> nanosheets	62
<b>Figure 3.2.</b> XPS, UPS, and CSAFM characterization of 1T- and 2H-WS <sub>2</sub>	66
<b>Figure 3.3.</b> Electrocatalytic performance of as-grown and chemically exfoliated WS <sub>2</sub> nanosheets	68
<b>Figure 3.4.</b> Optimizing the electrocatalytic performance of 1T-WS <sub>2</sub> nanosheets as a function of microwave intercalation duration	71
<b>Figure 3.5.</b> The superior catalytic activity of 1T-WS <sub>2</sub> nanosheets derived from CVD grown nanostructures	73
<b>Figure 3.6.</b> Electrocatalytic stability of 1T-WS <sub>2</sub> nanosheets	75
<b>Figure 4.1.</b> Polymorph behavior in MX <sub>2</sub> materials	82
<b>Figure 4.2.</b> SEM images of as-grown MX <sub>2</sub> nanostructures	92
<b>Figure 4.3.</b> TEM characterization of as-grown MoS <sub>2</sub> , WS <sub>2</sub> , and WSe <sub>2</sub> nanostructures	94
<b>Figure 4.4.</b> SEM and TEM characterization of 1T-MoS <sub>2</sub> and 1T-WS <sub>2</sub>	96
<b>Figure 4.5.</b> PXRD characterization of as-grown and chemically exfoliated MX <sub>2</sub> materials	98
<b>Figure 4.6.</b> Raman characterization of as-grown and chemically exfoliated MX <sub>2</sub> materials	100
<b>Figure 4.7.</b> Electrocatalytic performance of 1T-MoS <sub>2</sub> nanosheets produced by various methods for the chemical intercalation of n-butyllithium	103

<b>Figure 4.8.</b> Electrocatalytic performance of 1T-MoS <sub>2</sub> nanosheets produced by electrochemical intercalation of LiPF <sub>6</sub>	104
<b>Figure 4.9.</b> Electrocatalytic performance of 1T-WS <sub>2</sub> nanosheets produced by various methods for the chemical intercalation of n-butyllithium	107
<b>Figure 4.10.</b> Electrocatalytic performance of 1T-WS <sub>2</sub> nanosheets produced by electrochemical intercalation of LiPF <sub>6</sub>	108
<b>Figure 4.11.</b> Electrocatalytic performance of as-grown and chemically exfoliated MoSe <sub>2</sub> nanosheets	110
<b>Figure 4.12.</b> Electrocatalytic performance of as-grown and chemically exfoliated WSe <sub>2</sub> nanosheets	112
<b>Figure 4.13.</b> Electrocatalytic performance of as-grown ReS <sub>2</sub> nanostructures	114
<b>Figure 5.1.</b> SEM characterization of as-grown hematite NWs	126
<b>Figure 5.2.</b> Morphology control over hematite nanostructures	129
<b>Figure 5.3.</b> PXRD of hematite NWs	132
<b>Figure 5.4.</b> HRTEM characterization of as-grown hematite NWs	134
<b>Figure 5.5.</b> Electrical transport properties of as-grown and Si-doped hematite NWs	137
<b>Figure 5.6.</b> TEM characterization of Si-doped hematite NWs	142
<b>Figure 5.7.</b> EDS elemental mapping of Si-doped hematite NWS	144
<b>Figure A1.1.</b> CSAFM characterization of as-grown and chemically exfoliated MoS <sub>2</sub> nanosheets	152

<b>Figure A1.2.</b> Electron diffraction of 1T-MoS <sub>2</sub> nanosheets compared to 2H-MoS <sub>2</sub> nanostructures	155
<b>Figure A1.3.</b> <i>iR</i> -corrected catalytic activity of 1T-MoS <sub>2</sub> nanosheets	157
<b>Figure A1.4.</b> Using cyclic voltammetry to estimate relative differences in electrochemically active surface area	159
<b>Figure A2.1.</b> X-ray photoelectron spectra of the Au <i>4f</i> and C <i>1s</i> edges	161
<b>Figure A2.2.</b> CSAFM characterization of as-grown and chemically exfoliated WS <sub>2</sub> nanosheets	163
<b>Figure A2.3.</b> Comparison of electrochemical activity in 1T-WS <sub>2</sub> nanosheets isolated by various method	165
<b>Figure A3.1.</b> Characterization of as-sulfidized nanostructured CoS <sub>2</sub> film	169
<b>Figure A3.2.</b> Electrocatalytic HER performance of as-sulfidized nanostructured CoS <sub>2</sub> film	171

## Chapter 1

# Concepts of Water Splitting: The Electrocatalytic Hydrogen Evolution Reaction and the Photoelectrochemical Generation of Oxygen using Earth-Abundant Nanomaterials

### 1.1 Abstract

Although the vast majority of energy consumed worldwide is derived from fossil fuels, the growing interest in making cleaner alternative energies more economically viable has motivated recent research efforts aimed to make significant advances in solar, wind, and biomass power generation. Clean power generation also requires clean burning fuels, such as  $H_2$  and  $O_2$ , so that energy can still be provided on demand at night or in calm wind conditions. Herein we introduce the basic concepts of water splitting broken down into the hydrogen evolution and oxygen evolution reactions, and discuss the required materials properties needed to operate these reactions efficiently. We discuss the advantages of using earth-abundant, non-toxic nanomaterials as the platform for cost-effective and sustainable clean fuel production. Specifically, we introduce the layered metal chalcogenide family of materials for electrocatalytic hydrogen evolution and hematite photoanodes for photoelectrochemical oxygen evolution.

## 1.2 Introduction

Global environmental and economic factors drive the contemporary research toward harnessing alternative energy and fuels.<sup>1,2</sup> Solar conversion is a particularly appealing energy source,<sup>3</sup> although wind farms and biomass also play a significant role in clean power generation. Regardless of the approach to generate clean electricity, we also require the ability to store this energy to meet demands of continuous supply. Storing this energy in the form of “green” fuels, like H<sub>2</sub> and O<sub>2</sub>, is an attractive solution to this problem.<sup>4</sup> The splitting of water can be broken down into the hydrogen evolution reaction (HER) and the oxygen evolution reaction (OER). Although high-performance photoelectrochemical (PEC) systems based on single-crystalline III-V semiconductors have been demonstrated at the laboratory scale,<sup>5,6</sup> their practical applications are limited due to their use of rare, expensive elements or their chemical instability. Alternative research efforts directed at shifting commercial electrolysis units to run in acidic electrolytes are currently limited in part by the reliance on platinum (or other expensive, precious metals) as the cathode catalyst. Replacing these rare and expensive materials with stable, earth-abundant compounds would represent a significant step toward making hydrogen a competitive alternative energy source and facilitate the transition to the hydrogen economy.<sup>2,7</sup> Herein we introduce the basic concepts of the electrocatalytic HER and photoelectrochemical generation of oxygen with an emphasis on using earth-abundant materials such as layered metal chalcogenides and  $\alpha$ -Fe<sub>2</sub>O<sub>3</sub> (hematite).

## 1.3 The Hydrogen Evolution Reaction

The hydrogen evolution reaction (HER) is perhaps the most studied electrochemical reaction and is often used as the textbook example for relating the kinetics and surface properties of

electrodes.<sup>8</sup> With applications in electrodeposition, corrosion, and fuel production, the HER is both scientifically and commercially interesting. The HER is a simple reaction where two protons and two electrons combine to form H<sub>2</sub>.



The mechanism of hydrogen evolution is broken down into elementary steps that define the catalytic operation of the electrode. Here we present the pertinent reactions for hydrogen evolution in acidic media. The initial reaction, named the Volmer reaction, involves the adsorption of a free proton to an active site (denoted by an asterisk) with the transfer of an electron.



The subsequent step where hydrogen is evolved can proceed via the Tafel or Heyrovsky reaction. The Tafel reaction involves two adjacently adsorbed H atoms reacting associatively to form H<sub>2</sub>.



The Heyrovsky reaction involves the direct reaction of an adsorbed proton with another free proton and electron.



The Volmer reaction, where a proton is adsorbed to an active site, is often the rate limiting step for non-precious metal catalysts.<sup>9</sup> To this end, one method of predicting the catalytic activity of a material is to calculate the free energy of hydrogen binding using density functional theory. Ideally, the change in free energy for the hydrogen adsorption should be close to equilibrium ( $\Delta G = 0$ ) since the catalyst should neither hold onto the adsorbed proton too strongly

nor require a large driving force to initiate the reaction. The exchange current density ( $j_0$ ), which is explained in detail elsewhere,<sup>9</sup> is another important parameter governing the overall catalytic performance that may be simply viewed as the electron-transfer rate of the catalyst. Plotting the exchange current density against the free energy of proton adsorption results in the Sabatier plot<sup>10</sup> (Figure 1.1), where the most active catalysts for the HER lie at the top of the “volcano” curve. Unfortunately these catalysts, such as platinum (which is known to be best catalyst for hydrogen evolution in acidic media), are also among the most expensive and rarest of materials found on Earth.

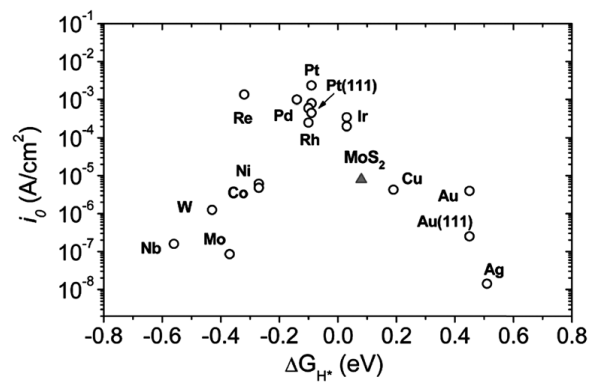


**Figure 1.1.** The Sabatier plot for HER catalysts showing the exchange current densities plotted against the free energy of hydrogen adsorption. Materials near the top of the volcano curve are expected to be most active in the HER.<sup>10</sup>

Determining the exact reaction pathway followed by a given catalyst is not always simple; in fact, both the Volmer-Tafel and Volmer-Heyrovsky mechanisms can operate at the same time. Further analysis of electrocatalytic behavior using Tafel plots can sometimes shed light onto the predominating mechanism. Starting from first principles and electrochemical definitions, it can be shown that the observed current for a reaction may be expressed by the Butler-Volmer equation, which takes into account both the cathodic and anodic processes.

$$i = i_0 \left[ e^{-\alpha n f \eta} - e^{(1-\alpha) n f \eta} \right] \quad (\text{EQ 1.5})$$

Here,  $i_0$  is the exchange current density,  $\alpha$  is the transfer coefficient (which reflects the symmetry of the energy barrier),  $f$  is Faraday's constant divided by product of the universal gas constant and absolute temperature ( $F/RT$ ),  $n$  is the number of electrons transferred, and  $\eta$  is the overpotential applied. For sufficiently large negative potentials ( $\eta > 118 \text{ mV}$ ), the anodic term becomes negligible, and the relationship can be simplified.<sup>8</sup>

$$i = i_0 e^{-\alpha n f \eta} \quad (\text{EQ 1.6})$$

Rearranging this simplified equation to reflect the linear relationship between the overpotential and the current, we obtain the cathodic Tafel equation.

$$\eta = \frac{RT}{\alpha n F} \ln(i_0) - \frac{RT}{\alpha n F} \ln(i) \quad (\text{EQ 1.7})$$

However, the Tafel equation is often written in a more simple empirical form.

$$\eta = a + b \log(i) \quad (\text{EQ 1.8})$$

Here, we recognize the empirical constants are identified from theory as

$$a = \frac{2.3RT}{\alpha n F} \log(i_0) \quad \text{and} \quad b = -\frac{2.3RT}{\alpha n F} \quad (\text{EQ 1.9})$$

The transfer coefficient, which generally takes values between 0 and 1, is generally estimated to be  $\alpha = 0.5$ .<sup>11</sup> Using this assumption, it can be shown that theoretical Tafel slopes of approximately 118 mV/decade, 30 mV/decade, or 40 mV/decade should be expected if the Volmer, Tafel, or Heyrovsky reaction, respectively, is the limiting step in the HER. It is important to note, however, that exact interpretations of the Tafel slope require the correct value of  $\alpha$ , which may differ by up to 20% from the normal estimated value of 0.5.<sup>12</sup> To avoid any ambiguity or errors associated with the extrapolation of exchange current densities, practical comparisons of HER catalysts are generally made using Tafel slopes and the electrocatalytic current drawn at a given overpotential.<sup>13</sup>

## **1.4 Layered Metal Chalcogenides as HER catalysts**

### **1.4.1 Background and early studies**

Layered metal chalcogenides are an exciting family of compounds with a broad range of traditional and envisioned applications.<sup>11,13-15</sup> These materials are composed of two dimensional (2D) layers stacked to form hexagonal structures held together by only weak van der Waals interactions. Having the general  $\text{MX}_2$  formula, where M is a metal (Mo, W, etc.) and X is a chalcogen (S, Se, etc.), most of these compounds are found in their semiconducting and thermodynamically favored 2H polymorph, which is built from edge-sharing trigonally prismatic  $\text{MX}_6$  units. Perhaps best represented by  $\text{MoS}_2$ , these materials have been well characterized for their high activity in hydrodesulfurization (HDS) catalysis.<sup>16</sup> However, natural single crystals of  $\text{MoS}_2$  were also shown to be active for electrochemical hydrogen evolution in the 1970s.<sup>17</sup> DFT calculations predicted the edges of the 2D sheets to be responsible for the catalytic activity.<sup>18</sup> Specifically, the (1010) Mo edges with 50% sulfur adsorption were predicted to be the most

catalytically active since the free energy of hydrogen adsorption was predicted to be most similar to platinum ( $\Delta G_{\text{H}_{\text{ads}}} = \sim 0 \text{ eV}$ ). This was later confirmed by direct measurement using scanning tunneling microscopy (STM) where the edges of nanoplatelets appear as bright rims, suggesting their more catalytically active nature (Figure 1.2).<sup>10</sup> Furthermore, the catalytic activity was shown to conclusively depend directly on the edge length but exhibited no clear relationship with the area coverage.

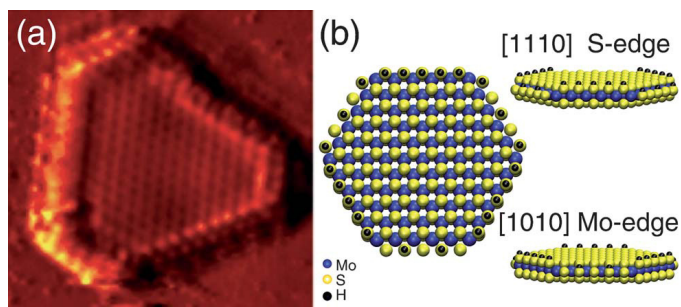


**Figure 1.2.** (a) STM of MoS<sub>2</sub> nanoplates on Au [111] showing the bright rim around the edges, corresponding to the catalytically active edge sites. (b) Molecular representations of a MoS<sub>2</sub> nanoplate where both Mo and S edges are exposed. <sup>10</sup>

### 1.4.2 Recent developments in MoS<sub>2</sub> and WS<sub>2</sub> nanomaterials for hydrogen evolution

With the understanding that catalytic activity is directly related to the number of active edge sites, the application of MoS<sub>2</sub> and other MX<sub>2</sub> materials for hydrogen evolution has become a popular research interest.<sup>11,13</sup> Nanostructuring MX<sub>2</sub> materials to increase the density of active edge sites have been the most popular approach to improving its catalytic activity for the HER. While the poor catalytic activity of bulk single crystals is reflected by its ~690 mV/decade Tafel slope, Jaramillo and co-workers reported Tafel slopes of 55-60 mV/decade for their MoS<sub>2</sub> nanoplates.<sup>10</sup> Bonde *et al.* reported the HER activity of MoS<sub>2</sub> and WS<sub>2</sub> nanoparticulates on a carbon support, where Tafel slopes of 120 and 135 mV/decade were observed for MoS<sub>2</sub> and WS<sub>2</sub>, respectively.<sup>19</sup> Bonde also showed an improvement in catalytic activity after “cobalt promotion,” which is expected to further reduce the  $\Delta G$  of hydrogen adsorption. Chen and co-workers reported core-shell nanowires with conductive substoichiometric MoO<sub>3</sub> cores and conformal MoS<sub>2</sub> shells exhibiting Tafel slopes of 50-60 mV/decade after *iR* corrections.<sup>20</sup> Later, the same group reported the complex template-directed synthesis of MoS<sub>2</sub> in a double gyroid phase with Tafel slopes reaching 50 mV/decade after correction for significant Ohmic losses.<sup>21</sup>

Li and co-workers reported the growth of MoS<sub>2</sub> nanoclusters with a high density of edges synthesized directly on reduced graphene oxide (rGO) nanosheets.<sup>22</sup> The direct connection to the conductive rGO substrate likely improves the charge-transfer kinetics from the MoS<sub>2</sub> catalysts, resulting in an impressive 41 mV/decade Tafel slope. Electrochemically deposited MoS<sub>x</sub> catalysts also show excellent catalytic activity for the HER, although the materials are less understood. Merki *et al.* saw onsets of catalytic activity at -0.1 V vs. RHE and a 40 mV/decade Tafel slope,<sup>23</sup> while Benck *et al.* observed ~60 mV/decade Tafel slopes.<sup>24</sup> Moreover, high catalytic activity from MoS<sub>x</sub> nanoparticles grown on graphene coated Ni foams was recently

reported by Chang and co-workers where they observed a 43 mV/decade Tafel slope.<sup>25</sup> The interesting chemistry of hydrogen evolution from  $\text{MX}_2$  materials has even inspired the design of molecular mimics. Karunadasa *et al.* recently reported the synthesis of a well-defined  $\text{Mo}^{\text{IV}}$ -disulfide inorganic compound where disulfide terminated edges mimic the edge sites of traditional  $\text{MoS}_2$  catalysts.<sup>26</sup> Jaramillo and co-workers have also designed incomplete cubane-type  $[\text{Mo}_3\text{S}_4]^{4+}$  molecules for hydrogen evolution.<sup>27</sup> While these systems still require further study, their strength lies in the modular nature of their chemistry that can be exploited in the rational approach to design powerful molecular catalysts.

### 1.4.3 Outlook and future directions for $\text{MX}_2$ electrocatalysts

Although these briefly reviewed publications reflect the significant advances aimed to improve the electrocatalytic activity of  $\text{MX}_2$  for the HER, many of these general approaches fall victim to the intrinsic limitations of 2H- $\text{MX}_2$  materials which exhibit anisotropic conductivity and potentially limiting reactivity of the active sites present.<sup>11</sup> In order to make  $\text{MX}_2$  materials truly competitive HER catalysts, these issues must be solved. We overcome these challenges by controlling their nanostructured synthesis and structural polymorphs using simple intercalation chemistry.<sup>28</sup> Electron transfer from intercalated alkali metals, such as lithium, destabilize the more thermodynamically favored trigonally prismatic phases (2H- and 3R) and facilitate the structural transition to the 1T phase,<sup>29,30</sup> which is built from edge-sharing  $\text{MX}_6$  octahedra (Figure 1.3).

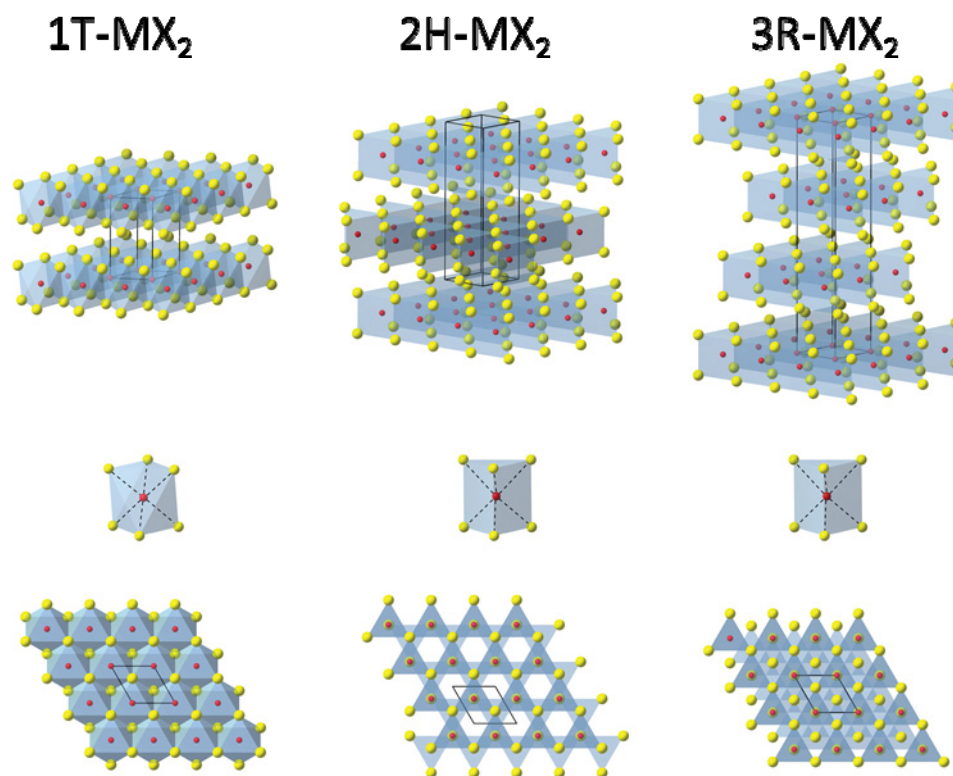


**Figure 1.3.** Crystal structure models illustrating the differences between the 1T-, 2H-, and 3R-MX<sub>2</sub> polymorphs, highlighting the octahedral and trigonal prismatic coordination and of the metal atoms. Projection along the *c*-axis reveals further contrast between the polymorphs. The 1T-MX<sub>2</sub> structure model was drawn using the crystallographic coordinates for the 1T-TiS<sub>2</sub>.

Removal of the intercalated lithium by forced hydration causes the chemical exfoliation of the material into single nanosheets, which are still predominantly comprised of the metastable 1T polymorph. These subtle structural changes have a dramatic affect on the physical properties, as the 1T polymorph is known to be metallic. Our recent work shows that this 1T phase exhibits significantly enhanced catalytic activity for the HER due to its proliferated density of active sites, metallic conductivity, and facile electrode kinetics.<sup>28</sup> A recent report from the Chhowalla group using a similar approach further corroborates our conclusions.<sup>31</sup> These unique characteristics, which have not been previously exploited until our MoS<sub>2</sub> work, are attributed to the electronic structure modification that accompanies the structural transition, and results in the  $\Delta G$  for hydrogen adsorption moving even closer to zero. We have explored multiple intercalation chemistries, including electrochemically driven reactions and microwave heating) to refine and optimize our approach to controlling the polymorph behavior of MX<sub>2</sub> compounds. Our more recent work focusing on MoSe<sub>2</sub> and WS<sub>2</sub> confirm the enhanced catalytic activity of the 1T phase is a general phenomenon and not limited to the specific case of MoS<sub>2</sub>.

These more catalytically active materials, which we have shown to be stable at ambient conditions during extended operation, can also be used in photocatalysis.<sup>32-34</sup> Moving forward, the direct utilization of sunlight to drive the electrocatalytic evolution of hydrogen is especially attractive to further reduce waste and cost. We believe our chemically exfoliated, metallic 1T-MX<sub>2</sub> nanosheets will further improve the already promising photocatalytic activity reported using less active MoS<sub>2</sub> materials.<sup>35</sup> To this end, we are currently exploring this research direction, with the ultimate goal of incorporating highly active 1T-MX<sub>2</sub> nanosheets in a tandem cell configuration (Figure 1.4).

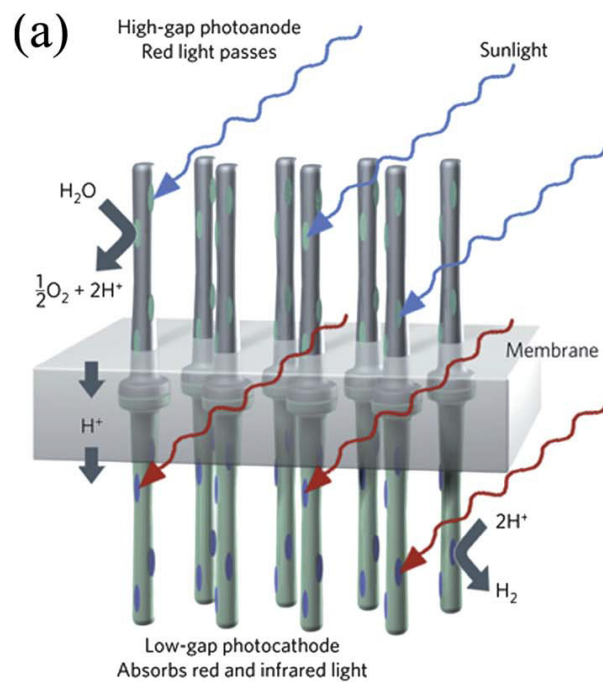


**Figure 1.4.** Cartoon representation of the idealized tandem device for water splitting where Si microwires decorated with catalyst efficiently perform the photoelectrocatalytic HER and OER.<sup>11</sup>

## 1.5 Oxygen Evolution from Photoanodes in PEC Solar Cells

### 1.5.1 Background and general PEC concepts

With our development of 1T-MX<sub>2</sub> nanosheets as highly active catalysts for the HER, we turn our attention to the other half reaction for water splitting. The oxygen evolution reaction (OER) is another elementary reaction that has received a great deal of attention in recent years, as it also partly limits the economic viability of generating clean chemical fuels.<sup>36</sup>



Although the OER can also be approached using electro- and photocatalysts, here we focus on the production of O<sub>2</sub> from photoelectrochemical systems using photoactive materials as the electrode. In these photoelectrodes, photocarriers generated by solar light irradiation are separated by the space-charge field created at the semiconductor-electrolyte interface. The minority carriers (holes for *n*-type photoanodes and electrons for a *p*-type photocathode) diffuse to the semiconductor-electrolyte junction to perform one half of the water splitting reaction (Figure 1.5).

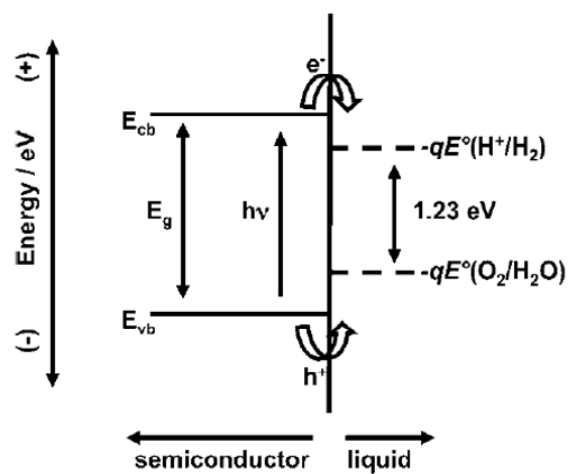


**Figure 1.5.** Energy diagram for photoelectrochemical water splitting using a single electrode where one material is responsible for both half reactions.<sup>4</sup>

The ideal material used for PEC water splitting should exhibit efficient broadband solar absorption, good semiconducting properties, and proper conduction and valence band alignments to reduce and oxidize water. Moreover, these materials should be photoelectrochemically stable in aqueous environments, non-toxic, and low cost. Not surprisingly, no single material has been identified which meets all of these criteria. Though wide band-gap semiconductors, such as  $\text{TiO}_2$ , are stable and have appropriate band-edge alignments, its large bandgap ( $E_g = 3.2$  eV for anatase) limits its absorption in the visible spectrum. Smaller bandgap materials such as  $\text{InP}$  ( $E_g = 1.3$  eV) are limited by their stability and use of rare and expensive elements.<sup>37</sup>

We can circumvent some of these materials requirements by using two different photoelectrodes in a tandem-cell design,<sup>38</sup> thereby decoupling the hydrogen and oxygen evolution reactions (Figure 1.6). Record solar-to-hydrogen (STH) conversion efficiencies over 12% have been reported using III-V semiconductor materials, but scalability and economic factors preclude its commercial use.<sup>5</sup> Stable and earth-abundant materials with intermediate bandgaps, such as  $\alpha\text{-Fe}_2\text{O}_3$  (hematite)<sup>39-43</sup> and  $\text{WO}_3$ ,<sup>44,45</sup> have been intensively investigated as alternative photoanode materials with the hope of enabling cost-effective PEC devices with reasonable efficiency. Though significant advances have been reported using  $\text{WO}_3$  as a photoanode, its larger bandgap and kinetic losses limit its maximum STH conversion efficiency to 8%.<sup>46</sup> To this end, we focus our efforts on hematite, which has the potential to achieve up to 16.8 % STH conversion,<sup>46</sup> though reported efficiencies are still well below this theoretical limit.

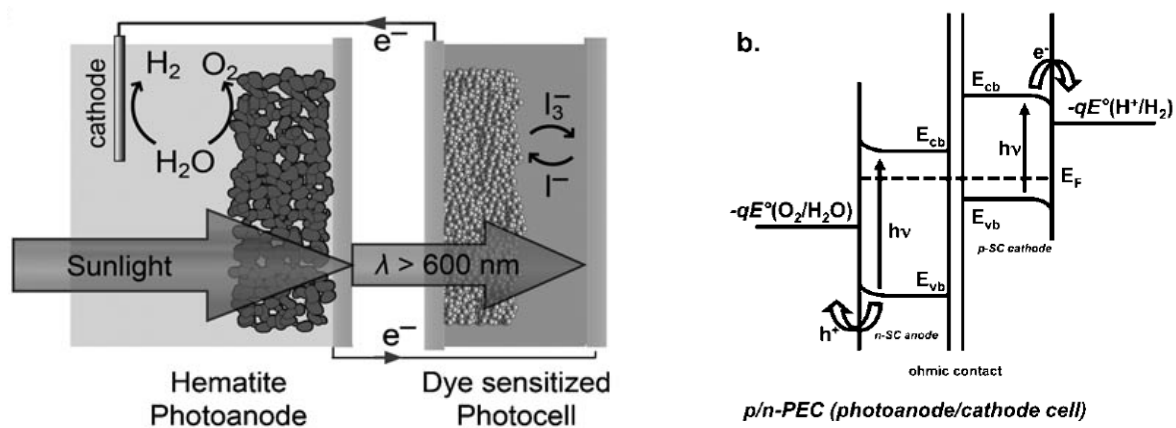


**Figure 1.6.** Tandem-cell designs where the water splitting half reactions are carried out by a specialized photoelectrodes. Possible tandem designs can pair photoanodes with (a) photovoltaic devices or (b) photocathodes.<sup>39</sup>

### 1.5.2 Hematite photoanodes in PEC solar cells

Colloquially known as “rust,” hematite has a favorable bandgap of 2.2 eV, allowing it to absorb approximately 40% of the solar spectrum, which is significantly more than other wide bandgap semiconductors like TiO<sub>2</sub>.<sup>47,48</sup> Its electrochemical stability, low toxicity, widespread abundance, and low-cost make hematite a particularly attractive photoanode material with applications in PEC solar cells. However, bulk hematite is also a notoriously poor semiconductor, suffering from short minority carrier lifetime (~10 ps) and diffusion length (~2-4 nm),<sup>49</sup> low absorptivity near the band edge ( $\alpha^{-1} \sim 0.12 \mu\text{m}$  at  $\lambda = 550 \text{ nm}$ ),<sup>50</sup> and low carrier mobility ( $< 1 \text{ cm}^2 \text{ V}^{-1} \text{ s}^{-1}$ ).<sup>43</sup> Additionally, complicated surface chemistry and sluggish kinetics for oxygen evolution have limited its PEC performance. Nanostructuring is a commonly used approach to help alleviate many of the traditional problems associated with hematite. Benefitting from orthogonalized light absorption and carrier separation,<sup>3</sup> nanostructured hematite photoanodes have exhibited enhanced PEC performance. Specifically, nanostructuring seems to improve the overall PEC performance by enhancing photocurrent, but improvements in overpotentials required for the onset of current remain limited.<sup>51</sup>

### 1.5.3 Strategies to overcome limitations of hematite photoanodes

Further improvements in the PEC performance of hematite photoanodes have been reported using impurity doping and catalyst integration. Dopants including Si,<sup>40</sup> Ti,<sup>52</sup> Sn,<sup>41,53</sup> Pt,<sup>54</sup> and Zr<sup>55</sup> (among others) have been investigated for hematite thin films or nanostructures. Surprisingly, the controlled and conclusive doping of high aspect-ratio hematite nanowires (NWs) is not well studied. We employ an improved thermal oxidation synthesis of hematite NWs as a convenient platform to understand their electrical transport properties as a function of

impurity dopants (Figure 1.6a).<sup>56</sup> Though most dopants only marginally improve PEC performance of hematite, Si, Ti, and Sn have been shown to significantly increase the photocurrent and yield lower onset voltages.<sup>40,52,53</sup> Typical incorporation of dopants has been accomplished during the growth of hematite photoanodes. While this co-growth method generally allows for a certain degree of control over the doping level, post-growth doping strategies have the added advantage of being generally applicable to any arbitrary nanostructured hematite synthesis. We report a simple post-synthetic chemical vapor deposition method to produce highly conductive Si-doped hematite NWs, as measured by a statistical analysis of the transport properties of single NW devices (Figure 1.6b).<sup>56</sup> Building upon this initial report, our group has also developed a similar post-growth doping method to produce Ti- and Zr- doped  $\alpha$ -Fe<sub>2</sub>O<sub>3</sub> NWs grown from a more cost-effective solution synthesis (Figure 1.6c).<sup>51</sup> These doped hematite NWs photoanodes exhibit enhanced PEC performance and could be used as the building blocks for further optimization where the incorporation of other high activity OER catalysts can be explored (Figure 1.7d).

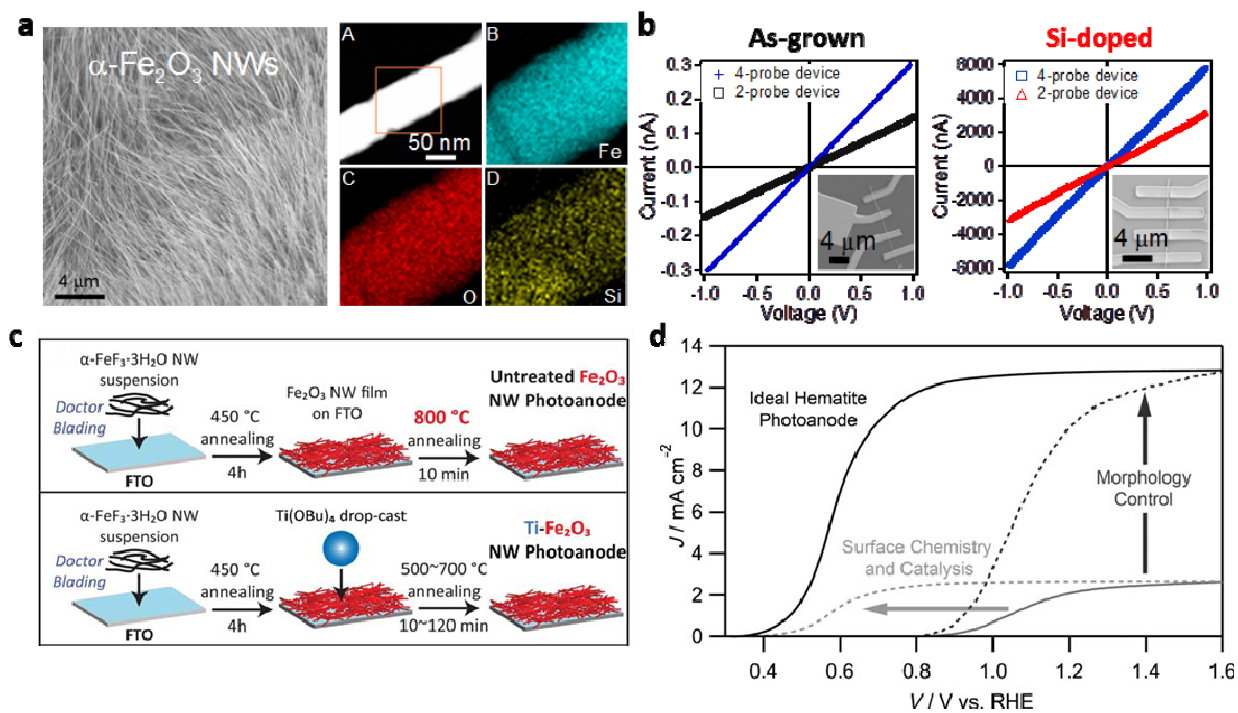


**Figure 1.7.** (a) Improved thermal oxidation synthesis of high aspect-ratio hematite nanowires that can be doped with Si to (b) greatly enhance their electrical transport properties.<sup>44</sup> (c) Synthetic scheme of solution-grown  $\text{FeF}_3 \cdot 3\text{H}_2\text{O}$  nanowires converted hematite by simple thermal oxidation which can be doped using simple dropcast and annealing methods.<sup>39</sup> (d) Two part strategy to improving the PEC performance of hematite photoanodes through the use of nanostructured morphology control (to enhance photocurrent) and surface chemistry to improve the overpotentials required for the onset of oxygen evolution.<sup>39,51,56</sup>

## 1.6 Conclusions

The environmental and economic factors driving contemporary research toward using alternative energies requires a clean burning fuel that can be stored for power generation on demand. Clean burning fuels, like H<sub>2</sub> and O<sub>2</sub>, are ideal candidates, but practical obstacles to the efficient operation of the water splitting reaction requires further advances in materials designed for the HER and OER. Here, we have introduced the basic concepts of hydrogen and oxygen evolution with the emphasis on developing cost-effective and earth-abundant materials as efficient catalysts and photoelectrodes. Specifically, we have briefly introduced and reviewed layered metal chalcogenides as catalysts for the HER and hematite photoanodes for PEC oxygen evolution. Expanding on these fields in the subsequent chapters, we will introduce our advances in developing superior HER catalysts and our more fundamental understanding of how doping affects electronic transport properties in hematite photoanodes.

## 1.6 References

- (1) Turner, J. A. *Science* **2004**, *305*, 972.
- (2) Lewis, N. S.; Nocera, D. G. *Proc. Natl. Acad. Sci. U. S. A.* **2006**, *103*, 15729.
- (3) Bierman, M. J.; Jin, S. *Energ Environ Sci* **2009**, *2*, 1050.
- (4) Walter, M. G.; Warren, E. L.; McKone, J. R.; Boettcher, S. W.; Mi, Q.; Santori, E. A.; Lewis, N. S. *Chem. Rev.* **2010**, *110*, 6446.
- (5) Khaselev, O.; Turner, J. A. *Science* **1998**, *280*, 425.
- (6) Licht, S.; Wang, B.; Mukerji, S.; Soga, T.; Umeno, M.; Tributsch, H. *Int. J. Hydrogen Energy* **2001**, *26*, 653.

- (7) McKone, J. R.; Warren, E. L.; Bierman, M. J.; Boettcher, S. W.; Brunschwig, B. S.; Lewis, N. S.; Gray, H. B. *Energ Environ Sci* **2011**, *4*, 3573.
- (8) Bard, A. J.; Faulkner, L. R. *Electrochemical Methods: Fundamentals and Applications*; 2 ed.; John Wiley & Sons, Inc., 2001.
- (9) Nørskov, J. K.; Bligaard, T.; Logadottir, A.; Kitchin, J. R.; Chen, J. G.; Pandelov, S.; Stimming, U. *J. Electrochem. Soc.* **2005**, *152*, J23.
- (10) Jaramillo, T. F.; Jørgensen, K. P.; Bonde, J.; Nielsen, J. H.; Horch, S.; Chorkendorff, I. *Science* **2007**, *317*, 100.
- (11) Laursen, A. B.; Kegnaes, S.; Dahl, S.; Chorkendorff, I. *Energ Environ Sci* **2012**, *5*, 5577.
- (12) Neyerlin, K. C.; Gu, W.; Jorne, J.; Gasteiger, H. A. *J. Electrochem. Soc.* **2007**, *154*, B631.
- (13) Merki, D.; Hu, X. *Energ Environ Sci* **2011**, *4*, 3878.
- (14) Chhowalla, M.; Shin, H. S.; Eda, G.; Li, L.-J.; Loh, K. P.; Zhang, H. *Nat Chem* **2013**, *5*, 263.
- (15) Wang, Q. H.; Kalantar-Zadeh, K.; Kis, A.; Coleman, J. N.; Strano, M. S. *Nat Nano* **2012**, *7*, 699.
- (16) Chianelli, R. R.; Siadati, M. H.; De la Rosa, M. P.; Berhault, G.; Wilcoxon, J. P.; Bearden, R.; Abrams, B. L. *Cataly Rev* **2006**, *48*, 1.
- (17) Tributsch, H.; Bennett, J. C. *J. Electroanal. Chem.* **1977**, *81*, 97.
- (18) Hinnemann, B.; Moses, P. G.; Bonde, J.; Jørgensen, K. P.; Nielsen, J. H.; Horch, S.; Chorkendorff, I.; Nørskov, J. K. *J. Am. Chem. Soc.* **2005**, *127*, 5308.
- (19) Bonde, J.; Moses, P. G.; Jaramillo, T. F.; Nørskov, J. K.; Chorkendorff, I. *Faraday Discuss.* **2009**, *140*, 219.

- (20) Chen, Z.; Cummins, D.; Reinecke, B. N.; Clark, E.; Sunkara, M. K.; Jaramillo, T. F. *Nano Lett.* **2011**, *11*, 4168.
- (21) Kibsgaard, J.; Chen, Z.; Reinecke, B. N.; Jaramillo, T. F. *Nat. Mater.* **2012**, *11*, 963.
- (22) Li, Y.; Wang, H.; Xie, L.; Liang, Y.; Hong, G.; Dai, H. *J. Am. Chem. Soc.* **2011**, *133*, 7296.
- (23) Merki, D.; Fierro, S.; Vrubel, H.; Hu, X. *Chem Sci* **2011**, *2*, 1262.
- (24) Benck, J. D.; Chen, Z.; Kuritzky, L. Y.; Forman, A. J.; Jaramillo, T. F. *ACS Catal* **2012**, *2*, 1916.
- (25) Chang, Y.-H.; Lin, C.-T.; Chen, T.-Y.; Hsu, C.-L.; Lee, Y.-H.; Zhang, W.; Wei, K.-H.; Li, L.-J. *Adv. Mater.* **2013**, *25*, 756.
- (26) Karunadasa, H. I.; Montalvo, E.; Sun, Y.; Majda, M.; Long, J. R.; Chang, C. J. *Science* **2012**, *335*, 698.
- (27) Jaramillo, T. F.; Bonde, J.; Zhang, J.; Ooi, B.-L.; Andersson, K.; Ulstrup, J.; Chorkendorff, I. *J. Phys. Chem. C* **2008**, *112*, 17492.
- (28) Lukowski, M. A.; Daniel, A. S.; Meng, F.; Forticaux, A.; Li, L.; Jin, S. *J. Am. Chem. Soc.* **2013**.
- (29) Py, M. A.; Haering, R. R. *Can. J. Phys.* **1983**, *61*, 76.
- (30) Joensen, P.; Frindt, R. F.; Morrison, S. R. *Mater. Res. Bull.* **1986**, *21*, 457.
- (31) Voiry, D.; Yamaguchi, H.; Li, J.; Silva, R.; Alves, D. C. B.; Fujita, T.; Chen, M.; Asefa, T.; Shenoy, V. B.; Eda, G.; Chhowalla, M. *Nat. Mater.* **2013**, *advance online publication*.
- (32) Zong, X.; Han, J.; Ma, G.; Yan, H.; Wu, G.; Li, C. *J. Phys. Chem. C* **2011**, *115*, 12202.
- (33) Ho, W. K.; Yu, J. C.; Lin, J.; Yu, J. G.; Li, P. S. *Langmuir* **2004**, *20*, 5865.

- (34) Di Paola, A.; Palmisano, L.; Derrigo, M.; Augugliaro, V. *J. Phys. Chem. B* **1997**, *101*, 876.
- (35) Hou, Y.; Abrams, B. L.; Vesborg, P. C. K.; Bjorketun, M. E.; Herbst, K.; Bech, L.; Setti, A. M.; Damsgaard, C. D.; Pedersen, T.; Hansen, O.; Rossmeisl, J.; Dahl, S.; Norskov, J. K.; Chorkendorff, I. *Nat. Mater.* **2011**, *10*, 434.
- (36) Rossmeisl, J.; Logadottir, A.; Norskov, J. K. *Chem. Phys.* **2005**, *319*, 178.
- (37) Szklarczyk, M.; Bockris, J. O. M. *J. Phys. Chem.* **1984**, *88*, 5241.
- (38) Minggu, L. J.; Wan Daud, W. R.; Kassim, M. B. *Int. J. Hydrogen Energy* **2010**, *35*, 5233.
- (39) Sivula, K.; Le Formal, F.; Grätzel, M. *ChemSusChem* **2011**, *4*, 432.
- (40) Kay, A.; Cesar, I.; Grätzel, M. *J. Am. Chem. Soc.* **2006**, *128*, 15714.
- (41) Sivula, K.; Zboril, R.; Le Formal, F.; Robert, R.; Weidenkaff, A.; Tucek, J.; Frydrych, J.; Grätzel, M. *J. Am. Chem. Soc.* **2010**, *132*, 7436.
- (42) Li, L.; Yu, Y.; Meng, F.; Tan, Y.; Hamers, R. J.; Jin, S. *Nano Lett.* **2012**, *12*, 724.
- (43) Klahr, B.; Gimenez, S.; Fabregat-Santiago, F.; Hamann, T.; Bisquert, J. *J. Am. Chem. Soc.* **2012**, *134*, 4294.
- (44) Santato, C.; Ulmann, M.; Augustynski, J. *J. Phys. Chem. B* **2001**, *105*, 936.
- (45) Su, J.; Feng, X.; Sloppy, J. D.; Guo, L.; Grimes, C. A. *Nano Lett.* **2010**, *11*, 203.
- (46) Murphy, A. B.; Barnes, P. R. F.; Randeniya, L. K.; Plumb, I. C.; Grey, I. E.; Horne, M. D.; Glasscock, J. A. *Int. J. Hydrogen Energy* **2006**, *31*, 1999.
- (47) Gratzel, M. *Nature* **2001**, *414*, 338.
- (48) van de Krol, R.; Liang, Y.; Schoonman, J. *J. Mater. Chem.* **2008**, *18*, 2311.
- (49) Cherepy, N. J.; Liston, D. B.; Lovejoy, J. A.; Deng, H.; Zhang, J. Z. *J. Phys. Chem. B* **1998**, *102*, 770.

- (50) Itoh, K.; Bockris, J. O. M. *J. Electrochem. Soc.* **1984**, *131*, 1266.
- (51) Franking, R.; Li, L.; Lukowski, M. A.; Meng, F.; Tan, Y.; Hamers, R. J.; Jin, S. *Energ Environ Sci* **2013**, *6*, 500.
- (52) Wang, G.; Ling, Y.; Wheeler, D. A.; George, K. E. N.; Horsley, K.; Heske, C.; Zhang, J. Z.; Li, Y. *Nano Lett.* **2011**, *11*, 3503.
- (53) Ling, Y.; Wang, G.; Wheeler, D. A.; Zhang, J. Z.; Li, Y. *Nano Lett.* **2011**, *11*, 2119.
- (54) Hu, Y.-S.; Kleiman-Shwarsstein, A.; Forman, A. J.; Hazen, D.; Park, J.-N.; McFarland, E. W. *Chem. Mater.* **2008**, *20*, 3803.
- (55) Horowitz, G. *J. Electroanal. Chem.* **1983**, *159*, 421.
- (56) Lukowski, M. A.; Jin, S. *J. Phys. Chem. C* **2011**, *115*, 12388.

## Chapter 2

### Enhanced Hydrogen Evolution Catalysis from Chemically

### Exfoliated Metallic MoS<sub>2</sub> Nanosheets\*

#### 2.1 Abstract

Promising catalytic activity from molybdenum disulfide (MoS<sub>2</sub>) in the hydrogen evolution reaction (HER) is attributed to active sites located along the edges of its two-dimensional layered crystal structure, but its performance is currently limited by the density and reactivity of active sites, poor electrical transport, and inefficient electrical contact to the catalyst. Here we report dramatically enhanced HER catalysis (an electrocatalytic current density of 10 mA/cm<sup>2</sup> at a low overpotential of -187 mV vs. RHE and a Tafel slope of 43 mV/decade) from metallic nanosheets of 1T-MoS<sub>2</sub> chemically exfoliated *via* lithium intercalation from semiconducting 2H-MoS<sub>2</sub> nanostructures grown directly on graphite. Structural characterization and electrochemical studies confirm that the nanosheets of the metallic MoS<sub>2</sub> polymorph exhibit facile electrode kinetics, low-loss electrical transport, and possess a proliferated density of catalytic active sites. These distinct and previously unexploited features of 1T-MoS<sub>2</sub> make these metallic nanosheets a highly competitive earth-abundant HER catalyst.

---

\* This chapter was originally published in *J. Am. Chem. Soc.* **2013**, *135*, 10274. It was prepared in collaboration with A.S. Daniel, F. Meng, A. Foricaux, L. Li, and S. Jin before being adapted here.

## 2.2 Introduction

The vision of utilizing hydrogen as a future energy carrier requires cost-effective, sustainable, and efficient hydrogen production.<sup>1</sup> While platinum and other precious metals are the best catalysts for the hydrogen evolution reaction (HER) in acidic media, replacing rare and expensive electrocatalysts with earth-abundant materials would represent a significant step toward making hydrogen a competitive alternative energy source and facilitate the transition to the hydrogen economy.<sup>1b,2</sup> Although traditionally used as an industrial hydrodesulfurization catalyst,<sup>3</sup> molybdenum disulfide ( $\text{MoS}_2$ ) is an exciting HER catalyst<sup>4</sup> that exhibits promising hydrogen evolution activity in crystalline<sup>5</sup> or amorphous materials,<sup>6</sup> and molecular mimics.<sup>7</sup> However, the catalytic HER performance of  $\text{MoS}_2$  is currently limited by the density and reactivity of active sites, poor electrical transport, and inefficient electrical contact to the catalyst.<sup>4,6a</sup>

$\text{MoS}_2$  belongs to a large family of two-dimensional (2D) layered metal chalcogenide materials that have the general  $\text{MX}_2$  formula, where M is a metal and X is a chalcogen (sulfur, selenium, or tellurium). Similar to graphene in graphite, individual sandwiched S-Mo-S layers are held together by weak van der Waals interactions in hexagonally packed structures. Experimental<sup>5a</sup> and computational<sup>5b</sup> studies conclude that catalytic activity arises from the active sites located along the edges of 2D  $\text{MoS}_2$  layers while basal surfaces are catalytically inert. The edges of  $\text{MX}_2$  are under coordinated and thermodynamically unfavorable, which explains the general propensity of  $\text{MX}_2$  to form closed-shell inorganic fullerene structures when synthesized on the nanoscale.<sup>8</sup> Recent studies sought to control  $\text{MoS}_2$  nanostructure growth and engineer their surface to maximize the density of active edge sites for catalysis.<sup>9</sup> Although the number of edge sites is unquestionably important for catalytic performance, as-synthesized  $\text{MoS}_2$  is a

semiconductor where poor bulk conduction and anisotropic electrical transport can limit overall catalytic efficiency.<sup>5a,9a</sup>

However, MoS<sub>2</sub> and other 2D metal chalcogenides can exist in various polymorphs (Figure 2.1) where subtle structural changes dramatically affect electrical properties.<sup>10</sup> Natural MoS<sub>2</sub> is found as the semiconducting and thermodynamically favored 2H phase which is described by two S-Mo-S layers built from edge-sharing MoS<sub>6</sub> trigonal prisms. In contrast, the metallic 1T polymorph is described by a single S-Mo-S layer composed of edge-sharing MoS<sub>6</sub> octahedra, and is not naturally found in bulk. Interesting optical and semiconducting properties<sup>11</sup> drive the contemporary research on single layers of semiconducting MX<sub>2</sub> isolated by mechanical<sup>12</sup> or chemical<sup>13</sup> exfoliation for applications in high performance devices. Although the 1T-MX<sub>2</sub> structure was characterized during the early exploration of 2D materials,<sup>14</sup> the catalytic hydrogen evolution properties of exfoliated 1T-MoS<sub>2</sub> nanosheets remain unexplored.<sup>11b</sup> Herein we overcome the challenges limiting the catalytic performance of MoS<sub>2</sub> by controlling the synthesis of its nanostructures and structural polymorphs using simple intercalation chemistry to make MoS<sub>2</sub> nanostructures a highly competitive earth-abundant catalyst for the HER.

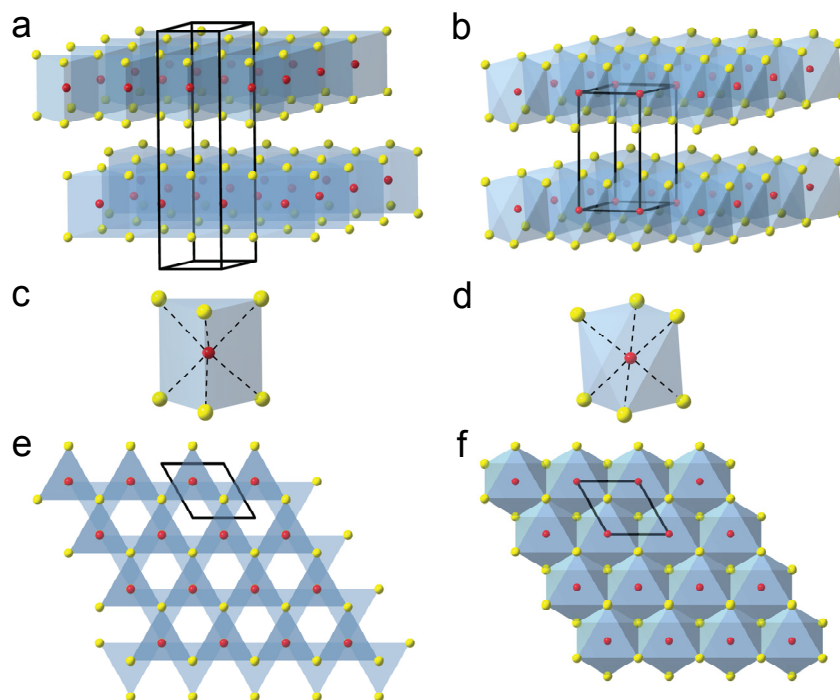


**Figure 2.1.** Crystal structure models illustrating the differences between the (a) 2H- and (b) 1T- $\text{MoS}_2$  polymorphs, highlighting the (c) trigonal prismatic and (d) octahedral coordination of the metal atoms. Projection along the  $c$ -axis reveals further contrast between the (e) 2H and (f) 1T polymorphs. The 1T- $\text{MoS}_2$  structure model was drawn using the crystallographic coordinates for the 1T- $\text{TiS}_2$  compound for illustration purposes since bulk 1T- $\text{MoS}_2$  does not exist.

## 2.3 Experimental Section

### 2.3.1 Synthesis of MoS<sub>2</sub> nanostructures

Spectroscopically pure graphite rods (99.9995%, Ultra F purity, Ultra Carbon Corporation) cut into thin discs (6 mm diameter; ~0.4 mm thick) were polished to a near-mirror finish using abrasive cloths. They are sonicated subsequently in 18 MΩ deionized water for 10 min, then in aqua regia (3:1 concentrated HCl: concentrated HNO<sub>3</sub> for 10 min (to remove remnant metal impurities), and then in 18 MΩ deionized water for 10 min again, before they were dried in an oven at 120 °C for 20 min. In a home-built CVD reactor consisting of a 1 inch fused silica tube equipped with pressure and gas flow controls placed in a single-zone tube furnace, alumina combustion boats charged with 50 mg molybdenum chloride (MoCl<sub>5</sub>, 95 %) and 200 mg elemental sulfur (99.5 %) were placed outside of the tube furnace upstream of the prepared graphite substrates. The reactor was evacuated and flushed three times with argon before it was back filled to the set-point pressure of 770 Torr under an argon flow of 125 sccm and heated to 525 °C. The MoCl<sub>5</sub> and sulfur boats were pushed into the mouth of the furnace (1.5 cm for MoCl<sub>5</sub> boat; 4.5 cm for sulfur boat) using a magnet to initiate the reaction which lasts 20 min, then the furnace was cooled naturally under argon flow.

### 2.3.2 *n*-Butyl lithium exfoliation treatment

Inside an argon-filled glove box, the purplish-blue substrates covered with as-synthesized MoS<sub>2</sub> nanostructures were soaked in 3 mL *n*-butyl lithium (2.7 M in heptane or 1.6 M in hexanes) inside sealed vials for 6–48 h. The sealed vials could also be brought out of the glove box and heated to 60 °C. Excess *n*-butyl lithium was removed by rinsing the treated substrates

with dry heptane, then the substrates were reacted with excess 18 M $\Omega$  deionized water and gently rinsed with water.

### **2.3.3 Structural characterization**

SEM was performed using a LEO Supra55 VP microscope operating at 3 kV. PXRD data were collected on harvested nanostructures dispersed on glass substrates using a Bruker D8 advanced powder diffractometer with Cu Ka radiation and the background from glass substrate was subtracted. TEM samples were prepared by gentle sonication and dropcasting onto lacey carbon supported TEM grids. HRTEM of the MoS<sub>2</sub> nanostructures and nanosheets was performed using an aberration-corrected FEI Titan scanning transmission electron microscope operated at an accelerating voltage of 200 kV in TEM mode. Electron diffraction of the exfoliated MoS<sub>2</sub> nanosheets was collected using a FEI T12 microscope operated at an accelerating voltage of 120 kV. Raman spectra were taken using a Thermo Scientific DXR confocal Raman microscope using a 532 nm excitation laser. AFM measurements were taken on samples grown on HOPG substrates using an Agilent 5500 AFM equipped with current-sensing capabilities using a symmetric Pt coated tip (30 nm, mikroMasch) with a force constant of 2.7 N/m. All of the data were collected in the trace, with no significant hysteresis in the retrace, as current-sensing requires the AFM to be operated in contact mode.

### **2.3.4 Electrochemical characterization**

Electrochemical measurements were performed using a rotating disc electrode (BASi, RDE-2) in a three-electrode electrochemical cell using a Bio-Logic SP-200 potentiostat. All measurements were performed in 50 mL of 0.5 M H<sub>2</sub>SO<sub>4(aq)</sub> electrolyte (pH = 0.16) prepared

using 18 M $\Omega$  deionized water purged with H<sub>2</sub> gas (99.999%), using MoS<sub>2</sub> on graphite discs as the working electrode, a graphite rod as a counter electrode, and a saturated calomel (SCE) reference electrode (CH Instruments). The MoS<sub>2</sub> on graphite discs were mounted on top of the embedded glassy carbon RDE electrodes using colloidal silver paint (Ted Pella). As a comparison, a standard Pt disc (4 mm diameter, Ted Pella) was mounted to the glassy carbon RDE electrode using the same method. The reversible hydrogen electrode (RHE) was calibrated using platinum as both working and counter electrodes to +0.260 V vs. the SCE reference. The performance of the hydrogen evolution catalyst is measured using linear sweep voltammetry beginning at +0.30 V and ending at -0.45 V vs. RHE with a scan rate of 3 mV/s when the working electrode is rotated at 2000 rpm. Electrochemical impedance spectroscopy was performed when the working electrode was biased at a constant -0.250 V vs. RHE while sweeping the frequency from 5 MHz to 10 mHz with a 10 mV AC dither. The impedance data were fit to a simplified Randles circuit to extract the series and charge transfer resistances. The electrochemical stability of the catalyst was evaluated by cycling the electrode 1000 times; each cycle started at +0.10 V and ended at -0.45 V vs. RHE with a scan rate of 50 mV/s while rotating the working electrode at 2000 rpm. Cyclic voltammograms taken with various scan rates (20, 40, 60 mV/s, etc.) were used to estimate the double-layer capacitance were collected in the 0.1–0.2 V vs. RHE region.

## 2.4 Results and Discussion

### 2.4.1 Synthesis and characterization of as-grown MoS<sub>2</sub> Nanostructures

We first synthesize flower-like MoS<sub>2</sub> nanostructures with a high density of exposed edges directly on graphite substrates *via* a simple chemical vapor deposition (CVD) method starting

from molybdenum(V) chloride and elemental sulfur precursors. The relatively mild reaction conditions at 525 °C allow for high density deposition of MoS<sub>2</sub> nanostructures on a variety of substrates, including silicon/silicon oxide, glass, fluorine-doped tin oxide on glass, molybdenum foils, carbon paper, and graphite (Figure 2.2). This highly tunable synthesis<sup>15</sup> offers two advantages: i) the dense MoS<sub>2</sub> flakes are dominated by edges (Figure 2.3a), thus increasing the density of active sites, and ii) the direct growth on conductive graphite substrates results in high-quality, low electrical-loss contact to the three-dimensional nanostructured electrocatalyst (Figure 2.3b). Lower resolution transmission electron microscopy (TEM) confirms the as-grown nanostructures are multilayered open structures (not inorganic fullerenes) hundreds of nanometers wide (Figure 2.3c). The lattice-resolved high-resolution TEM (HRTEM) (Figure 2.3d) and the corresponding fast Fourier transform (FFT) (Figure 2.3e) show highly crystalline structures that are indexed unequivocally to 2H-MoS<sub>2</sub>.

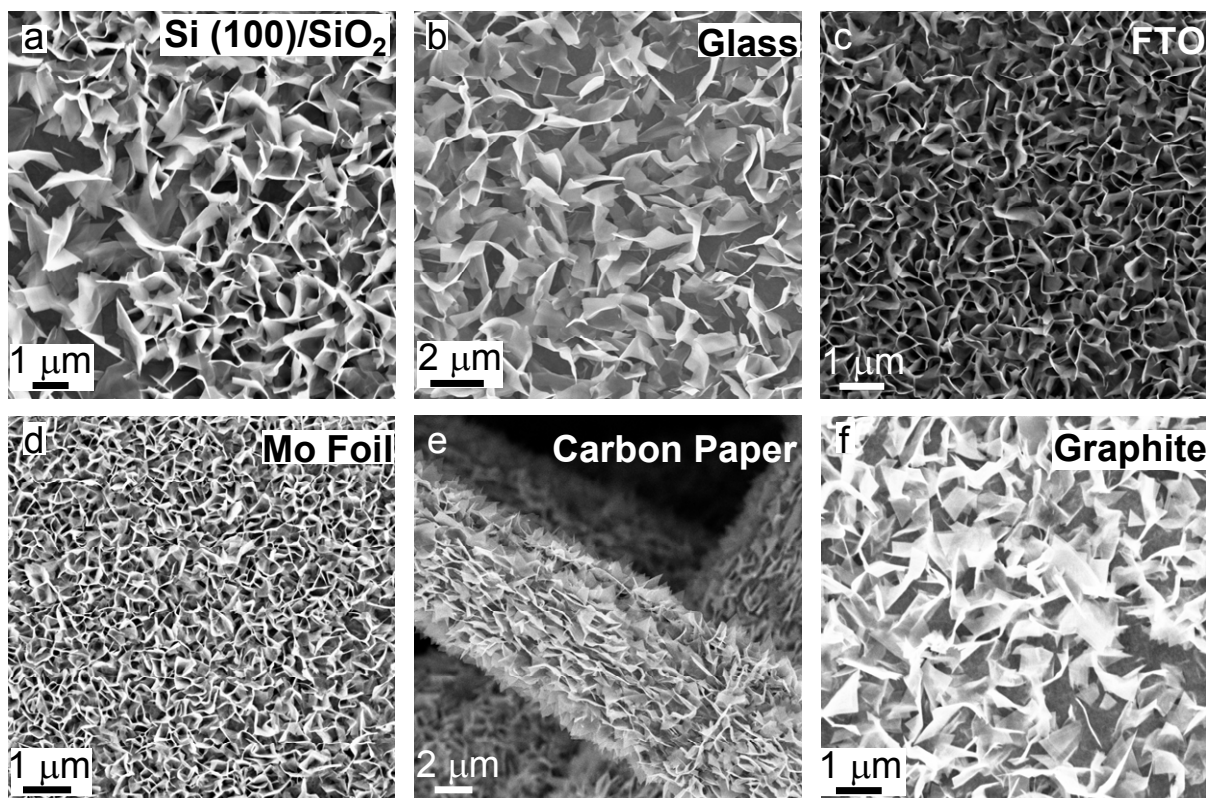


**Figure 2.2.** Representative SEM micrographs showing high-density deposition of MoS<sub>2</sub> flower-like nanostructures on: (a) Si (100)/SiO<sub>2</sub>, (b) glass, (c) FTO, (d) Mo foil, (e) carbon paper, and (f) graphite.

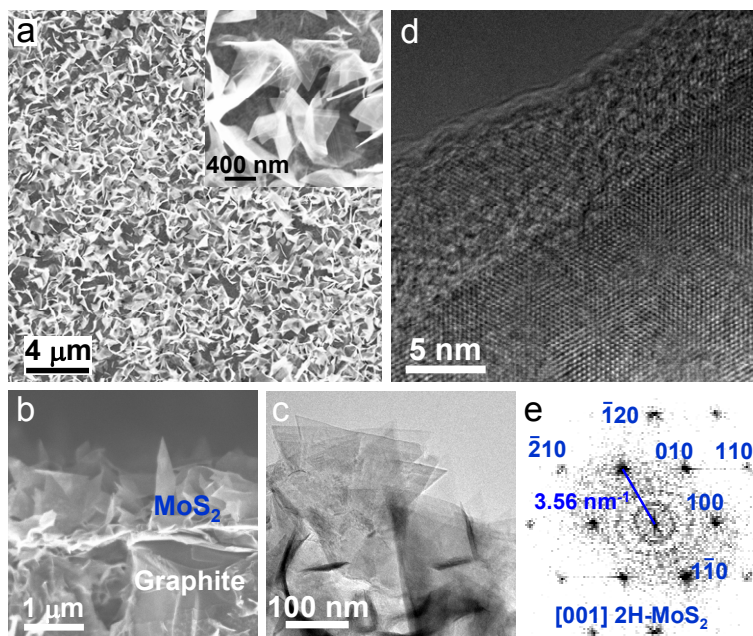


**Figure 2.3.** Electron microscopy characterization of as-grown 2H-MoS<sub>2</sub> nanostructures. (a) Top-down and (b) cross-section SEM images. (c) Low and (d) high-resolution TEM images with corresponding (e) indexed FFT.

We further confirmed the phase identity of the as-synthesized MoS<sub>2</sub> nanostructures using powder X-ray diffraction (PXRD) (Figure 2.4a) and Raman spectroscopy (Figure 2.4b). Strong (00*l*) reflections in the PXRD pattern illustrate the crystallinity and ordered stacking of 2D layers in the as-grown MoS<sub>2</sub> nanostructures. Furthermore, Scherrer analysis of the peak broadening in the (002) reflection yields an estimated average of 12 MoS<sub>2</sub> layers per flake. Characteristic Raman shifts (387, 412, and 456 cm<sup>-1</sup>) expected for the E<sub>2g</sub><sup>1</sup>, A<sub>1g</sub>, and longitudinal acoustic phonon modes for 2H-MoS<sub>2</sub>,<sup>16</sup> respectively, are clearly observed.

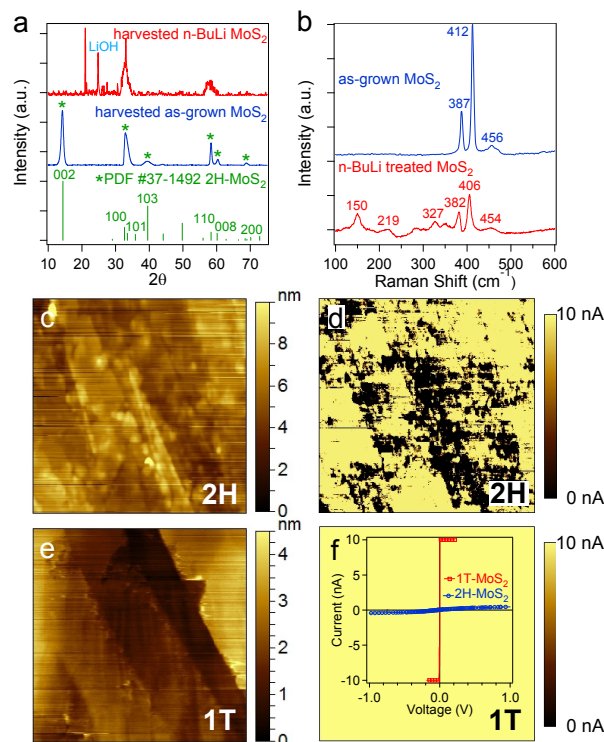


**Figure 2.4.** Comparison of as-grown and exfoliated MoS<sub>2</sub> nanosheets. (a) PXRD and (b) Raman spectra illustrating that the as-grown sample is pure 2H-MoS<sub>2</sub> and the exfoliated MoS<sub>2</sub> nanosheets contain a mixture of 1T- and 2H-MoS<sub>2</sub>. (c-f) Current-sensing AFM micrographs and conductivity maps for as-grown (c, d) and chemically exfoliated (e, f) MoS<sub>2</sub> nanosheets. All images are 3 μm by 3 μm and the conductivity maps were taken with a bias at 50 mV.

### 2.4.2 Lithium Intercalation and Exfoliated Nanosheet Characterization

We then convert the as-grown multilayered semiconducting MoS<sub>2</sub> nanostructures to the metallic 1T-MoS<sub>2</sub> polymorph by simply soaking them in n-butyl lithium solution at room temperature or 60 °C for 6–48 h and exfoliate the nanostructures by reacting the intercalated lithium with excess water, which generates H<sub>2</sub> gas and separates the 2D nanosheets. The absence of the (00 $l$ ) peaks in the PXRD pattern of an exfoliated sample (Figure 2.4a top trace) clearly shows that the long-range stacking order of the nanosheets along the c-axis is destroyed, i.e. the MoS<sub>2</sub> nanostructures are efficiently exfoliated into essentially single layers of MoS<sub>2</sub>. These structures are referred to as the MoS<sub>2</sub> nanosheets. Note that lithium intercalation into graphite is not favorable under these conditions.<sup>17</sup> The transition to the 1T phase is caused by electron transfer from intercalated Li, which destabilizes the original trigonal prismatic 2H-MoS<sub>2</sub> structure and favors octahedrally coordinated Mo atoms.<sup>10a</sup> The emergence of new Raman shifts (150, 219, and 327 cm<sup>-1</sup>) (Figure 2.4b bottom trace) associated with the phonon modes of 1T-MoS<sub>2</sub><sup>10c,16</sup> clearly confirms the formation of 1T-MoS<sub>2</sub> in exfoliated nanosheets. Raman shifts associated with the 2H phase are significantly suppressed but still observed. Although this exfoliation method was known to primarily yield 1T-MoS<sub>2</sub>,<sup>10a,13a</sup> recent studies show the coexistence of coherent nanometer-sized domains of 1T and 2H polymorphs in exfoliated single-layer MoS<sub>2</sub>.<sup>18</sup> The semiconducting to metallic phase transition is also confirmed by current-sensing atomic force microscopy (CSAFM). Contact-mode topography (Figure 2.4c&e), friction, and deflection images (Appendix 1 Figure A1.1) clearly show the presence of material on a highly ordered pyrolytic graphite (HOPG) substrate. The corresponding conductivity maps taken at +50 mV sample bias illustrate the uniformly metallic conduction in exfoliated MoS<sub>2</sub> (Figure 2.4f) and the inhomogeneous conductivity in semiconducting 2H-MoS<sub>2</sub> sample (Figure

2.4d). Individual I-V sweeps on specific nanostructures (Figure 2.4f inset) contrast the relatively poor conductivity of the as-grown 2H-MoS<sub>2</sub> with the metallic conduction observed in the exfoliated MoS<sub>2</sub>. The small size (1-10 nm<sup>2</sup>) expected for the remnant nanodomains of 2H polymorph present in the chemically exfoliated nanosheets<sup>18</sup> are below the resolution limit of the CSAFM due to the diameter of the tip (30 nm).

The MoS<sub>2</sub> nanostructure morphology is preserved after exfoliation (Figure 2.5a), though the exfoliated nanosheets are more disordered and compressed onto the substrate surface than the as-grown 3D MoS<sub>2</sub> nanoflowers (Figure 2.3a). Cross-section SEM (Figure 2.5b) suggests that electrical contact between the electrocatalyst and graphite substrate is maintained after exfoliation. HRTEM clearly shows regions of MoS<sub>2</sub> sheets with resolved crystal lattice, but the exfoliated nanosheets quickly become amorphous under the typical 200 kV TEM imaging conditions (Figure 2.5c arrows). The nanosheets are stable under a lower accelerating voltage of 120 kV (Figure 2.5d), which enables electron diffraction study even though high-resolution TEM imaging is not possible. The indexed [001] zone axis diffraction pattern (Figure 2.5e) confirms the expected crystal symmetry and expansion of the lattice constant for 1T-MoS<sub>2</sub><sup>10b</sup> (see Appendix 1 and Figure A1.2 for detail).

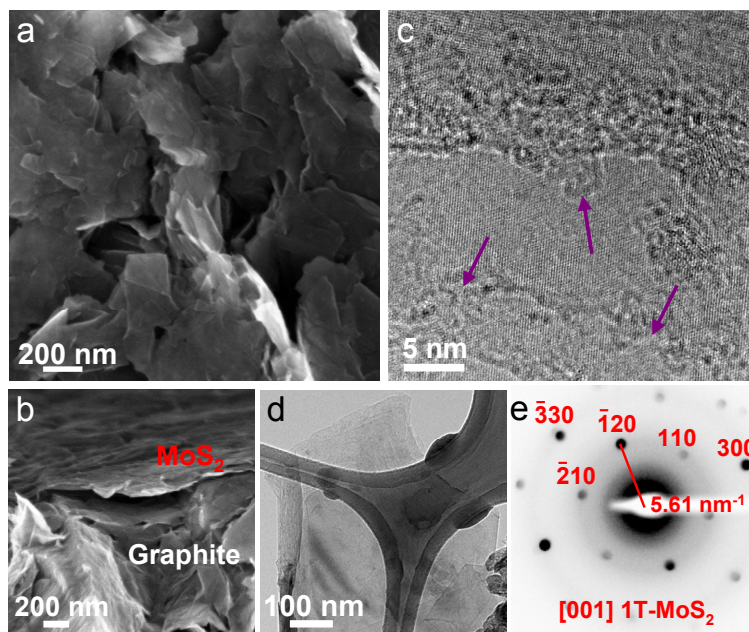


**Figure 2.5.** Electron microscopy characterization of the chemically exfoliated MoS<sub>2</sub> nanosheets. (a) Top-down and (b) cross-section SEM images. (c) Unstable HRTEM image taken at 200 kV. (d) Stable TEM images taken at 120 kV with corresponding (e) indexed electron diffraction.

### 2.4.3 Electrocatalytic Performance of as-grown and chemically exfoliated MoS<sub>2</sub> nanosheets

We have found this simple chemical exfoliation dramatically enhances the catalytic HER performance of MoS<sub>2</sub> nanosheets compared to the as-grown nanostructures. The direct growth and exfoliation of MoS<sub>2</sub> nanosheets on conducting graphite substrates enables convenient evaluation of their catalytic activity by attaching the substrate to a standard rotating disc electrode (RDE) apparatus in a three-electrode electrochemical measurement using 0.5 M H<sub>2</sub>SO<sub>4(aq)</sub> electrolyte continuously purged with H<sub>2</sub> gas. Polarization curves of the current density plotted against overpotential vs. reversible hydrogen electrode (RHE) show the HER activity of the as-grown MoS<sub>2</sub> and chemically exfoliated MoS<sub>2</sub> nanosheets on graphite compared to Pt (Figure 2.6a&b). As-grown 2H-MoS<sub>2</sub> exhibits onset of HER activity at approximately -200 mV vs. RHE, consistent with previously reports,<sup>5a,5c,9a</sup> and significant hydrogen evolution (10 mA/cm<sup>2</sup>) is not achieved until -320 mV vs. RHE. 1T-MoS<sub>2</sub> nanosheets that have been exfoliated after lithium intercalation at 60 °C for 48 h show dramatically improved HER activity, with electrocatalytic current densities reaching 200 mA/cm<sup>2</sup> at -400 mV vs. RHE (Figure 2.6a). Moreover, the onset of catalytic activity is shifted to a much lower overpotential so that significant hydrogen evolution (10 mA/cm<sup>2</sup>) is observed at overpotential as low as -195 mV (Figure 2.6b). Correcting the raw data for *iR* losses (see Appendix 1 and Figure A1.3 for detail) reveals even more impressive performance; an electrocatalytic current density of 10 mA/cm<sup>2</sup> can be achieved at a low overpotential of -187 mV vs. RHE (filled squares in Figure 2.6b). The dramatic enhancement in catalytic activity is even more apparent when comparing the Tafel slopes (Figure 2.6c) of the exfoliated MoS<sub>2</sub> nanosheets (54 mV/decade raw; 43 mV/decade after *iR* correction) and as-grown nanostructures (117 mV/decade; 110 mV/decade after *iR* correction). The earlier onset of catalytic activity and lower Tafel slope suggest the free energy

of hydrogen adsorption is closer to equilibrium. The 43 mV/decade Tafel slope and the early onset of significant hydrogen evolution confirms 1T-MoS<sub>2</sub> is among the most catalytic materials for any MoS<sub>2</sub> catalysts.<sup>4</sup>

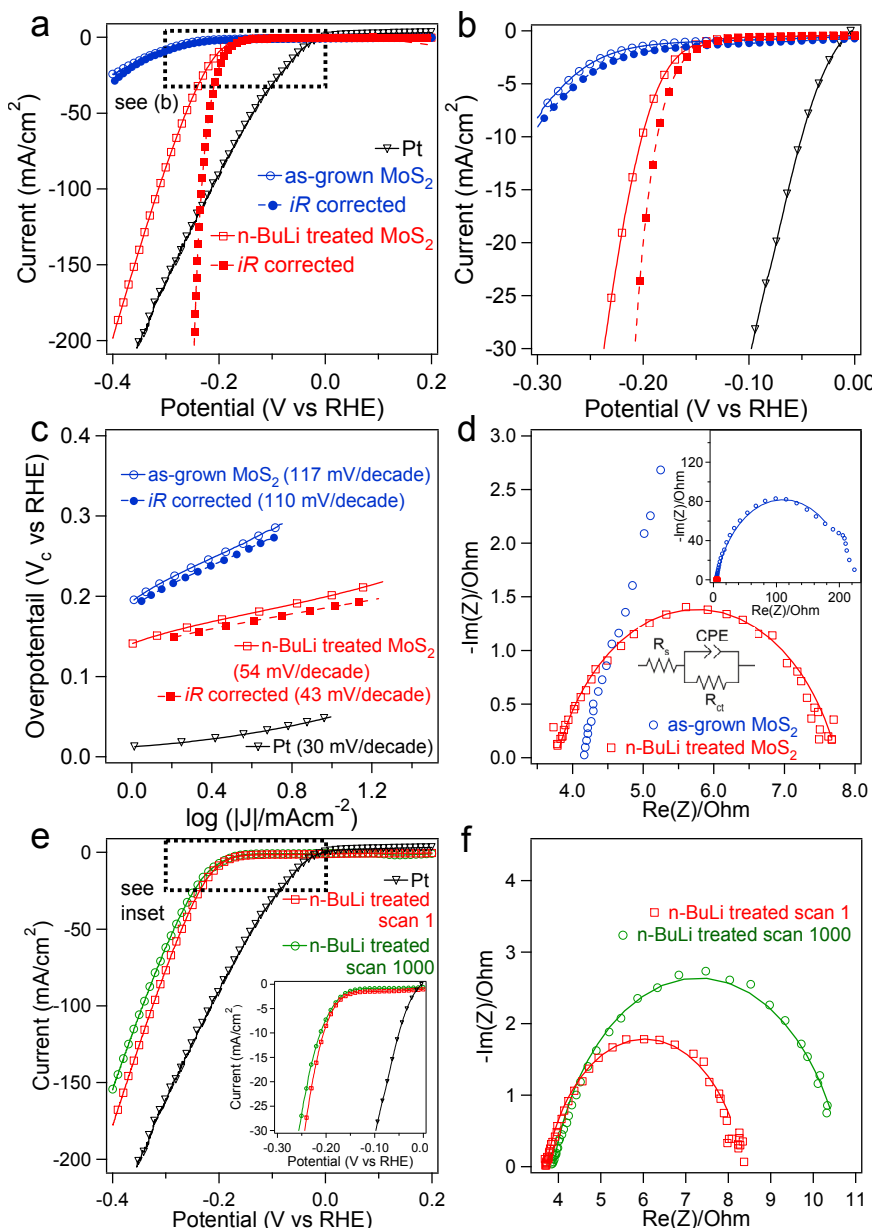


**Figure 2.6.** Electrocatalytic performance of the chemically exfoliated and as-grown MoS<sub>2</sub> nanosheets. Polarization curves at (a) higher and (b) lower overpotentials with corresponding (c) Tafel plots. Filled symbols show data after the *iR* correction. (d) EIS shows the facile electrode kinetics of 1T-MoS<sub>2</sub>. (e) Polarization curves and (f) EIS show 1T-MoS<sub>2</sub> nanosheets still exhibit excellent catalytic activity after 1000 cycles of continuous operation.

We explored various lithium intercalation conditions to optimize the catalytic activity of exfoliated MoS<sub>2</sub> nanosheets. The catalytic performance of the MoS<sub>2</sub> nanosheets was examined as a function of the duration of intercalation, temperature, and concentration of the *n*-butyl lithium solution (Figure 2.7). The as-synthesized MoS<sub>2</sub> nanostructures on graphite substrates from the same CVD synthesis were soaked in 1.6 M *n*-butyl lithium in hexanes at room temperature (23 °C) for 6, 12, and 48 h, or in 2.7 M *n*-butyl lithium in heptane at 60 °C for 12, 24, 36, and 48 h before chemically exfoliating the MoS<sub>2</sub> nanosheets. Significant improvement in catalytic performance compared to the as-grown MoS<sub>2</sub> nanostructures are observed for samples from all intercalation conditions, even at room temperature after only a few hours of soaking in *n*-butyl lithium. Control experiments show no appreciable HER activity from graphite substrates even after exposure to the same lithium intercalation conditions. In addition, we do not expect residual lithium to have any affect on the observed hydrogen evolution catalysis in this acidic solution, especially for the cycling and long term stability studies. The most important factors contributing to enhanced catalytic activity are the duration of intercalation and temperature. The data also indicate that a more concentrated *n*-butyl lithium solution (2.7 M in heptane) also helps to accelerate the intercalation process. As-synthesized MoS<sub>2</sub> nanostructures require shorter diffusion distance than bulk MoS<sub>2</sub> crystals, but the faster intercalation kinetics at 60 °C allow for more complete lithiation of MoS<sub>2</sub> within a shorter time. This results in a more thorough exfoliation of the MoS<sub>2</sub> nanosheets and a more complete 2H to 1T phase transformation, which explains the enhanced HER activity.

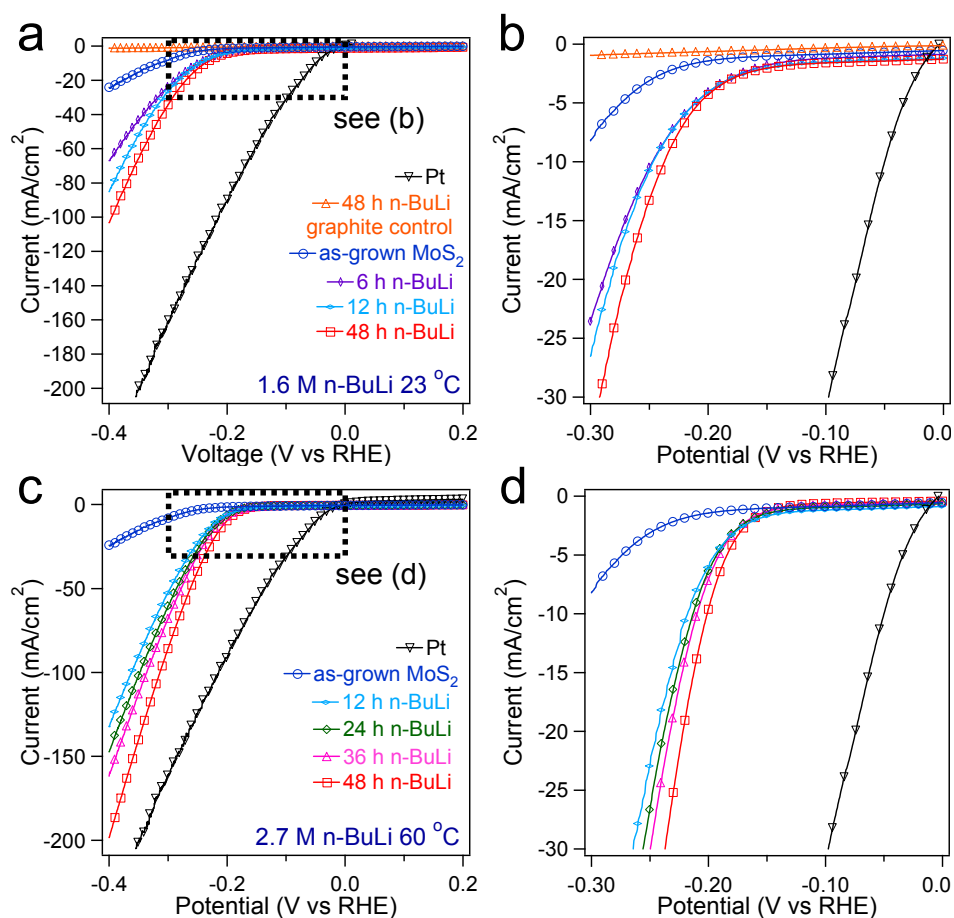


**Figure 2.7.** Polarization curves showing the (a) overall catalytic activity and (b) performance at lower overpotentials as a function of intercalation duration at room temperature in 1.6 M *n*-butyl lithium in hexanes. Increasing the intercalation temperature to 60 °C and using a more concentrated 2.7 M *n*-butyl lithium in heptane results in more enhancement of (c) overall HER activity and (d) requires lower overpotentials to achieve significant H<sub>2</sub> evolution. These data have not been corrected for *iR* losses.

Although the efficient exfoliation of MoS<sub>2</sub> nanoflowers (Figure 2.4a) results in the proliferation of active edge sites, we believe the phase transition into the metallic 1T polymorph is even more important to enhancing catalytic activity. The increase in the density of active sites due to exfoliation can be revealed by the > 10 fold increase in the double-layer capacitance ( $C_{dl}$ ) and, thus, relative electrochemical surface area as estimated using a simple cyclic voltammetry method<sup>19</sup> (see Appendix 1 and Figure A1.4 for detail). However, exfoliated semiconducting 2H-MoS<sub>2</sub> nanosheets recently investigated for hydrogen evolution only showed marginally improved catalytic performance,<sup>20</sup> suggesting that the density of edge sites is not the most important factor behind the dramatically enhanced performance of our 1T-MoS<sub>2</sub> nanosheets. Interestingly, the edges of the 2H-MoS<sub>2</sub> have been observed to be more conductive and posited to be inherently more catalytically active.<sup>4-5</sup> However, practical implementation of metallic 1T-MoS<sub>2</sub> has not been pursued. Although exfoliated MoS<sub>2</sub> has been investigated for hydrodesulfurization catalysis,<sup>21</sup> the high temperature conditions would cause their quick conversion back to the 2H phase, since 1T-MoS<sub>2</sub> is only metastable below 95 °C.<sup>10b</sup> Here, the phase identity and metallic conduction of 1T-MoS<sub>2</sub> are confirmed by Raman spectroscopy (Figure 2.4b), electron diffraction (Figure 2.5e), and CSAFM (Figure 2.4f).

The advantage of the 1T-MoS<sub>2</sub> nanosheets becomes more apparent when we use electrochemical impedance spectroscopy (EIS) to investigate electrode kinetics under HER operating conditions. Nyquist plots (Figure 2.6d) and data fittings reveal dramatically decreased charge transfer resistances for the exfoliated MoS<sub>2</sub> nanosheets on graphite (4 Ω) in contrast to the as-grown MoS<sub>2</sub> nanostructures on graphite (232 Ω). Furthermore, the small series resistances observed in all samples (~4 Ω) illustrates the importance of the direct synthesis on conductive substrates, which enables simple and effective electrical integration which minimizes

parasitic Ohmic losses.<sup>22</sup> The evidence afforded by structural characterization and impedance spectroscopy demonstrate exfoliated metallic 1T-MoS<sub>2</sub> nanosheets exhibit more facile electrode kinetics particularly useful in enhancing catalytic activity, representing unique features not previously demonstrated in other efforts aimed at improving MoS<sub>2</sub> for HER catalysis.<sup>4-5,6-7,9</sup>

#### ***2.4.4 Electrocatalytic Stability of chemically exfoliated MoS<sub>2</sub> nanosheets***

We demonstrate that the catalytic performance of 1T-MoS<sub>2</sub> nanosheets is stable, even though the 1T-phase is thermodynamically metastable. After 1000 cycles of continuous operation, exfoliated MoS<sub>2</sub> nanosheets show less than 15 % decay in the electrocatalytic current density (Figure 2.6e). Further EIS studies (Figure 2.6f) show that the slight loss in catalytic activity is accompanied by a slight increase in charge transfer resistance. Additional stability test shows the required overpotential to sustain a constant 10 mA/cm<sup>2</sup> increases by only 10 mV after 9 h of continuous service (Figure 2.8).

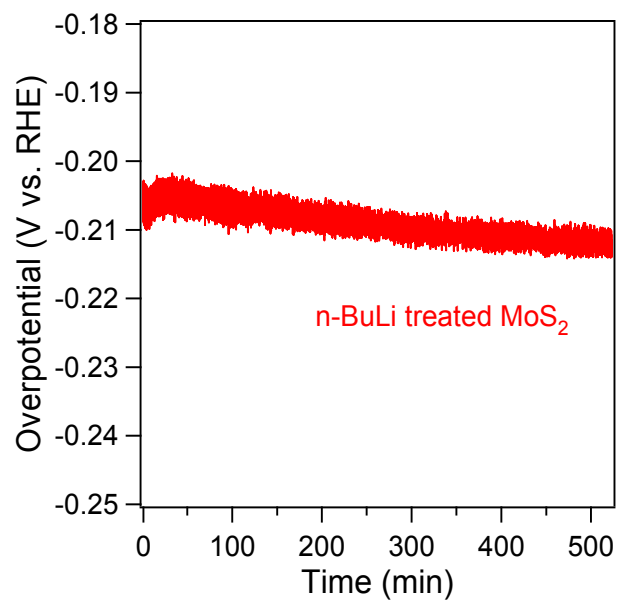


**Figure 2.8** The required overpotential (without  $iR$  correction) to achieve a constant electrocatalytic current of  $10 \text{ mA/cm}^2$  increases by only 10 mV after 9 h of continuous catalytic operation, which further demonstrates the electrocatalytic stability of 1T-MoS<sub>2</sub> nanosheets.

The minimal loss in catalytic activity suggests the metallic 1T polymorph is slowly reconverting to the semiconducting 2H phase. This hypothesis is further supported by longer phase stability studies where we monitored HER activity in exfoliated MoS<sub>2</sub> nanosheets aged over 3 weeks in ambient conditions with corresponding impedance and Raman spectroscopy measurements on the same samples (Figure 2.9). No decay in catalytic activity is observed within the first few days. Only after 7 days of aging is a noticeable decline in catalytic activity seen. Even after 21 days, the sample still retains more than 50 % of the initial maximum current density at -400 mV vs RHE, which is still a dramatic improvement over the as-grown nanostructures. EIS shows a slight increase in charge transfer resistance that suggests the slow reversion back to 2H polymorph may be responsible for the decline in catalytic performance. Raman spectroscopy shows a gradual suppression of the characteristic 1T peaks and resurgence of the 2H peaks, which corroborates the conversion hypothesis. Furthermore, we intentionally annealed the exfoliated 1T-MoS<sub>2</sub> nanosheets at 300 °C in argon for 5 min after aging the sample at room temperature for 21 days. PXRD shows re-emergence of the (002) diffraction peak after annealing (Figure 2.99d) and Raman spectroscopy shows enhanced signal intensity corresponding to the characteristic 2H peaks (Figure 2.9e). The expected drop in catalytic performance and accompanied large charge transfer resistance is observed in the respective polarization (purple diamond symbols in Figure 2.9a, c) and EIS measurements (Figure 2.9b, largest semi-circle). These data suggest that annealing at 300 °C not only results in the ordered restacking of the exfoliated MoS<sub>2</sub> nanosheets, but also transforms MoS<sub>2</sub> nanostructures from the 1T polymorph back to the 2H polymorph. Interestingly, this annealed sample still exhibits slightly enhanced HER activity compared to the original MoS<sub>2</sub> nanostructures (Figure 2.9a), which is likely due to residual 1T polymorph.

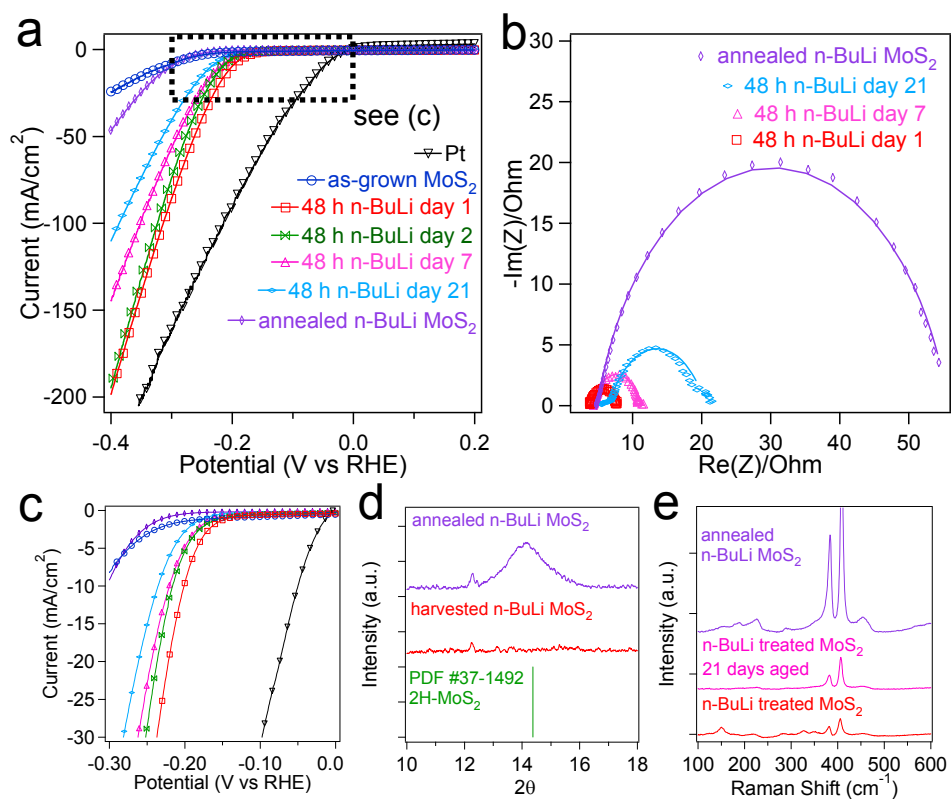


**Figure 2.9.** (a) Polarization curves showing the overall electrocatalytic stability and (c) performance at lower overpotential for 1T-MoS<sub>2</sub> nanosheets that have been aged in ambient conditions for various times over the course of 21 days. (b) Nyquist plots from EIS measurements show the corresponding slight increase in charge transfer resistance as the 1T-MoS<sub>2</sub> nanosheets are aged over the course of 21 days and then finally, annealed in argon at 300 °C. (d) PXRD results confirm the product has converted back to the restacked 2H polymorph after the MoS<sub>2</sub> nanosheets are intentionally annealed in argon at 300 °C for 5 min. (e) Raman spectroscopy showing the disappearance of the 1T peak shifts and resurgence of 2H peak shifts further supports the reconversion hypothesis as the samples are aged and intentionally annealed.

## 2.5 Conclusion

In conclusion, we demonstrate a simple and rational method to significantly enhance the electrocatalytic performance of MoS<sub>2</sub> by controlling its nanostructures and structural polymorphs using chemical exfoliation. This completely different approach to enhancing catalysis leads to favorable kinetics, metallic conductivity, and active site proliferation in the exfoliated 1T-MoS<sub>2</sub> nanosheets, which enable the superior yet stable catalytic activity and make MoS<sub>2</sub> nanostructures a highly competitive earth-abundant catalyst for HER and potentially other reactions. Furthermore, this represents the first application of the metallic 1T polymorph of layered metal chalcogenides in catalysis and this general approach to controlling nanostructures and polymorphism can be useful in modifying many 2D layered materials to enhance their applications in heterogeneous catalysis, solar energy, and high-performance electronics.

## 2.6 References

- (1) (a) Turner, J. A. *Science* **2004**, *305*, 972; (b) Lewis, N. S.; Nocera, D. G. *Proc. Natl. Acad. Sci. U. S. A.* **2006**, *103*, 15729.
- (2) McKone, J. R.; Warren, E. L.; Bierman, M. J.; Boettcher, S. W.; Brunschwig, B. S.; Lewis, N. S.; Gray, H. B. *Energ Environ Sci* **2011**, *4*, 3573.
- (3) Chianelli, R. R.; Siadati, M. H.; De la Rosa, M. P.; Berhault, G.; Wilcoxon, J. P.; Bearden, R.; Abrams, B. L. *Cataly Rev* **2006**, *48*, 1.
- (4) Laursen, A. B.; Kegnaes, S.; Dahl, S.; Chorkendorff, I. *Energ Environ Sci* **2012**, *5*, 5577.
- (5) (a) Jaramillo, T. F.; Jørgensen, K. P.; Bonde, J.; Nielsen, J. H.; Horch, S.; Chorkendorff, I. *Science* **2007**, *317*, 100; (b) Hinnemann, B.; Moses, P. G.; Bonde, J.; Jørgensen, K. P.; Nielsen, J. H.; Horch, S.; Chorkendorff, I.; Nørskov, J. K. *J. Am. Chem. Soc.* **2005**, *127*, 5308; (c) Bonde,

- J.; Moses, P. G.; Jaramillo, T. F.; Norskov, J. K.; Chorkendorff, I. *Faraday Discuss.* **2009**, *140*, 219; (d) Li, Y.; Wang, H.; Xie, L.; Liang, Y.; Hong, G.; Dai, H. *J. Am. Chem. Soc.* **2011**, *133*, 7296; (e) Vrubel, H.; Merki, D.; Hu, X. *Energ Environ Sci* **2012**, *5*, 6136.
- (6) (a) Merki, D.; Fierro, S.; Vrubel, H.; Hu, X. *Chem Sci* **2011**, *2*, 1262; (b) Benck, J. D.; Chen, Z.; Kuritzky, L. Y.; Forman, A. J.; Jaramillo, T. F. *ACS Catal* **2012**, *2*, 1916.
- (7) Karunadasa, H. I.; Montalvo, E.; Sun, Y.; Majda, M.; Long, J. R.; Chang, C. J. *Science* **2012**, *335*, 698.
- (8) Tenne, R.; Redlich, M. *Chem. Soc. Rev.* **2010**, *39*, 1423.
- (9) (a) Kibsgaard, J.; Chen, Z.; Reinecke, B. N.; Jaramillo, T. F. *Nat. Mater.* **2012**, *11*, 963; (b) Kong, D.; Wang, H.; Cha, J. J.; Pasta, M.; Koski, K. J.; Yao, J.; Cui, Y. *Nano Lett.* **2013**, *13*, 1341.
- (10) (a) Py, M. A.; Haering, R. R. *Can. J. Phys.* **1983**, *61*, 76; (b) Wypych, F.; Schollhorn, R. *J. Chem. Soc., Chem. Commun.* **1992**, *0*, 1386; (c) Yang, D.; Sandoval, S. J.; Divigalpitiya, W. M. R.; Irwin, J. C.; Frindt, R. F. *Phys Rev B* **1991**, *43*, 12053.
- (11) (a) Wang, Q. H.; Kalantar-Zadeh, K.; Kis, A.; Coleman, J. N.; Strano, M. S. *Nat Nano* **2012**, *7*, 699; (b) Chhowalla, M.; Shin, H. S.; Eda, G.; Li, L.-J.; Loh, K. P.; Zhang, H. *Nat Chem* **2013**, *5*, 263.
- (12) Novoselov, K. S.; Jiang, D.; Schedin, F.; Booth, T. J.; Khotkevich, V. V.; Morozov, S. V.; Geim, A. K. *Proc. Natl. Acad. Sci. U. S. A.* **2005**, *102*, 10451.
- (13) (a) Joensen, P.; Frindt, R. F.; Morrison, S. R. *Mater. Res. Bull.* **1986**, *21*, 457; (b) Coleman, J. N.; Lotya, M.; O'Neill, A.; Bergin, S. D.; King, P. J.; Khan, U.; Young, K.; Gaucher, A.; De, S.; Smith, R. J.; Shvets, I. V.; Arora, S. K.; Stanton, G.; Kim, H.-Y.; Lee, K.; Kim, G. T.; Duesberg, G. S.; Hallam, T.; Boland, J. J.; Wang, J. J.; Donegan, J. F.; Grunlan, J. C.; Moriarty,

- G.; Shmeliov, A.; Nicholls, R. J.; Perkins, J. M.; Grieveson, E. M.; Theuwissen, K.; McComb, D. W.; Nellist, P. D.; Nicolosi, V. *Science* **2011**, *331*, 568.
- (14) Murphy, D. W.; Di Salvo, F. J.; Hull, G. W.; Waszczak, J. V. *Inorg. Chem.* **1976**, *15*, 17.
- (15) (a) Bierman, M. J.; Lau, Y. K. A.; Kvit, A. V.; Schmitt, A. L.; Jin, S. *Science* **2008**, *320*, 1060; (b) Lau, Y. K. A.; Chernak, D. J.; Bierman, M. J.; Jin, S. *J. Am. Chem. Soc.* **2009**, *131*, 16461.
- (16) Jiménez Sandoval, S.; Yang, D.; Frindt, R. F.; Irwin, J. C. *Phys Rev B* **1991**, *44*, 3955.
- (17) Benavente, E.; Santa Ana, M. A.; Mendizábal, F.; González, G. *Coord. Chem. Rev.* **2002**, *224*, 87.
- (18) Eda, G.; Fujita, T.; Yamaguchi, H.; Voiry, D.; Chen, M.; Chhowalla, M. *ACS Nano* **2012**, *6*, 7311.
- (19) Merki, D.; Vrubel, H.; Rovelli, L.; Fierro, S.; Hu, X. *Chem Sci* **2012**, *3*, 2515.
- (20) Ge, P.; Scanlon, M. D.; Peljo, P.; Bian, X.; Vubrel, H.; O'Neill, A.; Coleman, J. N.; Cantoni, M.; Hu, X.; Kontturi, K.; Liu, B.; Girault, H. H. *Chem. Commun.* **2012**, *48*, 6484.
- (21) Miremadi, B. K.; Morrison, S. R. *J. Catal.* **1987**, *103*, 334.
- (22) Faber, M. S.; Park, K.; Cabán-Acevedo, M.; Santra, P. K.; Jin, S. *J. Phys. Chem. Lett.* **2013**, *4*, 1843.

## Chapter 3

# High-Performance Catalytic Hydrogen Evolution from Metallic WS<sub>2</sub> Nanosheets\*

### 3.1 Abstract

Building upon our recent discovery of enhanced hydrogen evolution catalysis from chemically exfoliated molybdenum disulfide (MoS<sub>2</sub>) nanosheets, here we develop metallic tungsten disulfide (WS<sub>2</sub>) nanosheets as extraordinarily active catalysts for the hydrogen evolution reaction (HER). By overcoming the challenges that have traditionally limited the catalytic performance of WS<sub>2</sub>, our 1T-WS<sub>2</sub> nanosheets achieve an electrocatalytic current density of 10 mA/cm<sup>2</sup> at the remarkably low potential of -142 mV vs. RHE. We believe this unprecedented performance represents a new benchmark for non-precious metal hydrogen evolution catalysts. Additionally, we develop a simple microwave method that allows us to avoid the time-consuming and cumbersome intercalation reactions while still producing 1T-WS<sub>2</sub> nanosheets exhibiting equivalently impressive catalytic activity.

---

\* This chapter was prepared for publication in collaboration with A.S. Daniel, C. R. English, F. Meng, A. Foricaux, R. J. Hamers, and S. Jin before being adapted here.

## 3.2 Introduction

Replacing rare and expensive catalysts, such as platinum, with earth-abundant materials continues to be a strong driving force behind contemporary research.<sup>1</sup> Layered metal chalcogenides ( $\text{MX}_2$ ) are an exciting family of compounds which consist of individual two-dimensional (2D) layers stacked to form hexagonal structures held together by only weak van der Waals interactions. Although the molybdenum disulfide ( $\text{MoS}_2$ ) analog is more well known, tungsten disulfide ( $\text{WS}_2$ ) also exhibits promising activity for the hydrogen evolution reaction (HER).<sup>2</sup> Experimental<sup>3</sup> and computational<sup>4</sup> studies show catalytically active sites are located along the edges of the 2D  $\text{MX}_2$  layers while the basal surfaces are catalytically inert. Not surprisingly,  $\text{WS}_2$  falls victim to many of the same issues that have traditionally limited the performance of  $\text{MoS}_2$  in the HER including the density and reactivity of active sites and poor electrical contact to the electrocatalyst.<sup>2c,5</sup> Building upon our recent report of enhanced hydrogen evolution from chemically exfoliated  $\text{MoS}_2$  nanosheets,<sup>6</sup> here we develop metallic 1T- $\text{WS}_2$  nanosheets as an extraordinarily active catalyst for the HER capable of achieving 10  $\text{mA}/\text{cm}^2$  electrocatalytic current density at the extremely low potential of  $-142$  mV vs. RHE. Moreover, we also demonstrate that required intercalation times can be significantly reduced using a simple microwave-assisted reaction method.

### 3.3 Experimental Section

#### 3.3.1 Synthesis of WS<sub>2</sub> nanostructures

Tungsten foils (0.05 mm thick,  $\sim 1 \text{ cm}^2$ ) were cleaned by sonication in acetone, isopropyl alcohol, and 18 M $\Omega$  deionized water for 10 min each before they were dried using nitrogen flow. Recycled tungsten substrates were first subjected to an aqua regia etch (3:1 concentrated HCl: concentrated HNO<sub>3</sub>) for 10 min to remove remnant materials and ensure a consistent reaction substrate. In a home-built CVD reactor consisting of a 1 inch fused silica tube equipped with pressure and gas flow controls placed in a single-zone tube furnace, an alumina combustion boat charged with 50 mg tungsten chloride (WCl<sub>6</sub>, 99.9 %) and 200 mg elemental sulfur (99.5 %) was placed outside of the tube furnace upstream of the prepared tungsten substrates. The reactor was evacuated and flushed three times with argon before it was back filled to the set-point pressure of 770 Torr under an argon flow of 125 sccm and heated to 550 °C. The combustion boat were pushed into the mouth of the furnace (1.5 cm) using a magnet and hydrogen flow was started at 0.75 sccm to initiate the reaction which lasts 20 min, then the furnace was cooled naturally under argon flow.

#### 3.3.2 *n*-Butyl lithium exfoliation treatment

Inside an argon-filled glove box, the substrates covered with as-synthesized WS<sub>2</sub> nanostructures were soaked in 3 mL *n*-butyllithium (2.7 M in heptane) inside sealed vials for 48 h which could be brought out of the glove box and heated to 80 °C inside an oven. Bulk WS<sub>2</sub> powder (99 %, 2  $\mu\text{m}$  particle size) was used as received from Sigma-Aldrich. Microwave-assisted intercalation reactions were carried out using a CEM microwave (Discover and Explorer) equipped with temperature probe and control used to maintain the reaction at 80 °C for

10-60 min using approximately 200 W power. Excess *n*-butyllithium was removed by rinsing the treated samples with dry heptane, then the samples were reacted with excess 18 M $\Omega$  deionized water. After reaction, the WS<sub>2</sub> nanosheets in water were centrifuged in an Eppendorf 5415D tabletop centrifuge at 13,200 rpm for 15 min. The supernatant was removed, and this washing procedure was repeated twice more with 18 M $\Omega$  deionized water to ensure complete reaction of intercalation lithium before the nanosheets were suspended in 1 mL of isopropyl alcohol.

### 3.3.3 Structural characterization

SEM was performed using a LEO Supra55 VP microscope operating at 3 kV. PXRD data were collected on harvested nanostructures dispersed on glass substrates using a Bruker D8 advanced powder diffractometer with Cu K $\alpha$  radiation and the background from glass substrate was subtracted. TEM samples were prepared by gentle sonication and drop-casting onto lacey carbon supported TEM grids. HRTEM of the WS<sub>2</sub> nanostructures and nanosheets was performed using an aberration-corrected FEI Titan scanning transmission electron microscope operated at an accelerating voltage of 200 kV in TEM mode. Raman spectra were taken using a Thermo Scientific DXR confocal Raman microscope using a 532 nm excitation laser. AFM measurements were taken on samples cast onto evaporated gold (50 nm) on Si(100)/SiO<sub>2</sub> substrates using an Agilent 5500 AFM equipped with current-sensing capabilities using a symmetric Pt coated tip (30 nm, mikroMasch) with a force constant of 2.7 N/m. All of the data is collected in the trace, with no significant hysteresis in the retrace, as current-sensing requires the AFM to be operated in contact mode. X-ray photoelectron spectroscopy (XPS) was performed on a custom-built XPS system (Phi Electronics, Eden Prairie, MN), that included a

model 10-610 Al  $K_{\alpha}$  x-ray source (1486.6 eV photon energy) and a model 10-420 toroidal monochromator. A model 10-360 hemispherical analyzer with a 16-channel detector array was used that under effective operating conditions had an analyzer resolution of 0.4 eV. Electrons were collected at an emission angle of  $45^{\circ}$  from the surface normal of the sample. High resolution data was collected for W ( $4f$ ), S ( $2p$ ), O ( $1s$ ) and C ( $1s$ ). The high resolution data were fit to Voigt functions in order to determine binding energies after being shifted so that the Au  $4f_{7/2}$  peak was at 84.0 eV. Ultraviolet photoelectron spectroscopy (UPS) was performed on the same custom-built system as was used to perform XPS. The analyzer resolution for UPS measurements was 0.09 eV. Negative biases ( $-7$  V) were applied to the samples to overcome the work function of the analyzer. A linear background correction was applied to the UPS data before doing any data workup. Platinum foil was used to determine the Fermi level for the system by fitting the valence band maximum edge to the Fermi function. The UPS spectra were then shifted to account for the negative bias applied as well as to place  $E_F$  equal to 0 eV. The valence band maximum edge for the  $WS_2$  samples were fit to lines and the x-axis intercept was used to determine the valence band maximum for each sample.

### ***3.3.4 Electrochemical characterization***

Electrochemical measurements were performed using a rotating disk electrode (BASi, RDE-2) in a three-electrode electrochemical cell using a Bio-Logic SP-200 potentiostat. All measurements were performed in 50 mL of 0.5 M  $H_2SO_{4(aq)}$  electrolyte (pH = 0.16) prepared using 18 M $\Omega$  deionized water purged with  $H_2$  gas (99.999%), using  $WS_2$  deposited graphite disks as the working electrode, a graphite rod as a counter electrode, and a saturated calomel (SCE) reference electrode (CH Instruments). As-grown 2H- $WS_2$  nanostructures grown directly

on graphite disks and harvested 2H-WS<sub>2</sub> nanostructures drop-cast onto graphite disks exhibited similar catalytic activities. Spectroscopically pure graphite rods (99.9995%, Ultra F purity, Ultra Carbon Corporation) cut into thin disks (6 mm diameter; ~0.4 mm thick) were polished to a near-mirror finish using abrasive cloths. They are sonicated subsequently in 18 MΩ deionized water for 10 min, then in aqua regia (3:1 concentrated HCl: concentrated HNO<sub>3</sub>) for 10 min (to remove remnant metal impurities), and then in 18 MΩ deionized water for 10 min again, before they were dried in an oven at 120 °C for 20 min. The WS<sub>2</sub> cast onto graphite disks (2 × 3 μL drops) were mounted on top of the embedded glassy carbon RDE electrodes using colloidal silver paint (Ted Pella). As a comparison, a standard Pt disc (4 mm diameter, Ted Pella) was mounted to the glassy carbon RDE electrode using the same method. The reversible hydrogen electrode (RHE) was calibrated using platinum as both working and counter electrodes to +0.260 V vs. the SCE reference. The performance of the hydrogen evolution catalyst is measured using linear sweep voltammetry beginning at +0.30 V and ending at -0.45 V vs. RHE with a scan rate of 3 mV/s when the working electrode is rotated at 2000 rpm. Electrochemical impedance spectroscopy was performed when the working electrode was biased at a constant -0.250 V vs. RHE while sweeping the frequency from 5 MHz to 10 mHz with a 10 mV AC dither. The impedance data were fit to a simplified Randles circuit to extract the series and charge transfer resistances. The electrochemical stability of the catalyst was evaluated by cycling the electrode 500 times; each cycle started at +0.10 V and ended at -0.45 V vs. RHE with a scan rate of 50 mV/s while rotating the working electrode at 2000 rpm. Cyclic voltammograms taken with various scan rates (20, 40, 60 mV/s, etc.) were used to estimate the double-layer capacitance were collected in the 0.1–0.2 V vs. RHE region.

## 3.4 Results and Discussion

### *3.4.1 Synthesis and characterization of as-grown WS<sub>2</sub> Nanostructures*

Our strategy begins with the simple chemical vapour deposition (CVD) of flower-like WS<sub>2</sub> nanostructures with a high density of exposed edges. Similar to our unique CVD method for producing 3D nanostructured MoS<sub>2</sub>,<sup>7</sup> the mild synthesis conditions make the deposition of WS<sub>2</sub> possible on many different substrates including fluorine-doped tin oxide on glass, graphite, and tungsten foils. Our tuneable synthetic method offers an important advantage in that our WS<sub>2</sub> nanostructures are dominated by edges, thus increasing the density of active sites (Figure 3.1b). Lattice resolved high-resolution transmission electron microscopy (HRTEM) show highly crystalline multilayered nanostructures (Figure 3.1c) which are not inorganic fullerenes (Figure 3.1d). The corresponding selected-area electron diffraction (SAED) pattern is unequivocally indexed to 2H-WS<sub>2</sub> (Figure 3.1e). The phase identity and purity of the as-synthesized WS<sub>2</sub> nanostructures is further confirmed using Raman spectroscopy (Figure 3.1j) and powder X-ray diffraction (Figure 3.1k).

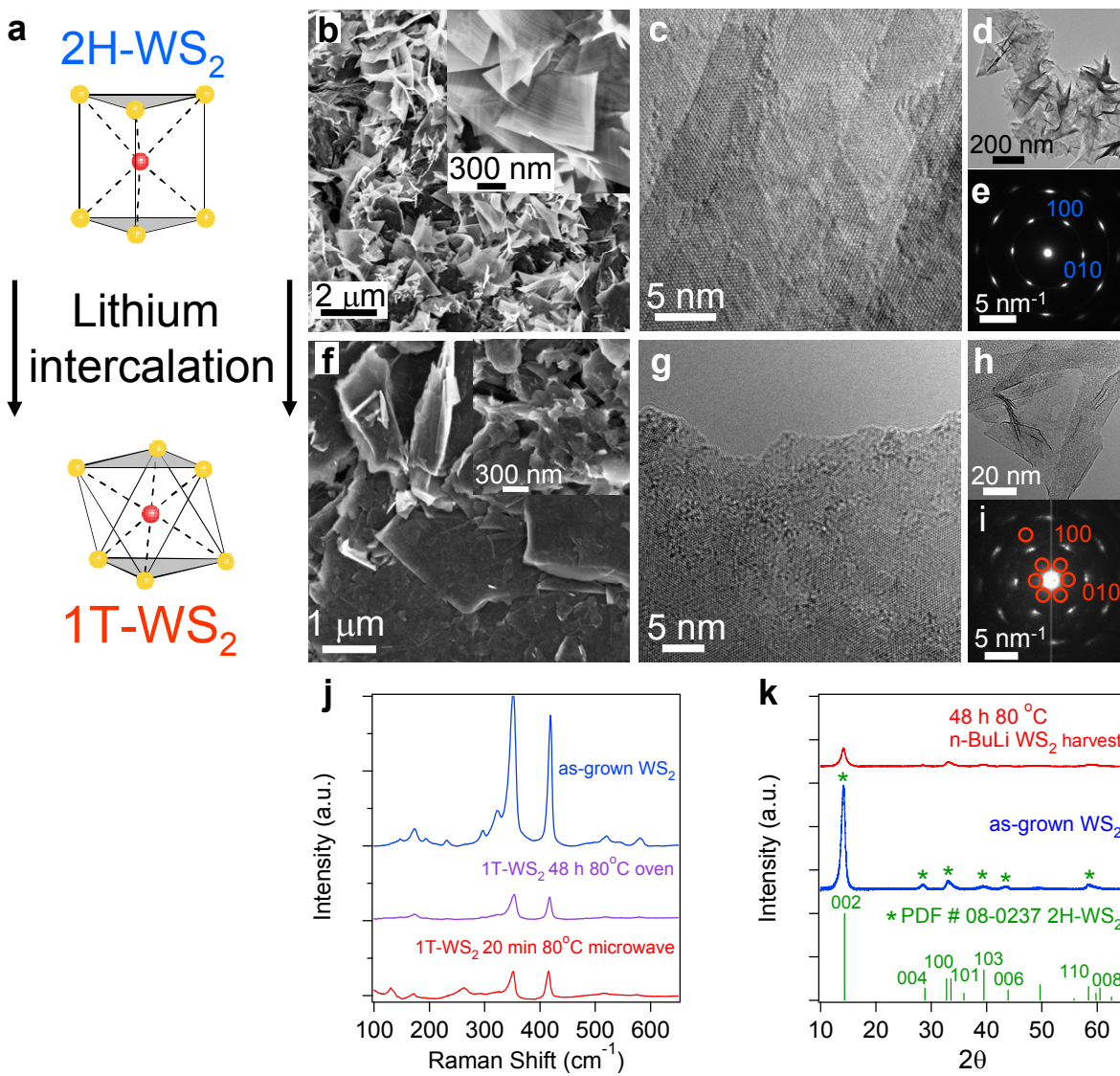


**Figure 3.1.** (a) Simple intercalation chemistry is used to facilitate the phase transformation to the 1T-WS<sub>2</sub> polymorph. Top-down SEM images of the (b) as-grown nanostructures on W foil and (f) chemically exfoliated nanosheets cast on graphite. Insets illustrate the high density of exposed edges. HRTEM of the (c) as-grown nanostructures and (g) chemically exfoliated nanosheets. Lower resolution images (d, h) confirm they are open structures (not inorganic fullerenes) and electron diffraction patterns confirm phase identity for the (e) 2H-WS<sub>2</sub> nanostructures and (i) 1T-WS<sub>2</sub> nanosheets. (j) Raman spectroscopy and (k) PXRD also confirm phase and purity.

### 3.4.2 Lithium Intercalation and Exfoliated Nanosheet Characterization

We then use simple intercalation chemistry to control the polymorph behavior in  $\text{MX}_2$  materials.<sup>7</sup> Electron transfer from intercalated lithium destabilizes the semiconducting and thermodynamically favored trigonally prismatic 2H structure, causing a transition to the octahedrally coordinated 1T polymorph (Figure 3.1a). The layered material is chemically exfoliated upon reaction with excess water, which generates  $\text{H}_2$ , and produces individual 1T- $\text{WS}_2$  nanosheets. Lithium intercalation of  $\text{MX}_2$  materials can be accomplished through either chemical (using n-butyllithium)<sup>6,8</sup> or electrochemical methods.<sup>9</sup> It is important to note that other exfoliation methods, such as mechanical cleavage<sup>10</sup> or liquid-phase sonication,<sup>11</sup> are limited to isolating single layers of the semiconducting 2H phase. Here, we convert our as-grown  $\text{WS}_2$  nanostructures to the metallic 1T- $\text{WS}_2$  polymorph by reacting the substrates with n-butyllithium for 48 h in vials sealed under a protective atmosphere at slightly elevated temperatures (80 °C) to help facilitate the intercalation process, which is known to be more difficult for  $\text{WS}_2$  than  $\text{MoS}_2$ .<sup>12</sup> Additionally, we develop a new microwave-assisted method to dramatically expedite the intercalation process and avoid the cumbersome 48 h reaction.<sup>13</sup> Remarkably, we find chemically exfoliated 1T- $\text{WS}_2$  nanosheets produced after only 20 min of microwave-assisted intercalation are nearly equivalent to those produced after 48 h of traditional oven intercalation.

Despite its strong similarities to  $\text{MoS}_2$ , we observed surprisingly unique behaviour in the exfoliation of  $\text{WS}_2$  nanosheets. Specifically, the violent generation of  $\text{H}_2$  caused the exfoliated nanosheets to delaminate from graphite (and other) substrates. We were able to overcome this obstacle by using tungsten foils as substrates for especially dense  $\text{WS}_2$  nanostructure growth, thereby significantly improving the yield of exfoliated nanosheets. After harvest, the chemically exfoliated nanosheets can be drop-cast onto any substrate. This approach also allows us to

minimize waste, as the tungsten foils can be cleaned and re-used in subsequent reactions. SEM shows a uniform film composed of many smaller sheets and particles still dominated by edges covering a graphite disk (Figure 3.1f). HRTEM shows the strained lattice of the exfoliated nanosheets (Figure 3.1g) and confirms they are still open structures (Figure 3.1h). The superlattice structure observed in the SAED pattern (Figure 3.1i red circles) is consistent with past reports of chemically exfoliated 1T-WS<sub>2</sub><sup>2f,14</sup> and suggests the product may be a mixture of 1T- and 2H-WS<sub>2</sub>. Raman spectroscopy is less sensitive to the structural transition, but the characteristic peaks for the 2H phase are much less intense and significantly broadened, which is in agreement with previous reports and similar to our own study of 1T-MoS<sub>2</sub> (Figure 3.1j).<sup>16</sup> Given the more difficult intercalation reaction and the propensity of chemically exfoliated nanosheets to restack into their thermodynamically favoured 2H phase,<sup>14b,14c</sup> it is likely that both the 1T and 2H polymorphs coexist in our chemically exfoliated samples. PXRD further supports this hypothesis, showing weakened reflections corresponding to the 2H polymorph (Figure 3.1k).

We further characterized the 1T-WS<sub>2</sub> nanosheets and highlight their differences from the 2H-WS<sub>2</sub> phase using X-ray photoelectron spectroscopy (XPS), Ultraviolet photoelectron spectroscopy (UPS), and current-sensing atomic force microscopy (CSAFM). X-ray photoelectron spectra of the W *4f* (Figure 3.2a) and S *2p* (Figure 3.2b) edges shows the presence of new chemical species clearly shifted toward lower binding energies after chemical exfoliation. These results are consistent with the known metallic nature of 1T-WS<sub>2</sub> and similar to past XPS studies on 1T-MX<sub>2</sub> materials.<sup>8a,8d,15</sup> The small shoulder at ~35 eV corresponding to the W *4f*<sub>7/2</sub> species (Figure 3.2a) confirms that the exfoliated 1T-WS<sub>2</sub> nanosheets are more susceptible to oxidation.<sup>12</sup> All XPS spectra are aligned with respect to the Au *4f* peak at 84.0 eV and the C *1s* peak is used to insure charging effects are not present (Figure A2.1). The more metallic

character of the chemically exfoliated nanosheets is also reflected in the UPS spectra (Figure 3.2c, 3.2d) for the 1T- and 2H-WS<sub>2</sub> nanosheets. The 1T-WS<sub>2</sub> nanosheets exhibit a valence band maximum (VBM) at 0.3 eV, which is much closer to the Fermi level (defined here as 0 eV) than the 0.9 eV VBM observed for the 2H-WS<sub>2</sub> nanostructures. We also use CSAFM to confirm the semiconducting-to-metallic phase transition. Contact mode topography (Figure 3.2g, 3.2h), friction, and deflection images (Figure A2.2) show the presence of material cast onto an evaporated gold on silicon substrate. Conductivity maps taken at +20 mV sample bias show the 2H-WS<sub>2</sub> nanostructures are much more resistive (Figure 3.2e) than the more uniformly conducting 1T-WS<sub>2</sub> nanosheets (Figure 3.2f). Individual current–voltage sweeps on specific nanostructures further contrast the clear differences in conductivity observed for the 1T- and 2H-WS<sub>2</sub> samples (Figure 3.2i).

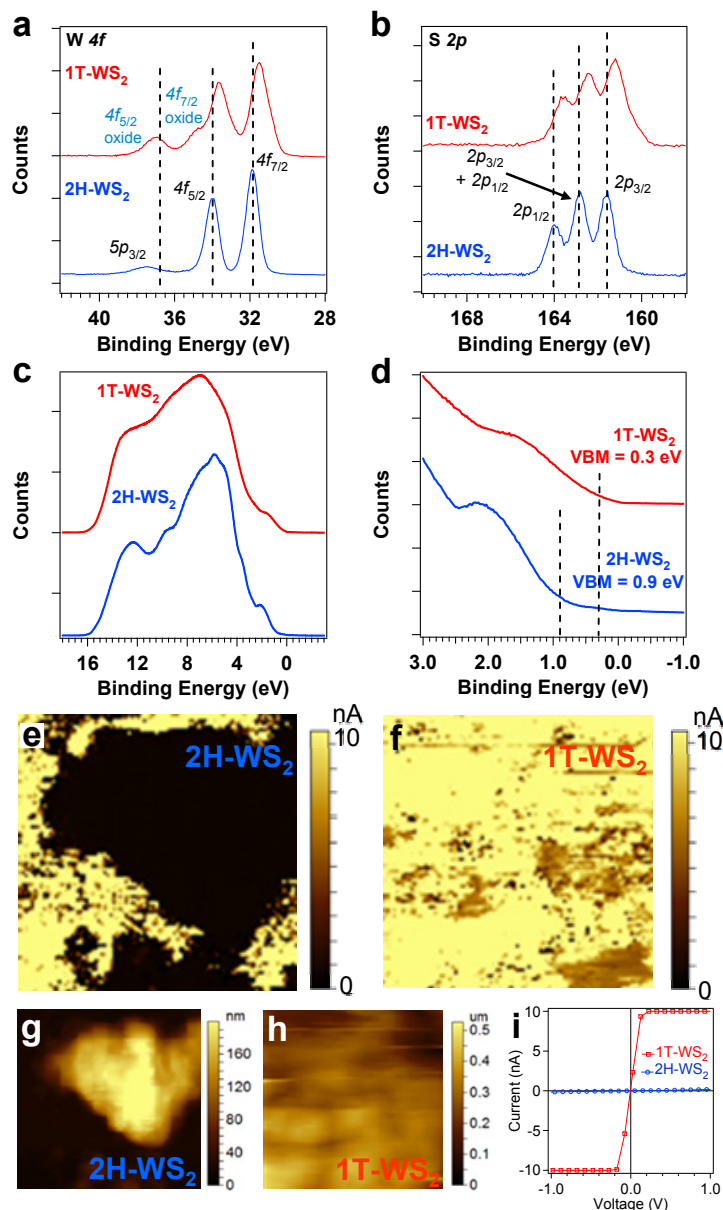


**Figure 3.2.** XPS spectra of the (a)  $W4f$  and (b)  $S2p$  edges, showing a new chemical species at lower binding energies after chemical exfoliation. (c-d) UPS spectra showing the valence band maxima with respect to the Fermi Level. (e-h) CSAFM micrographs and corresponding conductivity maps for the as-grown (e, g) and chemically exfoliated (f, h)  $WS_2$  nanosheets. All images are  $2\ \mu\text{m}$  by  $2\ \mu\text{m}$  and the conductivity maps were taken at a  $+20\ \text{mV}$  bias. (i) Current–voltage curves on individual nanostructures.

### 3.4.3 Electrocatalytic Performance of as-grown and chemically exfoliated WS<sub>2</sub> nanosheets

We demonstrate that our chemical exfoliation produces 1T-WS<sub>2</sub> nanosheets that exhibit extraordinary catalytic activity for the HER. We drop-cast the exfoliated 1T-WS<sub>2</sub> nanosheets onto graphite disks and evaluate their catalytic activity using a standard rotating disk electrode apparatus in a three-electrode electrochemical measurement. Polarization curves (Figure 3.3a) of the electrocatalytic current density ( $j$ ) plotted against potential vs. the reversible hydrogen electrode (RHE) show the HER activity of 1T-WS<sub>2</sub> nanosheets obtained from both oven and microwave-assisted intercalation methods compared to the as-grown WS<sub>2</sub> nanostructures. The advantages of our harvesting method become obvious after comparing these data with the poor catalytic activity exhibited by samples where growth and exfoliation were carried out on a single graphite substrate (Figure A2.3). As-grown WS<sub>2</sub> exhibits an onset of HER activity at approximately  $-200$  mV vs. RHE and significant hydrogen evolution ( $j = 10$  mA/cm<sup>2</sup>) is not reached until  $-330$  mV vs. RHE. 1T-WS<sub>2</sub> nanosheets that have been exfoliated after lithium intercalation at  $80$  °C for 48 h show dramatically improved HER activity where the onset of catalytic activity has been shifted to significantly lower voltages. After correcting for  $iR$  losses, our 1T-WS<sub>2</sub> nanosheets achieve  $10$  mA/cm<sup>2</sup> electrocatalytic current density at an unprecedented  $-142$  mV vs. RHE. To the best of our knowledge, this is the smallest requisite potential to achieve  $j = 10$  mA/cm<sup>2</sup> for any non-platinum (or other precious metal) catalyst. Remarkably, chemically exfoliated 1T-WS<sub>2</sub> nanosheets produced after only 20 min of microwave-assisted intercalation exhibit nearly equivalent performance, where  $j = 10$  mA/cm<sup>2</sup> is reached at  $-151$  mV vs. RHE. We further highlight the exceptional catalytic activity by comparing the 1T-WS<sub>2</sub> nanosheets against other high performing HER catalysts (Figure 3.3a).

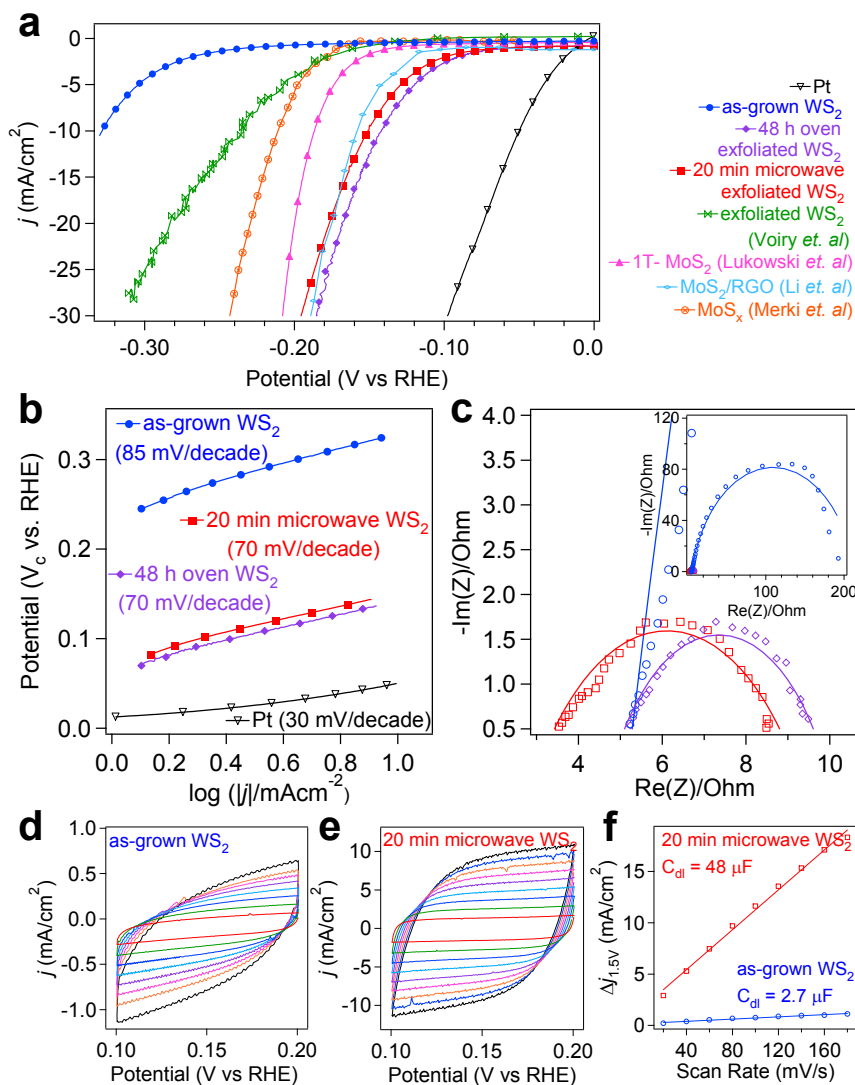


**Figure 3.3.** Electrocatalytic performance of the as-grown and chemically exfoliated WS<sub>2</sub>.

Polarization curves comparing the high-performance HER catalysis from 1T-WS<sub>2</sub> nanosheets with other non-precious metal catalysts. (b) Corresponding Tafel plots further reflect the dramatic improvement in catalytic activity after exfoliation. The filled points show the data after *iR* correction. (d) EIS Nyquist plots show the facile electrode kinetics of the 1T-WS<sub>2</sub> nanosheets. Voltammograms of the (e) as-grown and (f) chemically exfoliated WS<sub>2</sub> nanosheets at various scan rates used to estimate the  $C_{dl}$  and relative surface area.

The enhanced HER activity is further illustrated by comparing the Tafel slopes (Figure 3.3b) of the 1T-WS<sub>2</sub> nanosheets (70 mV/decade after *iR* correction for both oven and microwave intercalation) with the as-grown WS<sub>2</sub> nanostructures (85 mV after *iR* correction). The earlier onset of catalytic activity and lower Tafel slope suggests the free energy of hydrogen adsorption for 1T-WS<sub>2</sub> is closer to equilibrium. Additionally, we use electrochemical impedance spectroscopy (EIS) to investigate the electrode kinetics under the catalytic HER operating conditions. Nyquist plots and data fittings (Figure 3.3c) reveal dramatically reduced charge-transfer resistances ( $R_{ct}$ ) for the chemically exfoliated WS<sub>2</sub> nanosheets (6  $\Omega$  for the oven intercalation; 5  $\Omega$  for the microwave intercalation) in contrast to the as-grown WS<sub>2</sub> nanostructures (200  $\Omega$ ). Moreover, the small series resistances observed for all samples illustrates that our simple method enables high-quality electrical integration of the catalyst which minimizes Ohmic losses.<sup>17</sup> The polarization and EIS data confirm that 1T-WS<sub>2</sub> nanosheets are a highly active catalyst which exhibit facile electrode kinetics particularly useful for enhancing catalytic hydrogen evolution.<sup>6</sup>

We also estimate the relative differences in electrochemically active surface area before and after chemical exfoliation using a simple cyclic voltammetry method.<sup>18</sup> Current response in the potential window used for the cyclic voltammograms (0.1–0.2 V vs. RHE) at different scan rates should be due only to the charging of the double-layer (Figure 3.3d, 3.3e). The double-layer capacitances ( $C_{dl}$ ) for the chemically exfoliated and as-grown samples, which should be directly proportional to the surface area, are extracted by plotting the  $\Delta J$  ( $J_a - J_c$ ) at a given potential (0.15 V vs. RHE) against the cyclic voltammograms scan rates (Figure 3.3f). The slope of this linear relationship is twice the  $C_{dl}$  for each sample, respectively. The proliferation of active sites due to chemical exfoliation is illustrated by the more than an order-of-magnitude

increase in  $C_{dl}$  for the 1T-WS<sub>2</sub> nanosheets (48  $\mu\text{F}$ ) as compared to the as-grown 2H-WS<sub>2</sub> nanostructures (2.7  $\mu\text{F}$ ). While this increase in surface area certainly contributes to the improved performance, we believe the transition to the metallic polymorph is more important to enhancing the catalytic activity. This is consistent with recent results showing exfoliated semiconducting 2H-MoS<sub>2</sub> nanosheets exhibited only marginally improved activity,<sup>19</sup> suggesting that the number of active edge sites is not the most important factor behind improving the catalytic performance of related MX<sub>2</sub> materials.

The catalytic performance of the WS<sub>2</sub> nanosheets was examined as a function of the duration of microwave-assisted intercalation (Figure 3.4). The as-synthesized WS<sub>2</sub> nanostructures on tungsten foils from the same CVD synthesis were microwaved in 2.7 M *n*-butyl lithium in heptane at 80 °C for 10, 20, 30, and 60 min before rinsing away the excess *n*-butyl lithium with dry hexane/heptane, and subsequently reacting them with excess 18 MΩ deionized water, thus removing the intercalated lithium and exfoliating the WS<sub>2</sub> nanosheets, which causes their full delamination from the W foils that they can be harvested and isolated by centrifugation. Significant improvement in catalytic performance compared to the as-grown WS<sub>2</sub> nanostructures are observed for samples from all intercalation conditions. Prolonged microwave-assisted reactions (60 min) produced less catalytically active materials, possible due to the oxidation of the 1T-WS<sub>2</sub> nanosheets. We chose 20 min as the standard microwave-assisted intercalation time at 80°C for the balance of performance and reaction efficiency (Figure 3.4).

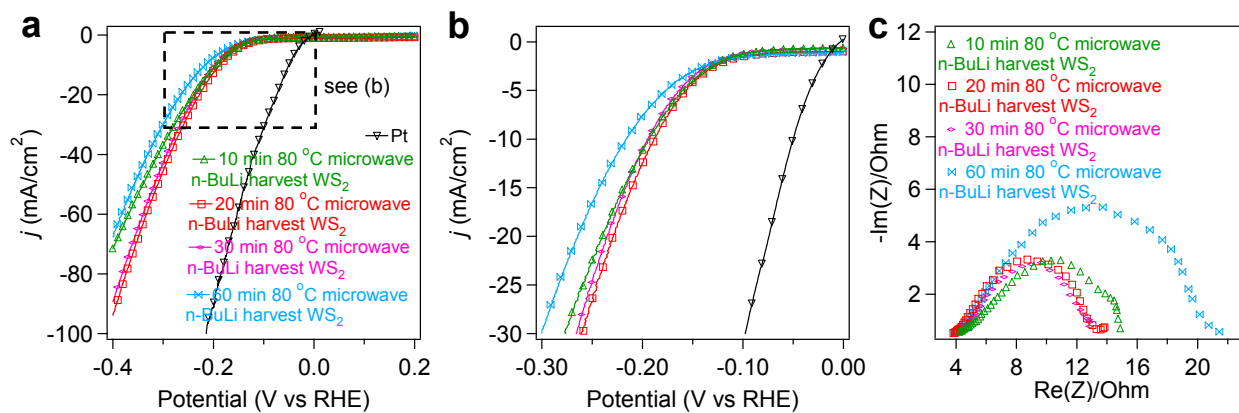


**Figure 3.4.** Polarization curves showing the (a) overall catalytic activity and (b) performance at lower potentials as a function of microwave intercalation duration at 80 °C in 2.7 M *n*-butyl lithium in heptane. (c) Nyquist plots show the corresponding trends in electrode kinetics.

#### ***3.4.4 Comparison of chemically exfoliated nanostructures and bulk powder***

The importance of choosing to chemically exfoliate our well controlled CVD synthesized WS<sub>2</sub> nanostructures reflected by their superior catalytic performance for the HER as compared to commercially available bulk WS<sub>2</sub> powder subjected to the same intercalation conditions (20 min microwave-assisted reaction at 80 °C) (Figure 3.5a, 3.5b). This claim is also supported by comparing the catalytic activity of the CVD grown nanostructures with the as-received bulk powder. EIS shows the attempt to exfoliate the bulk powder results in behavior most similar to our CVD synthesized WS<sub>2</sub> nanostructures (Figure 3.5c). Data fittings reveal charge transfer resistances ( $R_{ct}$ ) of 192  $\Omega$  for the "exfoliated" bulk powder and 1919  $\Omega$  for the as-received powder (c.f. 200  $\Omega$  for the CVD synthesized WS<sub>2</sub>). In comparison, the exfoliated 1T-WS<sub>2</sub> nanosheets from the CVD synthesized nanostructures exhibit much more facile kinetics ( $R_{ct} = 5 \Omega$ ). The dramatic difference in catalytic activity can likely be explained by the incomplete lithiation, conversion, and exfoliation of larger particle ( $\sim 2 \mu\text{m}$ ) in the bulk powder. SEM images of the as-received (Figure 3.5d) and the "exfoliated" bulk powder (Figure 3.5e) further support this hypothesis. Lastly, PXRD (Figure 3.5f) and Raman spectroscopy (Figure 3.5g) also show minimal differences in the "exfoliated" material as compared to the as-received bulk powder, thereby confirming that most of the powder has not been transformed to the more catalytically active 1T polymorph. These results emphasize the CVD synthesized nanomaterials require much shorter intercalation times in order to achieve efficient conversion and subsequent exfoliation.

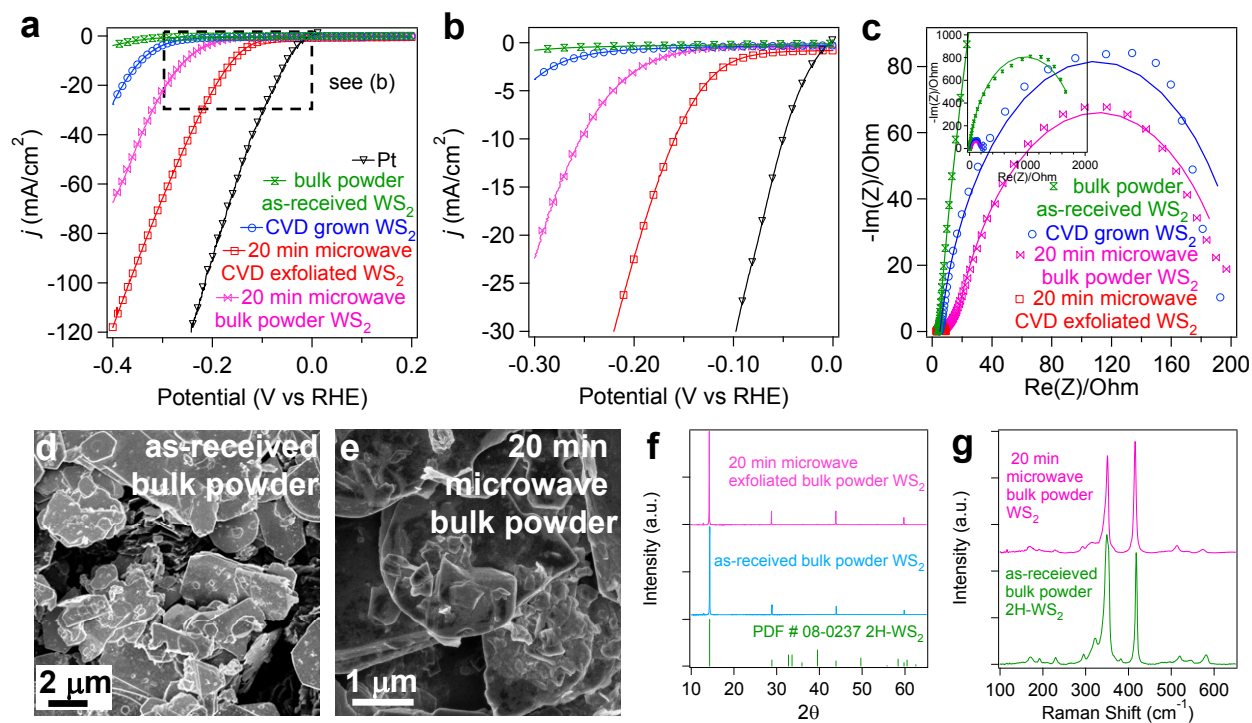


**Figure 3.5.** Polarization curves showing the superior (a) overall catalytic activity and (b) performance at lower potentials for chemically exfoliated nanosheets produced from CVD synthesized  $\text{WS}_2$  nanostructures compared to a commercial bulk  $\text{WS}_2$  powder exposed to the same intercalation and exfoliation conditions. (c) Nyquist plots show the corresponding trends in electrode kinetics. SEM images of the (d) as-received and (e) "exfoliated" bulk  $\text{WS}_2$  powder show the much larger particle sizes as compared to the CVD synthesized nanostructures. (f) PXRD and (g) Raman spectroscopy confirm the "exfoliated" bulk powder remains mostly in its 2H phase.

### ***3.4.5 Electrocatalytic Stability of chemically exfoliated WS<sub>2</sub> nanosheets***

We show the catalytic activity of 1T-WS<sub>2</sub> nanosheets is relatively stable although the 1T phase is metastable. We continuously cycle the 1T-WS<sub>2</sub> nanosheets over 500 times under the normal operating conditions and monitor the electrocatalytic performance (Figure 3.6a, 3.6b). In addition to monitoring the catalytic activity after continuous cycling, alternative stability test shows that the required potential to sustain a constant electrocatalytic current of 10 mA/cm<sup>2</sup> increases by ~80 mV after 4 h of continuous catalytic hydrogen evolution reaction in 0.5 M H<sub>2</sub>SO<sub>4</sub> (Figure 3.6c). The slight loss in catalytic activity is accompanied by an increase in charge transfer resistance, as revealed by EIS experiments (Figure 3.6d). This suggests a slow reversion to the thermodynamically favored 2H polymorph is responsible for the loss in catalytic activity, similar to our recent report on 1T-MoS<sub>2</sub> nanosheets.

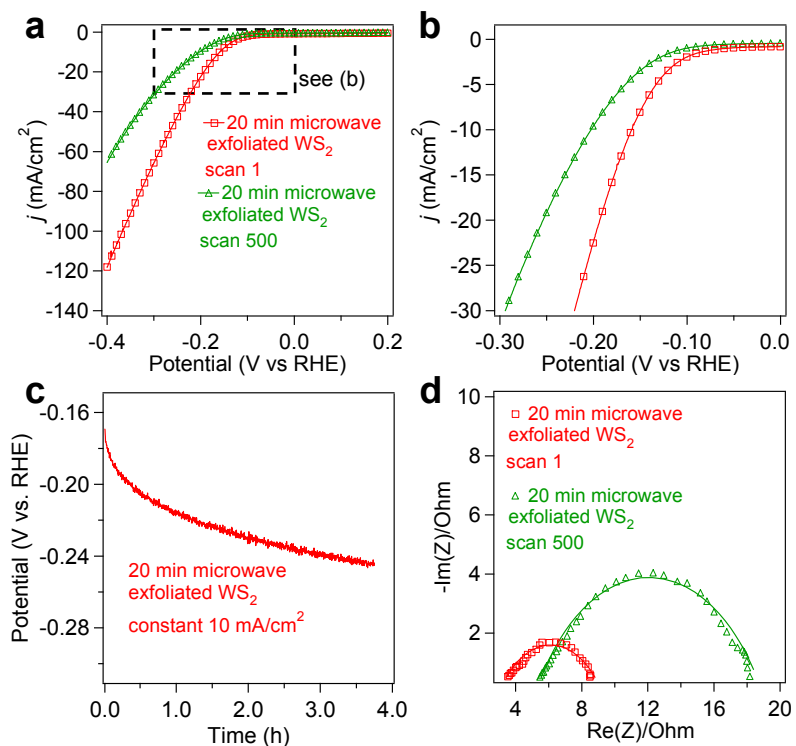


**Figure 3.6.** Polarization curves showing the catalytic stability of 1T-WS<sub>2</sub> nanosheets cycled continuously at (a) higher and (b) lower potentials. (c) The required potential to achieve a constant electrocatalytic current of 10 mA/cm<sup>2</sup> is plotted against time of continuous catalytic operation. (d) Nyquist plots show the slight increase in charge transfer resistance after continuous operation.

### 3.5 Conclusion

In conclusion, we have significantly enhanced the electrocatalytic activity of WS<sub>2</sub> for the HER by controlling its nanostructures and structural polymorphs. Moreover, we demonstrate that microwave intercalation chemistry can be used to avoid long cumbersome reaction times in excess of 48 h while still achieving equivalent performance. Additionally, this confirms our method is generally applicable to enhancing the applications of other materials within the MX<sub>2</sub> family. This approach leads to favourable kinetics, metallic conductivity, and active site proliferation in the chemically exfoliated 1T-WS<sub>2</sub> nanosheets, which enable its superior catalytic activity in the HER.

### 3.6 References

- (1) (a) Turner, J. A. *Science* **2004**, *305*, 972; (b) McKone, J. R.; Warren, E. L.; Bierman, M. J.; Boettcher, S. W.; Brunschwig, B. S.; Lewis, N. S.; Gray, H. B. *Energ Environ Sci* **2011**, *4*, 3573; (c) Chen, W.-F.; Sasaki, K.; Ma, C.; Frenkel, A. I.; Marinkovic, N.; Muckerman, J. T.; Zhu, Y.; Adzic, R. R. *Angew. Chem., Int. Ed.* **2012**, *51*, 6131.
- (2) (a) Wu, Z.; Fang, B.; Bonakdarpour, A.; Sun, A.; Wilkinson, D. P.; Wang, D. *Appl. Catal., B* **2012**, *125*, 59; (b) Bonde, J.; Moses, P. G.; Jaramillo, T. F.; Norskov, J. K.; Chorkendorff, I. *Faraday Discuss.* **2009**, *140*, 219; (c) Merki, D.; Hu, X. *Energ Environ Sci* **2011**, *4*, 3878; (d) Sobczynski, A.; Yildiz, A.; Bard, A. J.; Campion, A.; Fox, M. A.; Mallouk, T.; Webber, S. E.; White, J. M. *J. Phys. Chem.* **1988**, *92*, 2311; (e) Sobczynski, A.; Bard, A. J.; Campion, A.; Fox, M. A.; Mallouk, T. E.; Webber, S. E.; White, J. M. *J. Phys. Chem.* **1989**, *93*, 401; (f) Kim, J.; Byun, S.; Smith, A. J.; Yu, J.; Huang, J. *J. Phys. Chem. Lett.* **2013**, *4*, 1227.

- (3) Jaramillo, T. F.; Jørgensen, K. P.; Bonde, J.; Nielsen, J. H.; Horch, S.; Chorkendorff, I. *Science* **2007**, *317*, 100.
- (4) Hinnemann, B.; Moses, P. G.; Bonde, J.; Jørgensen, K. P.; Nielsen, J. H.; Horch, S.; Chorkendorff, I.; Nørskov, J. K. *J. Am. Chem. Soc.* **2005**, *127*, 5308.
- (5) Laursen, A. B.; Kegnaes, S.; Dahl, S.; Chorkendorff, I. *Energ Environ Sci* **2012**, *5*, 5577.
- (6) Lukowski, M. A.; Daniel, A. S.; Meng, F.; Forticaux, A.; Li, L.; Jin, S. *J. Am. Chem. Soc.* **2013**, *135*, 10274.
- (7) Huang, X.; Zeng, Z.; Zhang, H. *Chem. Soc. Rev.* **2013**, *42*, 1934.
- (8) (a) Voiry, D.; Yamaguchi, H.; Li, J.; Silva, R.; Alves, D. C. B.; Fujita, T.; Chen, M.; Asefa, T.; Shenoy, V. B.; Eda, G.; Chhowalla, M. *Nat. Mater.* **2013**, *advance online publication*; (b) Joensen, P.; Frindt, R. F.; Morrison, S. R. *Mater. Res. Bull.* **1986**, *21*, 457; (c) Yang, D.; Frindt, R. F. *J. Phys. Chem. Solids* **1996**, *57*, 1113; (d) Eda, G.; Yamaguchi, H.; Voiry, D.; Fujita, T.; Chen, M.; Chhowalla, M. *Nano Lett.* **2011**, *11*, 5111.
- (9) (a) Zeng, Z.; Yin, Z.; Huang, X.; Li, H.; He, Q.; Lu, G.; Boey, F.; Zhang, H. *Angew. Chem., Int. Ed.* **2011**, *50*, 11093; (b) Zeng, Z.; Sun, T.; Zhu, J.; Huang, X.; Yin, Z.; Lu, G.; Fan, Z.; Yan, Q.; Hng, H. H.; Zhang, H. *Angew. Chem., Int. Ed.* **2012**, *51*, 9052.
- (10) Novoselov, K. S.; Jiang, D.; Schedin, F.; Booth, T. J.; Khotkevich, V. V.; Morozov, S. V.; Geim, A. K. *Proc. Natl. Acad. Sci. U. S. A.* **2005**, *102*, 10451.
- (11) (a) Coleman, J. N.; Lotya, M.; O'Neill, A.; Bergin, S. D.; King, P. J.; Khan, U.; Young, K.; Gaucher, A.; De, S.; Smith, R. J.; Shvets, I. V.; Arora, S. K.; Stanton, G.; Kim, H.-Y.; Lee, K.; Kim, G. T.; Duesberg, G. S.; Hallam, T.; Boland, J. J.; Wang, J. J.; Donegan, J. F.; Grunlan, J. C.; Moriarty, G.; Shmeliov, A.; Nicholls, R. J.; Perkins, J. M.; Grievson, E. M.; Theuwissen,

K.; McComb, D. W.; Nellist, P. D.; Nicolosi, V. *Science* **2011**, *331*, 568; (b) Zhou, K.-G.; Mao, N.-N.; Wang, H.-X.; Peng, Y.; Zhang, H.-L. *Angew. Chem., Int. Ed.* **2011**, *50*, 10839.

(12) Miremadi, B. K.; Morrison, S. R. *J. Appl. Phys.* **1988**, *63*, 4970.

(13) Benavente, E.; González, G. *Mater. Res. Bull.* **1997**, *32*, 709.

(14) (a) Dungey, K. E.; Curtis, M. D.; Penner-Hahn, J. E. *Chem. Mater.* **1998**, *10*, 2152; (b) Tsai, H.-L.; Heising, J.; Schindler, J. L.; Kannewurf, C. R.; Kanatzidis, M. G. *Chem. Mater.* **1997**, *9*, 879; (c) Heising, J.; Kanatzidis, M. G. *J. Am. Chem. Soc.* **1999**, *121*, 638.

(15) Bhandavat, R.; David, L.; Singh, G. *J. Phys. Chem. Lett.* **2012**, *3*, 1523.

(16) Ramakrishna Matte, H. S. S.; Gomathi, A.; Manna, A. K.; Late, D. J.; Datta, R.; Pati, S. K.; Rao, C. N. R. *Angew. Chem.* **2010**, *122*, 4153.

(17) Faber, M. S.; Park, K.; Cabán-Acevedo, M.; Santra, P. K.; Jin, S. *J. Phys. Chem. Lett.* **2013**, *4*, 1843.

(18) Merki, D.; Vrubel, H.; Rovelli, L.; Fierro, S.; Hu, X. *Chem Sci* **2012**, *3*, 2515.

(19) Ge, P.; Scanlon, M. D.; Peljo, P.; Bian, X.; Vubrel, H.; O'Neill, A.; Coleman, J. N.; Cantoni, M.; Hu, X.; Kontturi, K.; Liu, B.; Girault, H. H. *Chem. Commun.* **2012**, *48*, 6484.

(20) Sekine, T.; Nakashizu, T.; Toyoda, K.; Uchinokura, K.; Matsuura, E. *Solid State Commun.* **1980**, *35*, 371.

## Chapter 4

# The Synthetic Development of Metal Chalcogenides and Exploration of Various Methods to Control their Phase Behavior

### 4.1 Abstract

The search for earth-abundant, efficient, and cost-effective catalysts for hydrogen evolution has led us to the exciting layered chalcogenide  $\text{MX}_2$  family of materials where catalytically active sites are located along the edges of their 2D layers. Here we develop a unique chemical vapor deposition method for the synthesis of nanostructured  $\text{MoS}_2$ ,  $\text{WS}_2$ ,  $\text{MoSe}_2$ ,  $\text{WSe}_2$ , and  $\text{ReS}_2$  materials dominated by edges on a variety of substrates. Additionally, we use simple intercalation chemistry to control the phase behavior of these  $\text{MX}_2$  materials and isolate the 1T phase which we show to be significantly more catalytically active for the hydrogen evolution reaction. Various intercalation methods are explored, including simply soaking the as-grown materials in n-butyllithium with gentle heating using either a traditional oven, or using a microwave-assisted method. Additionally, we also explore electrochemically driven intercalation within battery coin cells. Finally, we layout the fundamentals for further stabilizing the 1T phase using electron-donating impurity atoms.

## 4.2 Introduction

Layered metal chalcogenides are an exciting family of materials with the general  $\text{MX}_2$  formula, where M is a metal (Mo, W, etc.) and X is a chalcogen (S, Se, Te). Similar to graphene in graphite, these materials consist of individual two-dimensional (2D) layers stacked to form hexagonal structures held together by only weak van der Waals interactions. The strong interest in these 2D materials continues to be driven by the plethora of interesting physical phenomena exhibited when charge and heat transport is confined to a single plane.<sup>1-3</sup> Although much of the significant development in 2D materials has focused on graphene, many of these same approaches and paradigms can be applied to the  $\text{MX}_2$  family of compounds. In fact, the  $\text{MX}_2$  materials can be envisioned for many more applications due their more complex crystal structures and better intrinsic properties including, their band-gap which falls within the visible spectrum. These more diverse properties motivate much of the contemporary research on 2D  $\text{MX}_2$  materials aimed to integrate these unique materials into high-performance electronic, photonic, spintronic, thermal, and energy applications.<sup>4,5</sup> Herein we show the utility of  $\text{MoS}_2$ ,  $\text{MoSe}_2$ ,  $\text{WS}_2$ , and  $\text{WSe}_2$  as catalysts for the hydrogen evolution reaction and significant enhancement in their catalytic activity after controlling their nanostructures and polymorph behavior using simple intercalation chemistry.

$\text{MX}_2$  materials can exist in various polymorphs where subtle structural changes dramatically affect electrical properties (Figure 4.1).<sup>6-8</sup>  $\text{MoS}_2$ ,  $\text{WSe}_2$ , and their related analogs are found naturally in their semiconducting and thermodynamically favored 2H phase which is described by two X-M-X layers stacked in a repeating “ABAB” unit built from edge-sharing  $\text{MX}_6$  trigonal prisms. Other polymorphs, such as the 3R phase, are still semiconducting and trigonally prismatic structures, but differ slightly in the how the layers are stacked to form the

bulk structure. Single layers of the semiconducting material have been isolated using mechanical and chemical exfoliation methods. In contrast, the metallic 1T polymorph is described by a single X-M-X layer composed of edge-sharing  $\text{MX}_6$  octahedra, and is not naturally found in bulk. Intercalation of alkali metals, such as lithium, into the van der Waals gaps induces the phase change for  $\text{MX}_2$  materials such as  $\text{MoS}_2$  and  $\text{WS}_2$ . Electron transfer from the intercalated lithium  $s$  orbital into the  $d$  orbital of the transition metal destabilizes the trigonally prismatic 2H phase and favors the octahedrally coordinated 1T phase. The 1T polymorph is known to be metastable, even after removal of the intercalated lithium by reaction with excess water, which generates  $\text{H}_2$ , causing the exfoliation of the material into single layer nanosheets. Annealing or aging can expedite their transformation back into the thermodynamically favored 2H phase. It is important and interesting to note that for certain  $\text{MX}_2$  materials ( $\text{TaS}_2$  and  $\text{NbS}_2$ ), the 2H structure type is actually metallic. The structural parameters and pertinent physical properties for a variety of  $\text{MX}_2$  materials are presented in Table 4.1.

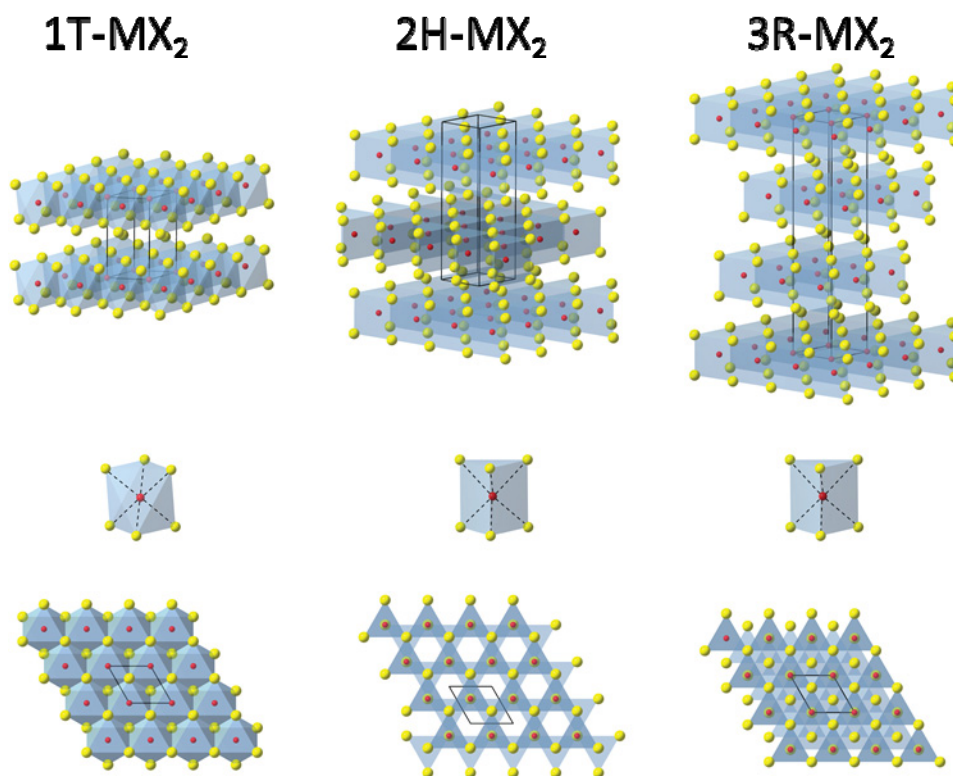


**Figure 4.1.** Crystal structure models illustrating the differences between the 1T-, 2H-, and 3R- $\text{MX}_2$  polymorphs, highlighting the octahedral and trigonal prismatic coordination and of the metal atoms. Projection along the  $c$ -axis reveals further contrast between the polymorphs. The 1T- $\text{MX}_2$  structure model was drawn using the crystallographic coordinates for the 1T- $\text{TiS}_2$ .

Compound	MoS <sub>2</sub>		WS <sub>2</sub>		MoSe <sub>2</sub>	WSe <sub>2</sub>	ZrS <sub>2</sub>	HfS <sub>2</sub>	TaS <sub>2</sub>	NbS <sub>2</sub>	TiS <sub>2</sub>	SnS <sub>2</sub>	SnSe <sub>2</sub>
Crystal System	2H	1T	2H	1T	2H	2H	1T	1T	2H	2H	1T	2T	2T
Lattice Constant a (Å)	3.161	3.27	3.154	3.32	3.287	3.286	3.662	3.635	3.313	3.31	3.407	3.648	3.81
Lattice Constant c/2 (Å)	6.149	n/a	6.181	n/a	6.463	6.492	5.813	5.837	6.034	5.945	5.6953	5.899	6.14
Bandgap (eV)	1.2 (1.8)	Metallic	1.4 (1.9)	Metallic	1.1 (1.5)	1.2 (1.7)	1.7	1.13	Metallic	Metallic	Semi-metal (1.0)	2.1	1.1

**Table 4.1.** Structural parameters and physical properties of a representative group of MX<sub>2</sub> materials. Band gaps listed in parenthesis correspond to the confinement effects observed for single layers.

Although  $\text{MX}_2$  materials have been traditionally used as hydrodesulfurization catalysts,<sup>9,10</sup> many exciting potential applications are envisioned for the future. More recently, especially with the focus on nanomaterials,  $\text{MX}_2$  materials have found applications as photo- and electrocatalysts for the hydrogen evolution reaction (HER).<sup>11-16</sup> Experimental<sup>11</sup> and computational<sup>17</sup> studies conclude the catalytically active sites are located along the edges of the 2D  $\text{MX}_2$  layers where atoms are undercoordinated and present dangling bonds for the chemi- and physisorption of species to be catalytically converted. In contrast, the basal surfaces are catalytically inert because the M-X bonds are completely satisfied. Although these edges are catalytically active, they are also thermodynamically unfavorable, which explains the propensity of  $\text{MX}_2$  to form closed-shell inorganic fullerene and nanotube structures when synthesized on the nanoscale.<sup>18</sup> While many other recent studies have focused on engineering the surface to maximize the density of active edge sites for catalysis,<sup>19-21</sup> this does not address the important issues of poor bulk conduction and anisotropic electrical transport which can limit the overall catalytic performance of  $\text{MX}_2$ . To overcome these challenges, we have taken the approach of controlling the synthesis of  $\text{MX}_2$  nanostructures dominated by edges and manipulating their polymorphs using simple intercalation chemistries to make  $\text{MX}_2$  nanosheets highly competitive earth-abundant catalysts for the HER.

## **4.3 Methods**

All chemicals were purchased from Sigma-Aldrich and used as-received unless otherwise noted.

### ***4.3.1 Growth substrate preparation***

Spectroscopically pure graphite rods (99.9995%, Ultra F purity, Ultra Carbon Corporation) cut into thin discs (6 mm diameter; ~0.4 mm thick) were polished to a near-mirror finish using abrasive cloths. They are sonicated subsequently in 18 M $\Omega$  deionized water for 10 min, then in aqua regia (3:1 concentrated HCl: concentrated HNO<sub>3</sub> for 10 min (to remove remnant metal impurities), and then in 18 M $\Omega$  deionized water for 10 min again, before they were dried in an oven at 120 °C for 20 min. Molybdenum foils (0.1 mm thick, ~ 1 cm<sup>2</sup>), fluorine-doped tin oxide on glass, Si(100)/SiO<sub>2</sub>, glass, and carbon paper were all cleaned by sonication in acetone, isopropyl alcohol, and 18 M $\Omega$  deionized water for 10 min each before they were dried using nitrogen flow. Recycled substrates were first subjected to an aqua regia etch (3:1 concentrated HCl: concentrated HNO<sub>3</sub>) for 10 min to remove remnant materials and insure a consistent reaction substrate.

#### ***4.3.2 Synthesis of MoS<sub>2</sub> nanostructures***

In a home-built CVD reactor consisting of a 1 inch fused silica tube equipped with pressure and gas flow controls placed in a single-zone tube furnace, alumina combustion boats charged with 50 mg molybdenum chloride (MoCl<sub>5</sub>, 95 %) and 200 mg elemental sulfur (99.5 %) were placed outside of the tube furnace upstream of the prepared graphite substrates. The reactor was evacuated and flushed three times with argon before it was back filled to the set-point pressure of 770 Torr under an argon flow of 125 sccm and heated to 525 °C. The MoCl<sub>5</sub> and sulfur boats were pushed into the mouth of the furnace (1.5 cm for MoCl<sub>5</sub> boat; 4.5 cm for sulfur boat) using a magnet to initiate the reaction which lasts 20 min, then the furnace was cooled naturally under argon flow.

#### ***4.3.3 Synthesis of WS<sub>2</sub> nanostructures***

In a home-built CVD reactor consisting of a 1 inch fused silica tube equipped with pressure and gas flow controls placed in a single-zone tube furnace, an alumina combustion boat charged with 50 mg tungsten chloride (WCl<sub>6</sub>, 99.9 %) and 200 mg elemental sulfur (99.5 %) was placed outside of the tube furnace upstream of the prepared tungsten substrates. The reactor was evacuated and flushed three times with argon before it was back filled to the set-point pressure of 770 Torr under an argon flow of 125 sccm and heated to 550 °C. The combustion boat were pushed into the mouth of the furnace (1.5 cm) using a magnet to initiate the reaction which lasts 20 min, then the furnace was cooled naturally under argon flow.

#### ***4.3.4 Synthesis of MoSe<sub>2</sub> nanostructures (Kyle Czech)***

In a home-built CVD reactor consisting of a 1 inch fused silica tube equipped with pressure and gas flow controls placed in a single-zone tube furnace, alumina combustion boats charged with 50 mg molybdenum chloride (MoCl<sub>5</sub>, 95 %) and 200 mg elemental selenium (99.5 %) were placed outside of the tube furnace upstream of the prepared graphite or molybdenum foil substrates. The reactor was evacuated and flushed three times with argon before it was back filled to the set-point pressure of 770 Torr under an argon flow of 125 sccm and heated to 600 °C. The MoCl<sub>5</sub> and sulfur boats were pushed into the mouth of the furnace (1.5 cm for MoCl<sub>5</sub> boat; 4.5 cm for sulfur boat) using a magnet and hydrogen flow was started at 0.75 sccm to initiate the reaction which lasts 20 min, and then the furnace was cooled naturally under argon flow.

#### ***4.3.5 Synthesis of WSe<sub>2</sub> nanostructures***

In a home-built CVD reactor consisting of a 1 inch fused silica tube equipped with pressure and gas flow controls placed in a single-zone tube furnace, an alumina combustion boat charged with 50 mg tungsten chloride ( $\text{WCl}_6$ , 99.9 %) and 200 mg elemental selenium (99.5 %) was placed outside of the tube furnace upstream of the prepared tungsten substrates. The reactor was evacuated and flushed three times with argon before it was back filled to the set-point pressure of 770 Torr under an argon flow of 125 sccm and heated to 550 °C. The combustion boat were pushed into the mouth of the furnace (1.5 cm) using a magnet to initiate the reaction which lasts 20 min, then the furnace was cooled naturally under argon flow.

#### ***4.3.6 Synthesis of $\text{ReS}_2$ nanostructures***

In a home-built CVD reactor consisting of a 1 inch fused silica tube equipped with pressure and gas flow controls placed in a single-zone tube furnace, alumina combustion boats charged with 50 mg rhenium chloride ( $\text{ReCl}_5$ , 95 %) and 200 mg elemental sulfur (99.5 %) were placed outside of the tube furnace upstream of the prepared graphite substrates. The reactor was evacuated and flushed three times with argon before it was back filled to the set-point pressure of 770 Torr under an argon flow of 125 sccm and heated to 525 °C. The  $\text{ReCl}_5$  and sulfur boats were pushed into the mouth of the furnace (1.5 cm for  $\text{ReCl}_5$  boat; 4.5 cm for sulfur boat) using a magnet to initiate the reaction which lasts 20 min, and then the furnace was cooled naturally under argon flow.

#### ***4.3.7 $n$ -Butyllithium intercalation and exfoliation***

Inside an argon-filled glove box, the substrates covered with as-synthesized  $\text{MX}_2$  nanostructures were soaked in 3 mL  $n$ -butyl lithium (2.7 M in heptane or 1.6 M in hexanes)

inside sealed vials for 6-48 h brought out of the glove box and could be heated to 60-80 °C. Bulk  $\text{MX}_2$  powder (99 %, 2  $\mu\text{m}$ ) was used as received from Sigma-Aldrich. Microwave reactions were carried out using a CEM microwave (Discover and Explorer) equipped with temperature control maintained automatically at 80 °C for 10-60 min using approximately 200 W power. Excess *n-butyllithium* was removed by rinsing the treated substrates with dry heptane, and then the substrates were reacted with excess 18 M $\Omega$  deionized water. For the  $\text{MoS}_2$  nanosheets on graphite, these substrates were used directly after a gentle rinse with water. Exfoliated  $\text{WS}_2$  nanosheets were harvested from nanostructures originally grown on W foils which efficiently delaminate from their substrates upon reaction with water after intercalation. To isolate nanosheets from metal foils, the  $\text{MX}_2$  nanosheets reacted in water were centrifuged in an Eppendorf 5415D tabletop centrifuge at 13,200 rpm for 15 min. The supernatant was removed, and the product was washed twice more with 18 M $\Omega$  deionized water to ensure complete reaction of intercalation lithium before being suspended in 1 mL of isopropyl alcohol.

#### **4.3.8 Battery coin cell lithiation and exfoliation**

As-grown  $\text{MX}_2$  nanostructures synthesized directly on spectroscopically pure graphite planchets (Ted Pella; 15 mm diameter  $\times$  1.6 mm thick) or carbon paper (Fuel Cell Earth, LLC; 15 mm diameter  $\times$  0.19 mm thick) were packed into a 2032-type coin cell using 1 M  $\text{LiPF}_6$  dissolved in 1:1 (v:v) ethyl carbonate(EC)/dimethyl carbonate (DMC) as the electrolyte, a polyethylene membrane, a lithium foil (>99%, 15.6 mm diameter; 0.45 mm thick) as the anode, a stainless steel spacer, and spring. After aging the cells overnight to ensure system equilibrium, typical open-circuit voltages of  $\sim$ 2.9 V were observed. Discharge and cycling tests were done on a multi-channel battery analyzer (MTI BST8-WA) operated using Neware software at room

temperature in a voltage window of 3.0-1.0 V vs.  $\text{Li}^+/\text{Li}$  under a constant current of  $100 \text{ mA g}^{-1}$  relative to the mass of  $\text{MX}_2$  as measured by an analytical microbalance. Discharged or cycled substrates were recovered by carefully opening the coin cells using pliers and gently rinsing the substrate with propylene carbonate to remove any adsorbed electrolyte. Substrates were then reacted gently using isopropyl alcohol, ethanol, methanol, and 18 M $\Omega$  water sequentially to minimize the loss of material due to violent  $\text{H}_2$  evolution while still ensuring all of the intercalated lithium was reacted.

#### ***4.3.9 Structural characterization***

SEM was performed using a LEO Supra55 VP microscope operating at 3 kV. PXRD data were collected using a Bruker D8 advanced powder diffractometer ( $\text{Cu K}\alpha$  radiation) on as-synthesized nanostructures still on their growth substrates (graphite, metal foil, etc.) or harvested nanostructures dispersed on glass substrates. Background from the glass substrate was subtracted where appropriate. TEM samples were prepared by gentle sonication and dropcasting onto lacey carbon supported TEM grids. HRTEM of the  $\text{MX}_2$  nanostructures and nanosheets was performed using an aberration-corrected FEI Titan scanning transmission electron microscope operated at an accelerating voltage of 200 kV in TEM mode. Electron diffraction of the exfoliated  $\text{MoS}_2$  nanosheets was collected using a FEI T12 microscope operated at an accelerating voltage of 120 kV. Raman spectra were taken using a Thermo Scientific DXR confocal Raman microscope using a 532 nm excitation laser.

#### ***4.3.10 Electrochemical characterization***

Electrochemical measurements were performed using a rotating disk electrode (BASi, RDE-2) in a three-electrode electrochemical cell using a Bio-Logic SP-200 potentiostat. All measurements were performed in 50 mL of 0.5 M  $\text{H}_2\text{SO}_{4(\text{aq})}$  electrolyte (pH = 0.16) prepared using 18 M $\Omega$  deionized water purged with  $\text{H}_2$  gas (99.999%), using  $\text{MX}_2$  on graphite disks as the working electrode, a graphite rod as a counter electrode, and a saturated calomel (SCE) reference electrode (CH Instruments). The  $\text{MX}_2$  grown directly or cast ( $2 \times 3 \mu\text{L}$  drops) onto graphite disks prepared as described for growth substrates were mounted on top of the embedded glassy carbon RDE electrodes using colloidal silver paint (Ted Pella). As a comparison, a standard Pt disc (4 mm diameter, Ted Pella) was mounted to the glassy carbon RDE electrode using the same method. The reversible hydrogen electrode (RHE) was calibrated using platinum as both working and counter electrodes to +0.260 V vs. the SCE reference. The performance of the hydrogen evolution catalyst is measured using linear sweep voltammetry beginning at +0.30 V and ending at -0.45 V vs. RHE with a scan rate of 3 mV/s when the working electrode is rotated at 2000 rpm. Electrochemical impedance spectroscopy was performed when the working electrode was biased at a constant -0.250 V vs. RHE while sweeping the frequency from 5 MHz to 10 mHz with a 10 mV AC dither. The impedance data were fit to a simplified Randles circuit to extract the series and charge transfer resistances. The electrochemical stability of the catalyst was evaluated by cycling the electrode at least 500 times; each cycle started at +0.10 V and ended at -0.45 V vs. RHE with a scan rate of 50 mV/s while rotating the working electrode at 2000 rpm. Cyclic voltammograms taken with various scan rates (20, 40, 60 mV/s, etc.) were used to estimate the double-layer capacitance were collected in the 0.1–0.2 V vs. RHE region.

#### 4.4 Results and Discussion

#### ***4.4.1 Synthesis of MX<sub>2</sub> nanostructures***

The chemical vapor deposition synthesis of MX<sub>2</sub> nanostructures takes advantage of the rich chemistry of volatile metal halides and elemental chalcogen precursors. Drawing on our previous experience for synthesizing complex, hierarchical nanostructures of other metal chalcogenides (PbS, PbSe, etc),<sup>22-24</sup> our optimized growth conditions enabled high-density deposition of MX<sub>2</sub> nanostructures on a variety of substrates. This highly tunable synthesis offers the distinct advantages of (i) the dense MX<sub>2</sub> flakes are dominated by edges (Figure 4.2), thus increasing the density of active sites, and (ii) the direct growth on conductive substrates (graphite, carbon paper, FTO, etc.) results in high-quality, low-electrical-loss contact to the 3D nanostructured catalyst.

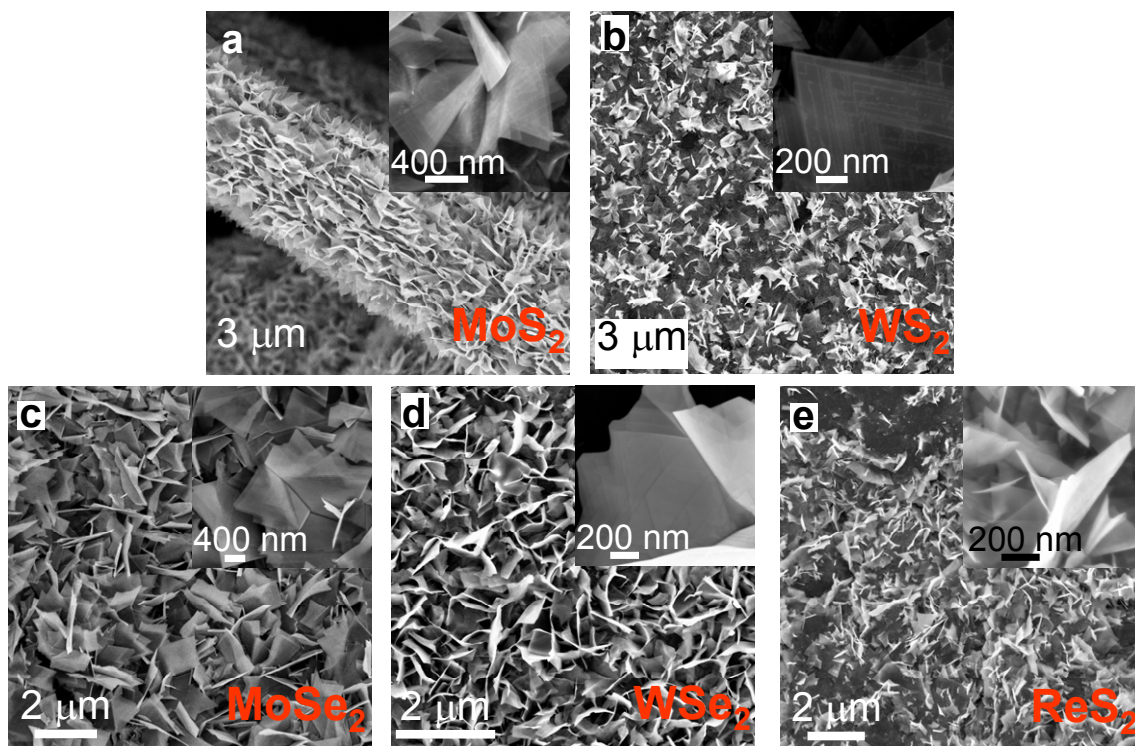


**Figure 4.2.** SEM images of as-grown (a)  $\text{MoS}_2$ , (b)  $\text{WS}_2$ , (c)  $\text{MoSe}_2$ , (d)  $\text{WSe}_2$ , and (e)  $\text{ReS}_2$  nanostructures

#### 4.4.2 *TEM characterization of MX<sub>2</sub> nanostructures*

TEM reveals the as-grown MX<sub>2</sub> nanostructures are highly crystalline and multilayered open structures (not inorganic fullerenes) which can be indexed unequivocally to their expected stable and thermodynamically favored 2H polymorphs. Not surprisingly, the nanostructures are often found along their [001] zone axis, but they can also be found along other stereographically similar axes. The HRTEM images show the nanoplates are well ordered with many edges making them especially appropriate for HER catalysis. MoS<sub>2</sub> (Figure 4.3a-c), WS<sub>2</sub> (Figure 4.3d-f), and WSe<sub>2</sub> (Figure 4.3g-i) nanostructures index to their [-111], [001], and [201] zone axes, respectively.

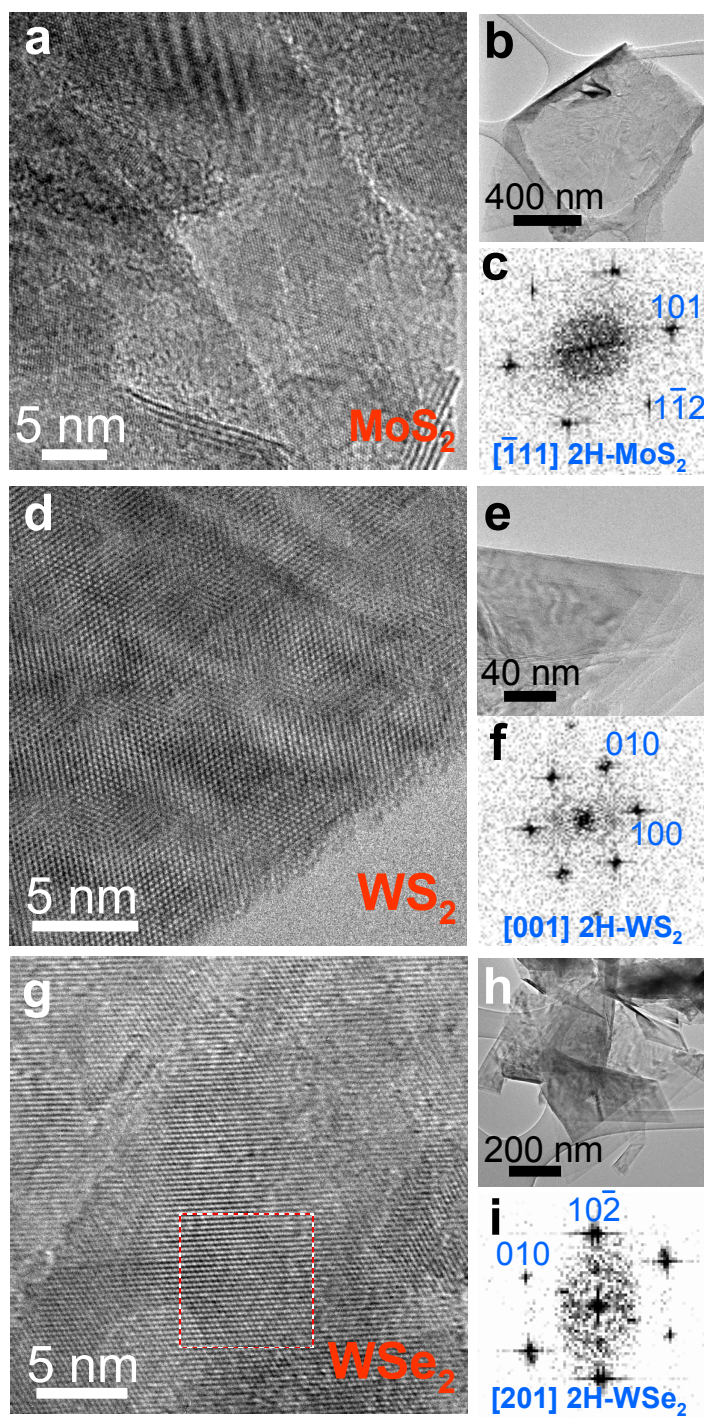


**Figure 4.3.** TEM images of as-grown (a-c) MoS<sub>2</sub>, (d-f) WS<sub>2</sub>, and (g-i) WSe<sub>2</sub> nanostructures with corresponding indexed electron diffraction or fast Fourier transform patterns.

#### 4.4.3 SEM and TEM characterization of exfoliated MX<sub>2</sub> nanosheets

Electron microscopy shows a clear difference in the materials after chemical exfoliation. SEM imaging reveals the overall nanosheet morphology is preserved and the nanostructures are still dominated by edges, although the chemically exfoliated MX<sub>2</sub> nanosheets are more disordered and compressed to their substrates (Figure 4.4a, e). The lack of contrast is also indicative of a change in their physical properties: they are now much more conductive, and therefore, do not differentially charge with respect to their underlying conductive substrates. TEM images confirm the nanosheets are still open structures, and have not changed into inorganic fullerenes (Figure 4.4c, g). In the case of MoS<sub>2</sub>, the exfoliated sheets are unstable under 200 kV imaging conditions (Figure 4.4b), making a HRTEM study impossible. The WS<sub>2</sub> nanosheets seem to be more stable during high-resolution imaging (Figure 4.4f). Careful electron diffraction study at lower accelerating voltages shows the expected symmetry and corresponding increase in lattice constant for both MoS<sub>2</sub> and WS<sub>2</sub> (Figure 4.4d, h).<sup>25,26</sup> The 1T-MoS<sub>2</sub> nanosheets are observed to be mostly phase pure. The electron diffraction from WS<sub>2</sub> nanosheets are more suggestive of a mixed phase product consisting of both 1T and 2H material. The superlattice reflections corresponding to the 1T phase in WS<sub>2</sub> are highlighted with red circles.

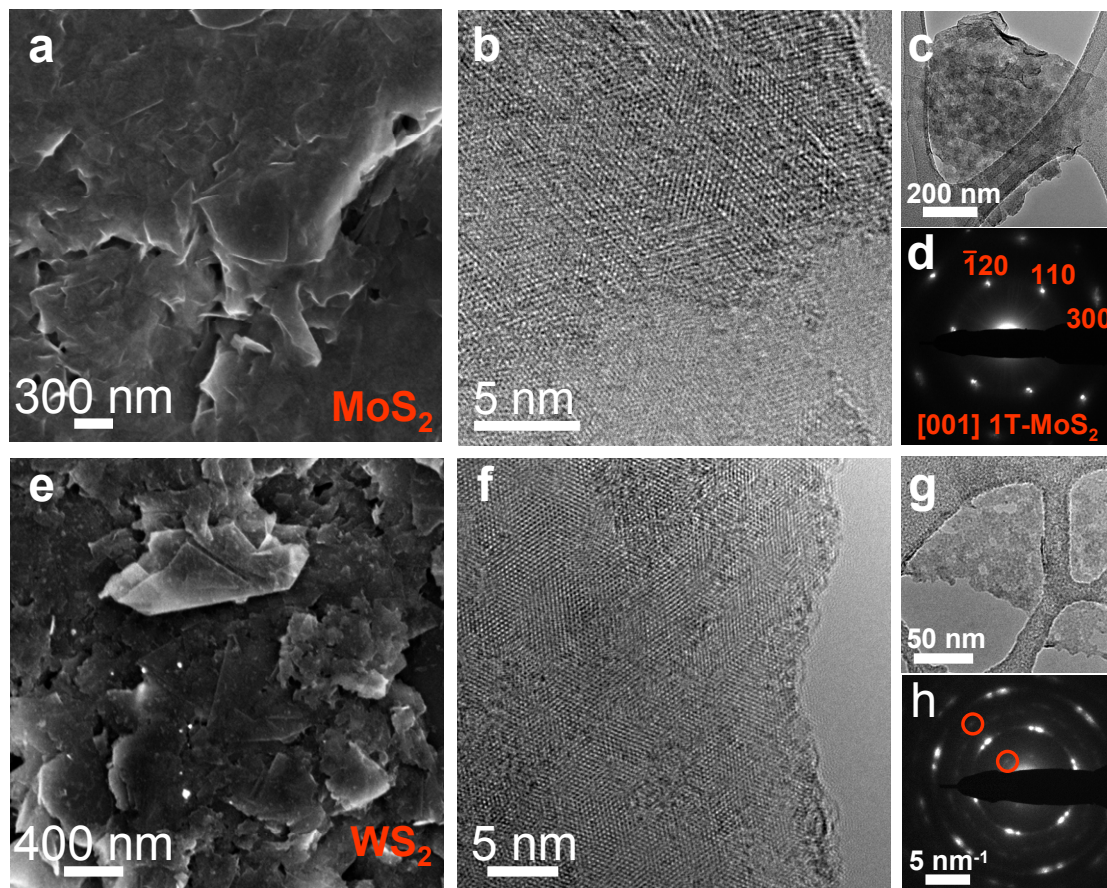


**Figure 4.4.** SEM and TEM images of exfoliated 1T nanosheets for (a-d) MoS<sub>2</sub> and (e-h) WS<sub>2</sub>.

#### ***4.4.4 PXRD characterization of as-grown MX<sub>2</sub> nanomaterials and their exfoliated nanosheets***

As-grown MX<sub>2</sub> materials on a variety of substrates (metal foils, graphite, harvested and dispersed on glass, etc.) were characterized using PXRD (Figure 4.5). For MoS<sub>2</sub> and WS<sub>2</sub>, sharp peaks corresponding to the graphite substrate (graphitic planchets or carbon papers) are also present. For MoSe<sub>2</sub>, the sharp peak near 58° corresponds to the Mo foil substrate. Strong reflections (i.e. (002), (004), etc) illustrate the long-range order of the as-grown nanostructures along the *c*-axis. From these results, it is clear that the as-grown nanostructures are phase-pure 2H-MX<sub>2</sub>. Interestingly, these reflections are completely destroyed after chemical exfoliation for MoS<sub>2</sub>, and severely diminished for WS<sub>2</sub>. This reflects the efficient exfoliation of the nanostructures into single sheets of the 1T polymorph which does not have a lattice constant along the *c*-axis since it is a 2D structure. In the case of WS<sub>2</sub>, the propensity of the 1T material to restack into its thermodynamically favored polymorph is confirmed by the presence of the (002) reflection.

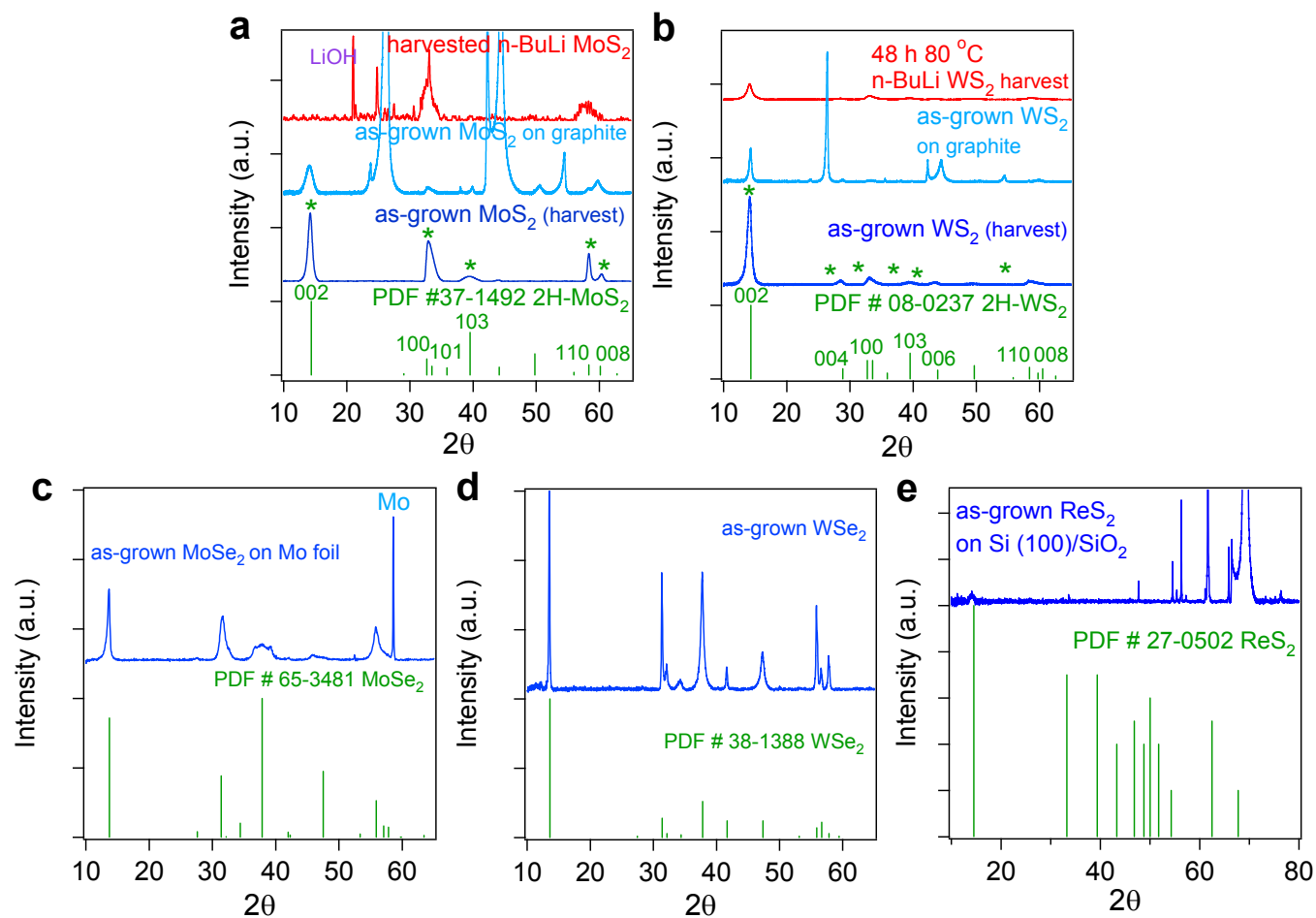


**Figure 4.5.** PXRD patterns for the as-grown and exfoliated (where available) nanostructures in (a) MoS<sub>2</sub>, (b) WS<sub>2</sub>, (c) MoSe<sub>2</sub>, (d) WSe<sub>2</sub>, and (e) ReS<sub>2</sub>.

#### ***4.4.5 Raman characterization of as-grown MX<sub>2</sub> nanomaterials and their exfoliated nanosheets***

As-grown MX<sub>2</sub> materials on a variety of substrates (metal foils, graphite, etc.) were characterized using Raman spectroscopy (Figure 4.8). Substrate choice does not influence the Raman signal as long as there are more than a few (1-4) layers of the MX<sub>2</sub> material. Strong characteristic peaks (e.g. 384 and 410 cm<sup>-1</sup> for MoS<sub>2</sub>) are seen for each material. After exfoliation, some materials show new peaks corresponding to the 1T phase and weakened peaks corresponding to the 2H polymorph. In all cases, the 2H peaks are broadened. For the case of MoS<sub>2</sub>, a phase pure 1T sample would be devoid of any peak at 383 cm<sup>-1</sup>, but new peaks arising at 156, 236, and 330 cm<sup>-1</sup> should be more prominent.<sup>27,28</sup> This near phase pure characteristic is seen for the MoS<sub>2</sub> grown on carbon paper and cycled in the coin cell (Figure 4.8a pink trace). This was never repeated, even for material grown on carbon planchets and cycled in the same manner. The Raman data also illustrate the utility of the microwave-assisted intercalation method, showing the same efficient conversion and exfoliation can be obtained in only a fraction of the time (20 min vs. 48 h) required for the oven heated intercalation.

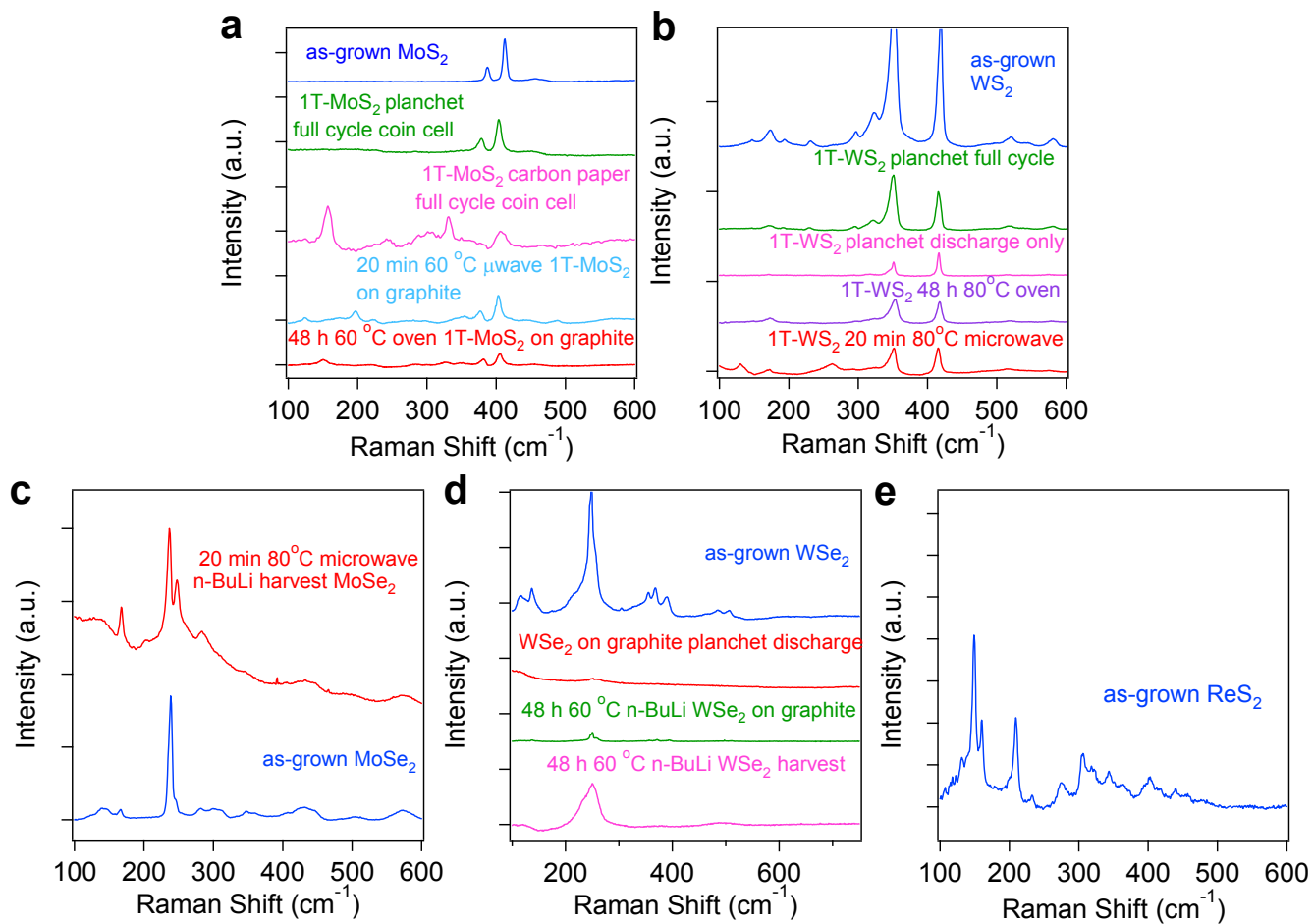


**Figure 4.6.** Raman spectra for the as-grown and exfoliated (where available) nanostructures in (a) MoS<sub>2</sub>, (b) WS<sub>2</sub>, (c) MoSe<sub>2</sub>, (d) WSe<sub>2</sub>, and (e) ReS<sub>2</sub>.

#### 4.4.6 *Electrocatalytic performance of chemically exfoliated MoS<sub>2</sub> nanosheets intercalated with n-butyllithium and LiPF<sub>6</sub>*

1T-MoS<sub>2</sub> nanosheets exfoliated by different means are compared for their electrocatalytic HER performance. Although our recent report on exfoliated MoS<sub>2</sub> nanosheets focuses solely on the intercalation reaction using n-butyllithium solution heated in an oven<sup>6</sup> here we also explore using microwave chemistry to expedite the intercalation (Figure 4.7).<sup>29</sup> Although the harvested MoS<sub>2</sub> exfoliated nanosheets still perform very well, the low-loss electrical address provided by the direct synthesis and exfoliation on graphite substrates is clearly the optimized method (Figure 4.7a, b). The harvesting method also introduces potential variability in the cast films, which may cause help explain its slightly decreased performance. Microwave intercalation for harvested nanosheets produces very competitive HER performance in just a fraction of the time (20 min vs. 48 h). Interestingly, the microwave intercalation for nanosheets synthesized directly on graphite does not perform as well. This likely reflects the need to further optimize the microwave conditions for the future. These trends in HER activity observed in the polarization curves are further reflected by the Nyquist plots (Figure 4.7c) showing the series (all ~4 Ω) and charge transfer resistances (as-grown: 232 Ω; oven harvest: 11 Ω; microwave harvest: 7 Ω; microwave graphite: 43 Ω; oven graphite: 4 Ω). Additionally, we also present the catalytic properties of nanosheets produced from electrochemically controlled Li intercalation reactions carried out in a battery coin cell using LiPF<sub>6</sub> as the lithium source (Figure 4.8). Using a battery analyzer, which applies a constant current density to drive the lithium intercalation, we can more quantitatively control the extent of lithiation, and even electrochemically remove some of the intercalated lithium. Practically, we can never electrochemically remove all of the lithium since the 1T phase is metallic and generally causes the coin cell to short-circuit. The choice of substrate used for the

coin cell intercalation is also important (Figure 4.8a, b). The substrates used for the electrochemical lithiation must conform to the size (15.6 mm diameter) of the 2032 coin cell. The graphite planchet is a larger, commercially available version of the graphite disks normally used in the n-BuLi intercalation while the carbon paper is a very porous (>70%) substrate comprised of graphitic carbon fibers. Although the extent of lithiation may be more complete for the carbon paper thanks to its enhanced solid-electrolyte surface contact, the ultimate performance is likely limited by the large pores of the substrate which present other practical challenges when silver colloid is used to electrically address the electrodes to the RDE tips.

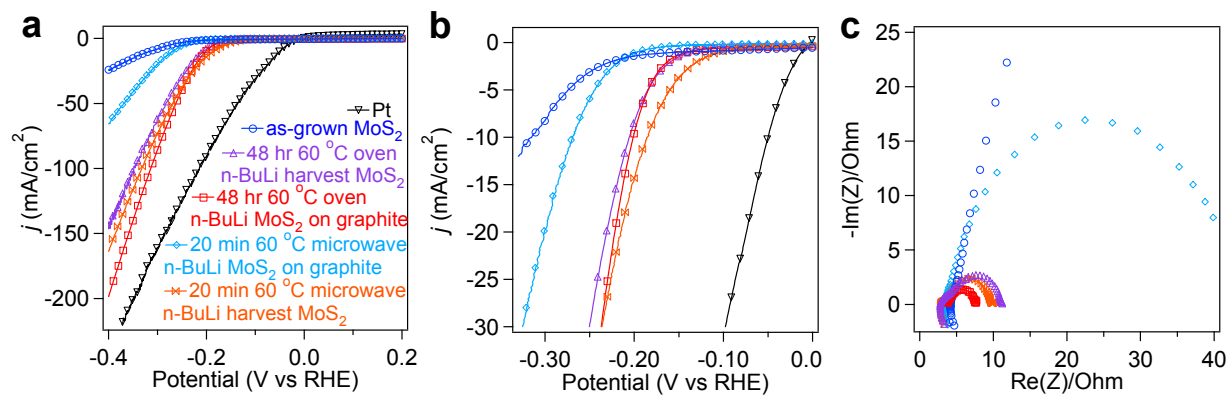


**Figure 4.7.** Polarization curves showing the electrocatalytic performance of 1T-MoS<sub>2</sub> nanosheets produced from different modes of lithium intercalation using n-butyltithium at (a) higher and (b) lower potentials. (c) Nyquist plots from EIS further contrast the differences in the 1T-MoS<sub>2</sub> nanosheets.

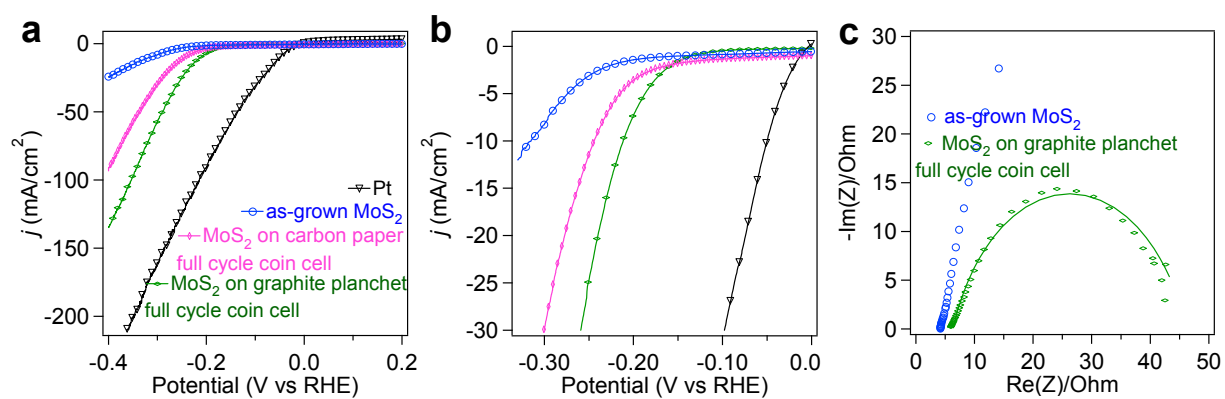


**Figure 4.8.** Polarization curves showing the electrocatalytic performance of 1T-MoS<sub>2</sub> nanosheets produced from coin cell intercalation using LiPF<sub>6</sub> at (a) higher and (b) lower potentials. (c) Nyquist plots from EIS further contrast the differences in the 1T-MoS<sub>2</sub> nanosheets.

#### ***4.4.7 Electrocatalytic performance of chemically exfoliated WS<sub>2</sub> nanosheets intercalated with n-butyllithium and LiPF<sub>6</sub>***

1T-WS<sub>2</sub> nanosheets exfoliated by different means are compared for their electrocatalytic HER performance. Although MoS<sub>2</sub> and WS<sub>2</sub> are very similar compounds, their intercalation chemistry and behavior of exfoliated nanosheets are surprisingly different. The lithium intercalation reaction is much more difficult for WS<sub>2</sub>.<sup>30</sup> To mitigate these issues, we heat the reaction to higher temperatures (80 °C vs. 60 °C for MoS<sub>2</sub>). The most important difference in the behavior of the exfoliated WS<sub>2</sub> nanosheets manifests itself during the reaction with water. The violent generation of H<sub>2</sub> causes the delamination of WS<sub>2</sub> nanostructures from the substrate (graphite, W foil, etc.). Not surprisingly, this results in very poor HER performance (Figure 4.9a, b). We also encounter the same issues after electrochemical intercalation in the battery coin cell using LiPF<sub>6</sub>. Although the delamination of active WS<sub>2</sub> material can be alleviated to some degree by electrochemically removing some lithium and the more gentle reaction of the remaining lithium with alkyl alcohols, the performance is ultimately limited by the unavoidable loss of active material (Figure 4.10a, b). To overcome this issue, we change the procedure completely and we take advantage of such delamination behavior by more easily harvesting the exfoliated nanosheets from the tungsten foils used as the original growth substrate.

We then drop-cast these harvested nanosheets onto graphite disks for electrochemical measurements. Here it is important to note 1T-WS<sub>2</sub> nanosheets achieve 10 mA/cm<sup>2</sup> current densities at the extremely low overpotential of -142 mV vs. RHE (Figure 4.9b). We believe this is the new overpotential benchmark for any non-precious metal HER catalyst. Moreover, we further extend our microwave methodology and show equivalent HER performance can be obtained from nanosheets produced from both microwave-assisted and traditional oven

intercalation methods. These trends in HER activity observed in the polarization curves are further reflected by the Nyquist plots (Figure 4.9c and 4.10c) showing the series (all  $\sim 4 \Omega$ ) and charge transfer resistances (as-grown:  $200 \Omega$ ; oven harvest:  $6 \Omega$ ; microwave harvest:  $5 \Omega$ ; microwave graphite:  $>1000 \Omega$ ; full-cycle battery coin cell:  $410 \Omega$ ; discharge-only battery coin cell:  $422 \Omega$ ).

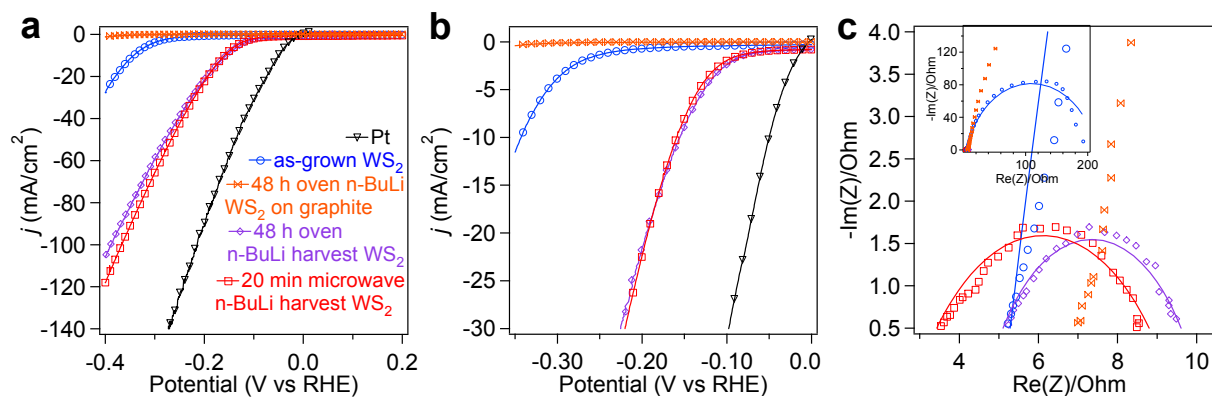


**Figure 4.9.** Polarization curves showing the electrocatalytic performance of 1T-WS<sub>2</sub> nanosheets produced from different modes of lithium intercalation using n-butyllithium at (a) higher and (b) lower potentials. (c) Nyquist plots from EIS further contrast the differences in the 1T-WS<sub>2</sub> nanosheets.

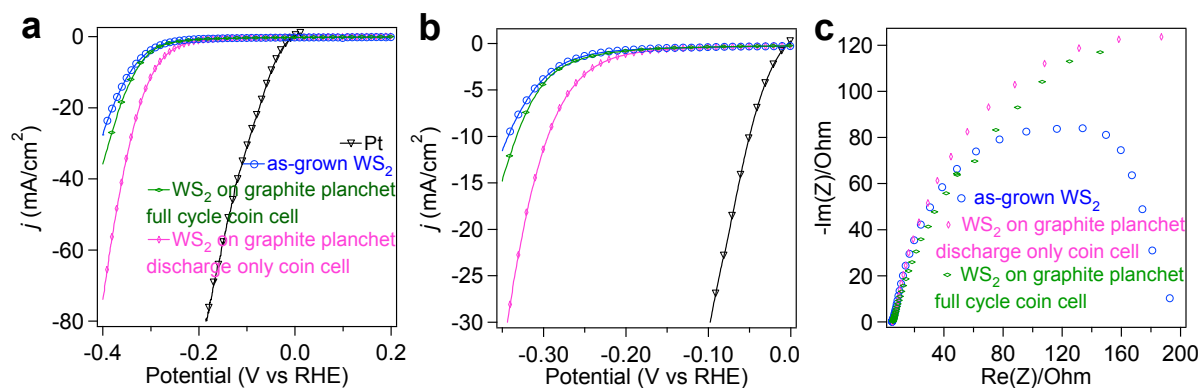


**Figure 4.10.** Polarization curves showing the electrocatalytic performance of 1T-WS<sub>2</sub> nanosheets produced from coin cell intercalation using LiPF<sub>6</sub> at (a) higher and (b) lower potentials. (c) Nyquist plots from EIS further contrast the differences in the 1T-WS<sub>2</sub> nanosheets.

#### ***4.4.8 Electrocatalytic performance of chemically exfoliated MoSe<sub>2</sub> nanosheets intercalated with n-butyllithium***

MoSe<sub>2</sub> nanostructures were grown on molybdenum foils using the synthetic method described above. Interestingly, these nanostructures could not be successfully grown directly on graphite. It is likely that some initial selenization reaction of the Mo foil helps with the subsequent nucleation and growth of the MoSe<sub>2</sub> nanostructures. As-grown MoSe<sub>2</sub> nanostructures harvested from Mo foils and drop-cast onto graphite disks for electrochemical measurements exhibit similar HER activity as compared to 2H-MoS<sub>2</sub> and 2H-WS<sub>2</sub> either grown directly on or drop-cast onto graphite disks. Similar to WS<sub>2</sub> nanostructures, MoSe<sub>2</sub> nanostructures can be easily lithiated using a microwave-assisted intercalation method (80 °C for 20 min) and subsequently reacted with water, thus causing their delamination from the Mo foil growth substrate. The harvested nanosheets are then cast onto graphite disks for catalytic measurements. The exfoliated MoSe<sub>2</sub> nanosheets show significantly enhanced HER activity (Figure 4.11a, b), where significant electrocatalytic current densities ( $j = 10 \text{ mA/cm}^2$ ) is achieved at only  $-203 \text{ mV vs. RHE}$  after correction for  $iR$  losses (c.f. 1T-MoS<sub>2</sub> requires  $-187 \text{ mV vs. RHE}$ ). This also exceeds the performance of other recently published accounts of carefully engineered MoSe<sub>2</sub> for the HER.<sup>21</sup> The corresponding Nyquist plots (Figure 4.11c) confirm the more facile electrode kinetics exhibited by the 1T-MoSe<sub>2</sub> nanosheets ( $R_s = 3 \Omega$ ;  $R_{ct} = 6 \Omega$ ) make it a particularly useful HER catalyst with dramatic improvements over the as-grown MoSe<sub>2</sub> nanostructures ( $R_s = 5 \Omega$ ;  $R_{ct} = 23 \Omega$ ). Tafel analysis of the catalytic behavior (Figure 4.11d) further illustrates the dramatic improvement in HER activity exhibited by the exfoliated MoSe<sub>2</sub> nanosheets ( $63 \text{ mV/decade}$ ) as compared to the as-grown MoSe<sub>2</sub> nanostructures ( $87 \text{ mV/decade}$ ).

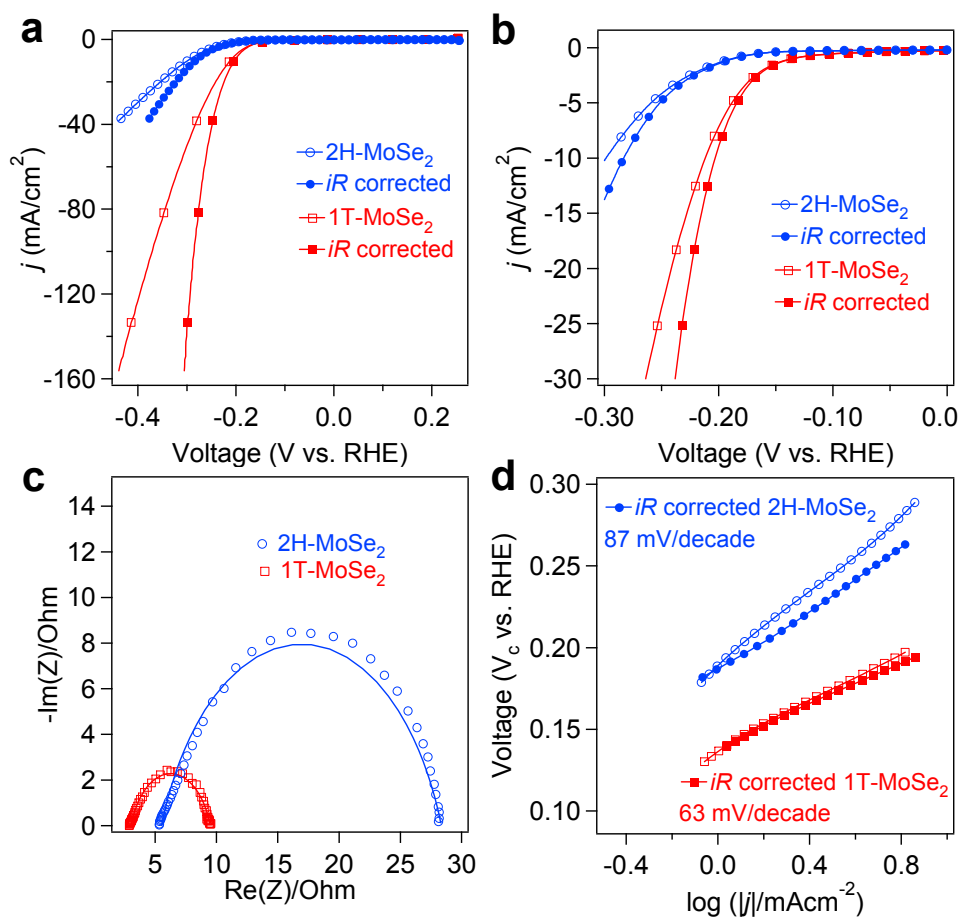


**Figure 4.11.** Polarization curves showing the electrocatalytic performance of exfoliated MoSe<sub>2</sub> nanosheets produced from microwave intercalation using n-butyllithium at (a) higher and (b) lower potentials. (c) Nyquist plots from EIS further confirm the facile electrode kinetics exhibited by the exfoliated MoSe<sub>2</sub> nanosheets. (d) Tafel analysis further illustrates the dramatic improvement in HER activity exhibited by the exfoliated MoSe<sub>2</sub> nanosheets.

#### ***4.4.9 Electrocatalytic performance of chemically exfoliated WSe<sub>2</sub> nanosheets intercalated with n-butyllithium and LiPF<sub>6</sub>***

WSe<sub>2</sub> nanostructures were grown on both graphite substrates and tungsten foils using the synthetic method described above. As-grown WSe<sub>2</sub> nanostructures exhibit similar catalytic HER activity compared to other as-grown MX<sub>2</sub> materials. However, chemical exfoliation of WSe<sub>2</sub> substantially differs from its similar analogs. Although lithium intercalation can be accomplished using oven or microwave-assisted heating methods, the exfoliated WSe<sub>2</sub> is very prone to oxidation. Even during isolation of the exfoliated WSe<sub>2</sub> nanosheets, the initially black product is observed to change color to a red hue. Electrochemical measurements show very poor activity for the HER (Figure 4.12a, b). Battery coin cell intercalation seems to improve the catalytic activity slightly, although these substrates also exhibited visual signs of oxidation. The corresponding Nyquist plots (Figure 4.12c) confirm the WSe<sub>2</sub> nanosheets do not show the facile electrode kinetics exhibited by other exfoliated MX<sub>2</sub> nanosheets (as-grown: 445 Ω; n-BuLi oven graphite: > 1000 Ω; n-BuLi oven harvest: >1000 Ω; battery coin-cell discharge: 817 Ω). It is important to note that some of these EIS data fittings are not consistent with the polarization data (e.g. the best polarization curve is the battery coin cell discharge, but EIS data taken after the LSV data show larger R<sub>ct</sub> than the as-grown WSe<sub>2</sub>). This can be attributed to product decomposition during measurement. Though chemical exfoliation can significantly increase the catalytic activity of MX<sub>2</sub> materials, there is no question that certain materials are still more appropriate for hydrogen evolution than others. WSe<sub>2</sub> is still interesting for many other applications, but HER catalysis is probably not utilizing its properties to the fullest capabilities.

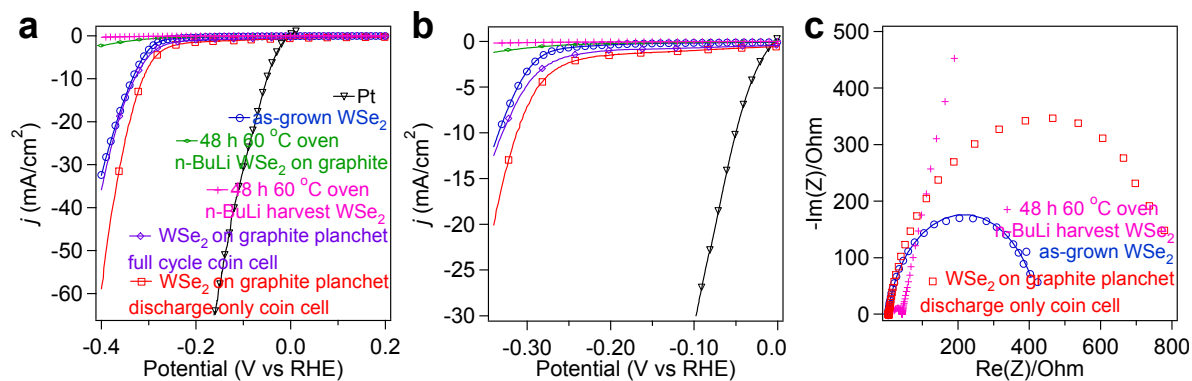


**Figure 4.12.** Polarization curves showing the electrocatalytic performance of exfoliated WSe<sub>2</sub> nanosheets produced from microwave and coin cell intercalation at (a) higher and (b) lower potentials. (c) Nyquist plots from EIS further confirm exfoliated WSe<sub>2</sub> nanosheets are not as catalytically active as other MX<sub>2</sub> compounds.

#### ***4.4.10 Electrocatalytic performance of as-grown ReS<sub>2</sub> nanostructures***

Although rhenium is not an earth-abundant element, ReS<sub>2</sub> is another interesting material from the MX<sub>2</sub> family. The growth of pure ReS<sub>2</sub> nanostructures is actually just a precursor to the eventually goal of doping other earth-abundant MX<sub>2</sub> materials with Re. Doping exfoliated group 6 MX<sub>2</sub> nanosheets with electron-rich impurities atoms (like Re) should further stabilize the metastable 1T phase,<sup>31</sup> even after the lithium atoms are removed by reaction with water. Past studies have shown solubility of Re in MX<sub>2</sub> is only on the order of 0.1 %.<sup>32</sup> Quantification or even qualitative confirmation of nanostructured doping can be very challenging, but since this doping strategy is envisioned to stabilize the 1T phase, the success of our approach will be first judged by this operation criterion. Incorporation of the Re dopant is likely to be most homogeneous if accomplished during the CVD growth. For this reason, the growth of ReS<sub>2</sub> nanostructures was carried out at the typical reaction conditions for MoS<sub>2</sub> and WS<sub>2</sub>. Electrochemical tests on the as-grown ReS<sub>2</sub> nanostructures on graphite show relatively promising HER activity as compared to other as-grown group 6 MX<sub>2</sub> materials (Figure 4.13). Since we intend on using this as a starting point for doping experiments, no further exfoliation experiments were done for ReS<sub>2</sub>.

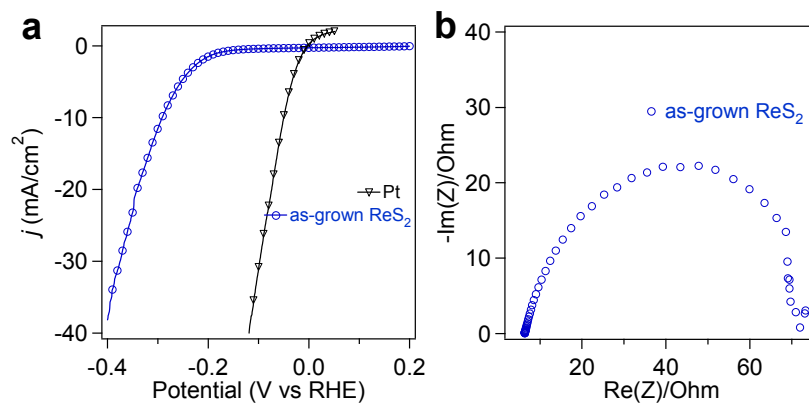


**Figure 4.13.** (a) Polarization curve showing the electrocatalytic performance of as-grown ReS<sub>2</sub> nanostructures. (b) Nyquist plots from EIS reflect the relatively high activity for the HER in as-grown ReS<sub>2</sub> nanostructures.

## 4.5 Conclusions

We have shown the utility of our synthetic method to grow a wide variety of  $\text{MX}_2$  materials having a broad range of potential applications. Moreover, the significant enhancement in catalytic activity exhibited by the chemically exfoliated nanosheets is a general phenomena and not only applicable to  $\text{MoS}_2$ . We use a variety of physical characterization tools including SEM, TEM, Raman, PXRD, CSAFM, XPS, and UPS to show the fundamental differences between the as-grown and chemically exfoliated nanosheets. The 1T- $\text{MX}_2$  materials not only have a higher density of active edge sites, but their catalytic properties have actually been optimized in that the free energy of hydrogen adsorption is likely to be closer to equilibrium. This explains the better performance, especially at lower overpotentials. Beyond these previously unexploited features, we have also laid the fundamental groundwork for the next phase of the project where we target the stabilization of the metastable 1T polymorph by doping with electron-rich impurity atoms. Clearly, a bright future lies ahead for these fundamentally interesting and high-performing earth-abundant  $\text{MX}_2$  materials.

## 4.5 References

- (1) Wang, Q. H.; Kalantar-Zadeh, K.; Kis, A.; Coleman, J. N.; Strano, M. S. *Nat Nano* **2012**, *7*, 699.
- (2) Chhowalla, M.; Shin, H. S.; Eda, G.; Li, L.-J.; Loh, K. P.; Zhang, H. *Nat Chem* **2013**, *5*, 263.
- (3) Koski, K. J.; Cui, Y. *ACS Nano* **2013**, *7*, 3739.
- (4) Georgiou, T.; Jalil, R.; Belle, B. D.; Britnell, L.; Gorbachev, R. V.; Morozov, S. V.; Kim, Y.-J.; Gholinia, A.; Haigh, S. J.; Makarovskiy, O.; Eaves, L.; Ponomarenko, L. A.; Geim, A. K.; Novoselov, K. S.; Mishchenko, A. *Nat Nano* **2013**, *8*, 100.
- (5) Radisavljevic, B.; Radenovic, A.; Brivio, J.; Giacometti, V.; Kis, A. *Nat Nano* **2011**, *6*, 147.
- (6) Lukowski, M. A.; Daniel, A. S.; Meng, F.; Forticaux, A.; Li, L.; Jin, S. *J. Am. Chem. Soc.* **2013**, *135*, 10274.
- (7) Joensen, P.; Frindt, R. F.; Morrison, S. R. *Mater. Res. Bull.* **1986**, *21*, 457.
- (8) Py, M. A.; Haering, R. R. *Can. J. Phys.* **1983**, *61*, 76.
- (9) Chianelli, R. R.; Siadati, M. H.; De la Rosa, M. P.; Berhault, G.; Wilcoxon, J. P.; Bearden, R.; Abrams, B. L. *Cataly Rev* **2006**, *48*, 1.
- (10) Vradman, L.; Landau, M. V.; Herskowitz, M.; Ezersky, V.; Talianker, M.; Nikitenko, S.; Kolytyn, Y.; Gedanken, A. *J. Catal.* **2003**, *213*, 163.
- (11) Jaramillo, T. F.; Jørgensen, K. P.; Bonde, J.; Nielsen, J. H.; Horch, S.; Chorkendorff, I. *Science* **2007**, *317*, 100.
- (12) Merki, D.; Fierro, S.; Vrubel, H.; Hu, X. *Chem Sci* **2011**, *2*, 1262.
- (13) Laursen, A. B.; Kegnaes, S.; Dahl, S.; Chorkendorff, I. *Energ Environ Sci* **2012**, *5*, 5577.

- (14) Voiry, D.; Yamaguchi, H.; Li, J.; Silva, R.; Alves, D. C. B.; Fujita, T.; Chen, M.; Asefa, T.; Shenoy, V. B.; Eda, G.; Chhowalla, M. *Nat. Mater.* **2013**, *advance online publication*.
- (15) Zong, X.; Han, J.; Ma, G.; Yan, H.; Wu, G.; Li, C. *J. Phys. Chem. C* **2011**, *115*, 12202.
- (16) Merki, D.; Hu, X. *Energ Environ Sci* **2011**, *4*, 3878.
- (17) Hinnemann, B.; Moses, P. G.; Bonde, J.; Jørgensen, K. P.; Nielsen, J. H.; Horch, S.; Chorkendorff, I.; Nørskov, J. K. *J. Am. Chem. Soc.* **2005**, *127*, 5308.
- (18) Tenne, R.; Redlich, M. *Chem. Soc. Rev.* **2010**, *39*, 1423.
- (19) Kibsgaard, J.; Chen, Z.; Reinecke, B. N.; Jaramillo, T. F. *Nat. Mater.* **2012**, *11*, 963.
- (20) Chen, Z.; Cummins, D.; Reinecke, B. N.; Clark, E.; Sunkara, M. K.; Jaramillo, T. F. *Nano Lett.* **2011**, *11*, 4168.
- (21) Kong, D.; Wang, H.; Cha, J. J.; Pasta, M.; Koski, K. J.; Yao, J.; Cui, Y. *Nano Lett.* **2013**, *13*, 1341.
- (22) Bierman, M. J.; Lau, Y. K. A.; Kvit, A. V.; Schmitt, A. L.; Jin, S. *Science* **2008**, *320*, 1060.
- (23) Bierman, M. J.; Lau, Y. K. A.; Jin, S. *Nano Lett.* **2007**, *7*, 2907.
- (24) Lau, Y. K. A.; Chernak, D. J.; Bierman, M. J.; Jin, S. *J. Am. Chem. Soc.* **2009**, *131*, 16461.
- (25) Dungey, K. E.; Curtis, M. D.; Penner-Hahn, J. E. *Chem. Mater.* **1998**, *10*, 2152.
- (26) Yang, D.; Frindt, R. F. *J. Phys. Chem. Solids* **1996**, *57*, 1113.
- (27) Jiménez Sandoval, S.; Yang, D.; Frindt, R. F.; Irwin, J. C. *Phys Rev B* **1991**, *44*, 3955.
- (28) Yang, D.; Sandoval, S. J.; Divigalpitiya, W. M. R.; Irwin, J. C.; Frindt, R. F. *Phys Rev B* **1991**, *43*, 12053.
- (29) Benavente, E.; González, G. *Mater. Res. Bull.* **1997**, *32*, 709.

- (30) Miremadi, B. K.; Morrison, S. R. *J. Appl. Phys.* **1988**, *63*, 4970.
- (31) Enyashin, A. N.; Yadgarov, L.; Houben, L.; Popov, I.; Weidenbach, M.; Tenne, R.; Bar-Sadan, M.; Seifert, G. *J. Phys. Chem. C* **2011**, *115*, 24586.
- (32) Marzik, J. V.; Kershaw, R.; Dwight, K.; Wold, A. *J. Solid State Chem.* **1984**, *51*, 170.

## Chapter 5

### Improved Synthesis and Electrical Properties of Si-Doped $\alpha$ -Fe<sub>2</sub>O<sub>3</sub>

#### Nanowires\*

##### 5.1 Abstract

We report an improved method to synthesize  $\alpha$ -Fe<sub>2</sub>O<sub>3</sub> (hematite) nanowires (NWs) via thermal oxidation that significantly reduces reaction time while improving NW density and uniformity. Stress introduced by shot-peening the starting steel foils and the relief of such stress seems to play an important role in promoting uniform one-dimensional growth. Water vapor is also shown to strongly influence both density and morphology of the grown nanostructures. Furthermore, while the as-grown NWs exhibit the high average resistivity ( $4 \times 10^2 \pm 4 \times 10^2 \Omega \cdot \text{m}$ ) associated with undoped hematite, chemical vapor deposition of silane coating these NWs, followed by an annealing step, produces silicon doped  $\alpha$ -Fe<sub>2</sub>O<sub>3</sub> NWs that exhibit a significantly improved average resistivity of  $4 \times 10^{-3} \pm 6 \times 10^{-3} \Omega \cdot \text{m}$ . High resolution electron microscopy, elemental mapping by EDS, and further study of their electrical properties attribute the increased conductivity to lattice doping. These doped hematite NW arrays are promising candidates for potential application as photoanodes in photoelectrochemical solar cells.

---

\* This chapter was originally published in *J. Phys. Chem. C* **115**, 12388. It was prepared in collaboration with S. Jin.

## 5.2 Introduction

Hematite ( $\alpha$ -Fe<sub>2</sub>O<sub>3</sub>) is an intrinsic *n*-type semiconductor with an indirect bandgap of 2.1 eV.<sup>1,2</sup> This theoretically allows the utilization of approximately 40% of the solar spectrum, which is significantly more than other wide band gap semiconductors, such as TiO<sub>2</sub>.<sup>3-7</sup> Combined with its electrochemical stability, low toxicity, wide abundance, and low-cost, hematite is a particularly attractive material for use in photoelectrochemical (PEC) cells.<sup>7-9</sup> Additionally, hematite has also found applications in gas sensing,<sup>10</sup> field emission,<sup>11</sup> heterogeneous catalysis,<sup>12</sup> and as lithium-ion battery electrodes.<sup>13</sup>

However, pure  $\alpha$ -Fe<sub>2</sub>O<sub>3</sub> is a notoriously poor semiconductor, with very high electrical resistivity, sluggish surface kinetics,<sup>2</sup> low mobility, and rapid electron-hole recombination rates,<sup>14</sup> consequently resulting in short carrier diffusion lengths.<sup>15,16</sup> Furthermore, while  $\alpha$ -Fe<sub>2</sub>O<sub>3</sub> is actually one of the few semiconductors with a valence band edge position suitable for oxygen evolution, the conduction band edge of hematite is slightly below the H<sup>+</sup>/H<sub>2</sub> redox potential, thus requiring an applied electrical bias to generate hydrogen.<sup>4</sup> One potential solution to the traditional problems associated with bulk  $\alpha$ -Fe<sub>2</sub>O<sub>3</sub> is to use high aspect ratio nanowires (NWs) as the photoelectrode.<sup>7,17-20</sup> In this configuration, light absorption is allowed to occur along the longer axial dimension of the NW, while carrier separation occurs by diffusion across the much shorter orthogonal radial dimension.<sup>19</sup> This mitigates the problems associated with poor carrier transport in hematite, and this advantage is becoming increasingly clear in recent reports of improved performance in various forms of hematite nanomaterials for PEC application.<sup>2,21-25</sup> It is important to note that even for NW photoelectrodes, precise control over morphology and dopant concentration is still essential to optimizing efficiencies.<sup>26</sup> Furthermore, quantum confinement effects could be used to tune the band edge positions<sup>27</sup> and may allow for the direct

reduction of water without an applied bias. Regardless of the ability to reduce water, hematite remains an interesting material with potential application as a photo-anode in a tandem-cell configuration.<sup>28</sup>

While nanostructures and thin films of hematite doped with a variety of impurity elements have been extensively explored as potential photoanodes,<sup>8,9,22,24,25,29,30</sup> there are much fewer reports using high aspect ratio  $\alpha$ -Fe<sub>2</sub>O<sub>3</sub> NWs for their potential applications in PECs. It was first reported by Takagi in the late 1950s that simply heating pure iron in an oxygen atmosphere resulted in the formation of  $\alpha$ -Fe<sub>2</sub>O<sub>3</sub> whiskers.<sup>31</sup> Although there have been a number of recently published reports on the traditional thermal oxidation of iron foils,<sup>32-34</sup> the NWs are often not uniform or not observed in high yields. Those procedures resulting in denser growth require extremely long oxidation times (tens of hours) and/or harsh oxidizing environments. Recently, there have been interesting new reports using oxidation-related techniques such as resistive heating<sup>35</sup> and combustion-flame synthesis<sup>36</sup> methods that yielded high density, uniform NWs in short reaction times. Furthermore, the as-grown NWs resulting from any of these simple oxidation reactions are not doped, and are therefore expected to be poorly conductive. It has been noted that improved performances in  $\alpha$ -Fe<sub>2</sub>O<sub>3</sub> are observed when the structures are properly doped by subjecting them to a high temperature anneal to encourage dopant incorporation.<sup>24,25</sup> However, very little is known about the electrical properties of  $\alpha$ -Fe<sub>2</sub>O<sub>3</sub> NWs, or their doped counterparts.<sup>37,38</sup> Herein, we report the improved thermal oxidation synthesis of  $\alpha$ -Fe<sub>2</sub>O<sub>3</sub> NWs accomplished by shot-peening the steel foils before oxidation and controlling the water vapor content during the reaction. Moreover, we show a significant increase in observed electrical conductivity after successfully doping the  $\alpha$ -Fe<sub>2</sub>O<sub>3</sub> NWs with silicon. Our doping method is not

limited to  $\alpha$ -Fe<sub>2</sub>O<sub>3</sub> NWs grown by thermal oxidation. In principle, this strategy can be applied to  $\alpha$ -Fe<sub>2</sub>O<sub>3</sub> NWs grown by other routes,<sup>39</sup> and potentially other materials as well.

## 5.3 Experimental Section

### 5.3.1 Preparation of Steel Growth Substrate

0.005" thick sheets of 1008/1010 low carbon steel shim stock obtained from McMaster-Carr are first homogeneously work hardened by shot peening their surface with ~500  $\mu$ m diameter stainless steel beads at ~0.3 MPa for approximately 5 sec, or until the surface appears uniform. These shot peened sheets are cut into approximately 1 cm  $\times$  1 cm foils that are subsequently sanded by hand and etched in concentrated HCl solution for 1 min to remove any native oxide layers. These etched foils are then cleaned by ultrasonication in acetone for 10 minutes, rinsed, and blown dry with N<sub>2</sub>. The resultant foil does not appear polished, but rather dull, and characteristic of freshly exposed metal.

### 5.3.2 Thermal Oxidation Nanowire Synthesis

The  $\alpha$ -Fe<sub>2</sub>O<sub>3</sub> NWs were synthesized in a home-built reactor consisting of a 1" fused silica tube placed in a single-zone tube furnace (Lingberg\ Blue M) equipped with pressure and multiple-gas flow controls. Although the procedure is fairly robust to various reaction parameters, the optimal conditions to form  $\alpha$ -Fe<sub>2</sub>O<sub>3</sub> nanowires are outlined below. The pre-treated foil is placed at the center of the furnace, and the tube is evacuated and flushed three times with argon gas. The tube is heated under vacuum to a temperature of 600 °C. Once the set-point temperature is reached, oxygen gas is flowed at a rate of 150 sccm at a pressure of 760 torr. Once the pressure is stable, hydrogen gas is co-flowed at a rate of 10 sccm; this generates

trace amounts of water vapor *in situ*, which is observed to accelerate the reaction. (Safety warning: heating certain mixtures of H<sub>2</sub> and O<sub>2</sub> can result in an explosion. Consult a combustion reference for the explosion limits of the system.<sup>40</sup>) While NWs are observed to grow within minutes, the reactions are generally terminated after 60 mins by stopping the flow of oxygen and hydrogen, and allowing the tube to cool to room temperature. By tuning reaction parameters such as temperature and the amount of water vapor, a variety of different morphologies can be reproducibly grown.

### ***5.3.3 Silicon Doping of $\alpha$ -Fe<sub>2</sub>O<sub>3</sub> Nanowires***

As-grown  $\alpha$ -Fe<sub>2</sub>O<sub>3</sub> NWs on the steel substrates are placed at the center of a tube furnace in a chemical vapor deposition (CVD) setup. The tube is evacuated and flushed three times with helium gas, and is then heated to 500 °C under a constant inert He flow of 100 sccm with an overall system pressure of 760 torr. Once the set-point temperature is reached, 1 sccm of silane (10% SiH<sub>4</sub> diluted in He) is first introduced and decomposed over the NWs for 30 sec to result in the coating of silicon on the  $\alpha$ -Fe<sub>2</sub>O<sub>3</sub> NWs. Then the reactor is evacuated and flushed with 100 sccm He flow at 760 torr and further annealed at 800 °C for 30 mins to encourage homogeneous lattice doping of silicon.

### ***5.3.4 Nanowire Characterization***

The morphology and density of the as-grown products was examined using scanning electron microscopy (SEM) with a LEO SUPRA 1530 operating at 3 kV. Powder X-ray diffraction (PXRD) on the as-grown substrates was collected using a Siemens STOE diffractometer with Cu K $\alpha$  radiation. High resolution transmission electron microscopy

(HRTEM) and electron diffraction analysis (ED) was done using a Phillips CM200, operating at 200 kV. Elemental maps of the Si-doped  $\alpha$ -Fe<sub>2</sub>O<sub>3</sub> NWs were collected using energy dispersive X-ray spectroscopy (EDS) inside a FEI TITAN aberration corrected scanning transmission electron microscope (STEM) operating at 200 kV. Samples for STEM/EDS analysis were prepared by subjecting the Si-doped  $\alpha$ -Fe<sub>2</sub>O<sub>3</sub> NWs to an additional annealing step in air at 150 °C for 10 mins. These twice annealed NWs are then exposed to a buffered HF solution (Buffered HF Improved, Transene Inc.) for 3 sec before deposition onto a lacey carbon TEM grid for analysis.

### ***5.3.5 Electrical Device Fabrication and Measurements.***

Two-terminal and four-terminal NW devices were fabricated using standard photolithography and electron-beam lithography methods, respectively, to define the electrodes on degenerately doped silicon substrates with a 100 nm thermal oxide. A simple developer solution (1:3 methyl-isobutyl ketone: isopropyl alcohol) is used to dissolve the degraded polymer, and an oxygen plasma descum step (100 W for 30 sec) is employed to remove any residual organics that may otherwise impede ohmic electrical contact. Iron electrodes (150 nm thick) were deposited using electron beam metal evaporation. Prior to electrode deposition, no HF etch step is employed, unless otherwise noted for the specific purpose of determining the origin of the increased electrical conductivity. For the HF etched NW devices, the entire NW is exposed to a buffered HF solution (Buffered HF Improved, Transene Inc.) for 5 sec before the devices are fabricated. Room temperature transport measurements were performed on a probe station with a custom  $I$ - $V$  transport setup.

## 5.4 Results and Discussion

### 5.4.1 Nanowire Growth and Morphology

Our initial thermal oxidation experiments following the general procedures outlined by past reports<sup>33,34,41</sup> showed that while NW growth was always observed, results were inconsistent and the density over the whole substrate was neither sufficient nor uniform (Figure 1A). These experiments were done using steel foils that had not been shot-peened, or intentionally cold-worked in any way. We further noticed that denser NW growth was always seen near the cut edges of the foil (Figure 1A inset), or areas where the foil had been inadvertently scratched. These areas share the common characteristics of having freshly exposed iron and high local concentrations of stress due to the mechanical deformations introduced by cutting or scratching. These observations prompted us to homogeneously cold-work the starting steel foils by shot-peening, which involves shooting small stainless steel balls (shot) at a target (the steel foils). Shot-peening is a common procedure used in engineering to work-harden metal alloys used in mechanically abrasive applications. It has been shown that shot-peening dramatically increases the dislocation density in the target substrates.<sup>42</sup> Along with the brief acid etch and subsequent cleaning steps outlined in the experimental section, these treatments should act to not only ensure consistent surfaces for each reaction, but it may also further expose dislocations and other defects that might be beneficial for NW growth.<sup>43,44</sup> A dramatic improvement in NW density and uniformity is observed for the steel foils having been shot-peened before the oxidation (Figure 1B).

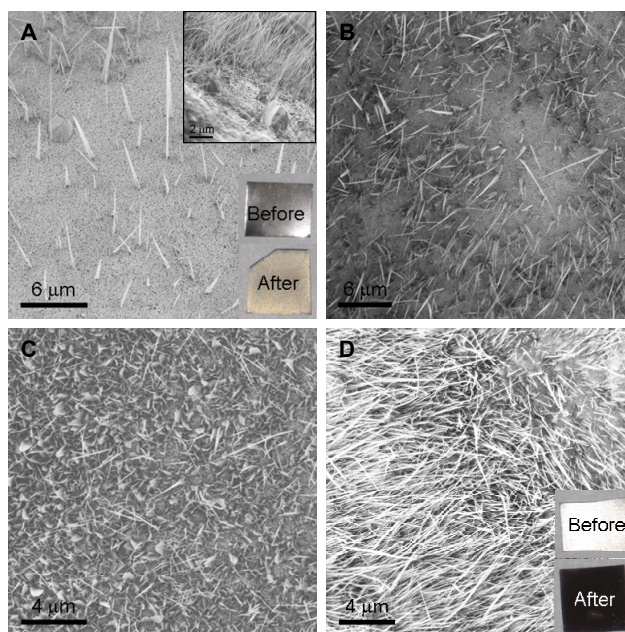


**Figure 5.1.** Representative SEM images of  $\alpha$ -Fe<sub>2</sub>O<sub>3</sub> NWs showing experimental effects of shot peening and water vapor introduction. All substrates were oxidized for 60 mins at 600 °C. A) pristine substrate, no water vapor. Inset SEM image contrasts the NW density observed at the edges of the oxidized foil; B) shot peened substrate, no water vapor; C) pristine substrate, with water vapor present during oxidation (150 sccm O<sub>2</sub> and 10 sccm H<sub>2</sub>); D) shot peened substrate, with water vapor present during oxidation (150 sccm O<sub>2</sub> and 10 sccm H<sub>2</sub>). Insets in panels A and D show the physical appearance of the substrates before and after oxidation.

Along with shot-peening the starting steel foils, the effect of introducing water vapor (by co-flowing oxygen and hydrogen gases) is also investigated. Compared to a dry oxygen environment (no hydrogen gas co-flow), a pristine substrate oxidized in the presence of water vapor (but not shot-peened) exhibits denser growth (Figure 1C). In general, trace amounts of water vapor are observed to accelerate the oxidation by promoting nucleation and nanostructure growth. In addition to providing another oxidizing species, the water vapor generated *in situ* is also expected to catalyze the decomposition of oxygen gas required for the subsequent oxidation of the iron species.<sup>45</sup> The importance of water vapor for quick and dense NW growth has been pointed out in the literature before.<sup>36,46</sup> Simultaneously utilizing shot-peening and introducing trace amounts of water vapor results in a high density of uniform NW growth across the substrate (Figure 1D). The differences in physical appearance between the steel foils are also striking. The pristine foil appears relatively lustrous and typical of average steel, while the shot-peened and acid treated foil appears relatively dull and characteristic of freshly exposed metal. After the standard 60 min oxidation, the untreated foils have only a faintly rusted appearance (Figure 1A inset), whereas the shot-peened foils oxidized in the presence of water vapor have an almost black, deep-red color (Figure 1D inset). Most of the NWs have a length of 5 – 10  $\mu\text{m}$  and diameters of 20 – 100 nm. The density, uniformity, and overall quality of the synthesized NWs are remarkable considering the relatively short amount of time and mild reaction conditions compared to previous thermal oxidation reports which require many hours (10 – 72 hours) and/or harsh oxidizing environments for comparable NW density and uniformity.<sup>32-34</sup>

Varying the reaction temperature and water vapor concentration led to controllable formation of different morphologies (Figure 2). The optimal conditions for NW growth are a balance of oxidation temperature and a relatively moderate concentration of water vapor. Dense

NW growth is observed across the steel foils using oxidation conditions of 150 sccm O<sub>2</sub> and 10 sccm H<sub>2</sub> at 600 °C for approximately 60 mins (Figure 2A). Typically, there are always some small areas showing a distribution of more varied morphologies, including both NWs and plates (Figure 2B). These areas become more common as the substrate size is increased. Blade-like NWs and nanobelts (NBs) are more prevalent as oxidation temperatures are increased to 650 °C, and their formation can be further encouraged by increasing the water vapor concentration; this is accomplished adjusting the gas flows to be 150 sccm O<sub>2</sub> and 15 sccm H<sub>2</sub> (Figure 2C). Plates are observed to primarily form at lower temperatures, with more selective growth in atmospheres rich in water-vapor. Typical reaction conditions that yield plates are 150 sccm O<sub>2</sub> and 15 sccm H<sub>2</sub> at 500 °C (Figure 2D). From these results, it becomes evident that the introduction of water vapor into the oxidation atmosphere not only accelerates the oxidation, but also affects the morphology of the as-grown nanostructures. Sometimes larger and more irregular structures are also observed to form around dense areas of NW growth (Figure 2E), though it is not clear exactly what influences the growth, as their formation is sporadic and not attributable to a single set of reaction conditions. It is likely that these more irregular structures are due to impurities and inhomogeneities present in the low-carbon steel growth substrate. Rough and jagged plates with NWs growing from the tips are observed to sometimes form in oxidation conditions of 150 sccm O<sub>2</sub> and 12 sccm H<sub>2</sub> at 550 °C (Figure 2F). It is emphasized that while these last two morphologies have been observed, their occurrence is irregular and very rare. Overall, the optimal conditions outlined generally yield remarkably uniform and dense nanostructured growth of tunable morphology.

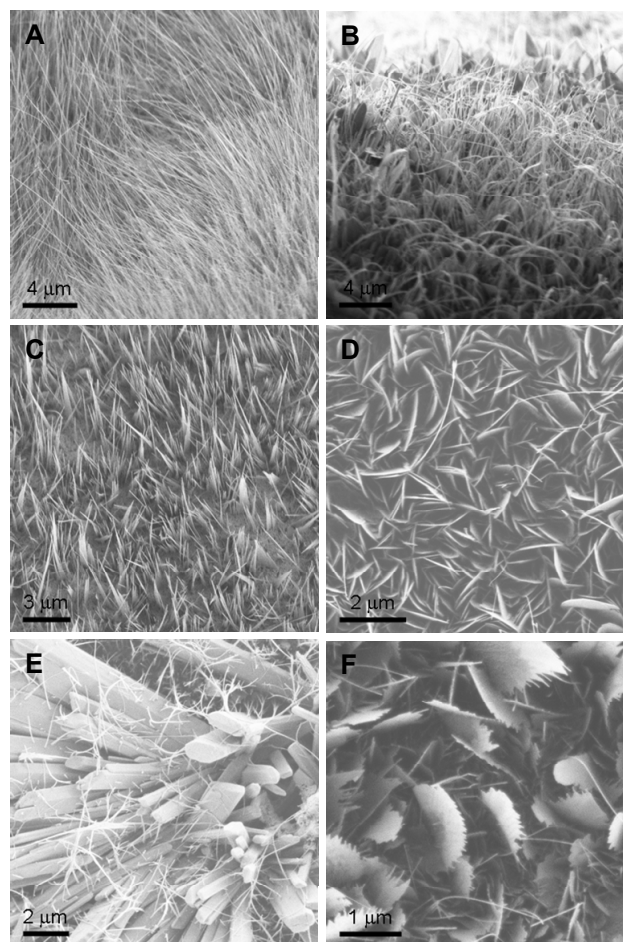


**Figure 5.2.** Representative SEM images showing morphology variations in  $\alpha\text{-Fe}_2\text{O}_3$ . All samples oxidized for 60 mins. A) Dense, uniform NWs; B) Dense overgrowth of NWs with platelets; C) Blade-like nanobelts (NBs); D) Dense, uniform platelets; E) Larger, more irregular structures; F) Rough and jagged platelets with NWs growing from tips.

The traditional oxidation of iron is relatively well understood because of the importance of corrosion problems. Oxidizing iron in air at high temperatures results in the formation of multiple layers of oxide scales; the often non-stoichiometric FeO (wüstite) forms first next to the metal, followed by the formation of Fe<sub>3</sub>O<sub>4</sub> (magnetite) as an intermediate layer, and finally,  $\alpha$ -Fe<sub>2</sub>O<sub>3</sub> (hematite) forms at the solid-vapor interface.<sup>47</sup> Examination of cross-sectional images of the as-grown products reveals the addition of water vapor to the oxidizing atmosphere also increases the growth rates of the underlying oxide scale layers, which is consistent with past reports.<sup>36,45</sup> These scale layers play an important role in the continued growth of the metal oxides, as they act to buffer the outward diffusion of metal atoms to the solid-vapor interface

As for the mechanism for 1-D NW growth, the commonly employed vapor-liquid-solid (VLS)<sup>48</sup> and vapor-solid-solid (VSS)<sup>49</sup> NW growth mechanisms can be dismissed, as the oxidation temperatures are well below the melting points of any iron species present during the reaction (Fe: 1538 °C; FeO: 1370 °C; Fe<sub>3</sub>O<sub>4</sub>: 1538 °C; Fe<sub>2</sub>O<sub>3</sub>: 1566 °C). Moreover, there are no known eutectics, nor is there evidence of catalyst particles present at the tips of any of the nanostructures. Although the details of the growth mechanism are still being investigated, there is a growing consensus that a simple diffusive process is responsible for the mass transport of iron,<sup>34,50</sup> while the dissociation of O<sub>2</sub> provides the majority of the oxygen species. However, diffusion alone fails to explain the anisotropic crystal growth observed in the metal oxide NWs successfully synthesized by thermal oxidation, as not all oxidation conditions result in NWs, or even other different morphologies of nanostructure growth. Fundamentally, there must be some factor that breaks the symmetry of the crystal growth, accounting for the high aspect ratio NWs observed.<sup>44</sup> While the presence of water vapor is observed to accelerate the oxidation process, the empirical improvement in NW density and uniformity observed when the starting foils are

shot-peened seem to suggest that stress and its relief mechanisms play an important role in promoting nanostructure growth. This is supported by the increase in nanostructure density observed in the foils that have been shot-peened (Figure 1) and the morphology control demonstrated by tuning the temperature and water vapor concentration in the oxidizing atmosphere (Figure 2). We continue to work towards developing a coherent model explaining the spontaneous growth of NWs and other morphologies observed in the thermal oxidation of iron. This is likely to be a general mechanism that could be applicable to other metal oxide systems where NWs can be readily synthesized by thermal oxidation.<sup>51</sup>

#### ***5.4.2 Structural and Phase Characterization***

All of the peaks in the observed powder X-ray diffractogram taken on the as-grown substrate (Figure 3) can be indexed to  $\alpha$ -Fe<sub>2</sub>O<sub>3</sub> (PDF card 01-079-0007) and Fe<sub>3</sub>O<sub>4</sub> (PDF card 01-071-6337). Characteristic peaks from hematite (denoted with stars) clearly dominate the experimental pattern. The small Fe<sub>3</sub>O<sub>4</sub> signal can be attributed to the underlying magnetite scale, which is found just below the outer-most hematite layer. Since iron forms multiple oxide scales when oxidized,<sup>47</sup> as discussed above, it is not unreasonable that other phases are detected in the PXRD experiment. Wüstite, the oxide layer formed adjacent to the metal, is not observed in the diffractogram. The underlying oxide scales are observed to have a total thickness of  $\sim 8 \mu\text{m}$  after the standard 60 min oxidation, with the wüstite layer accounting for approximately 90 % of the total thickness.

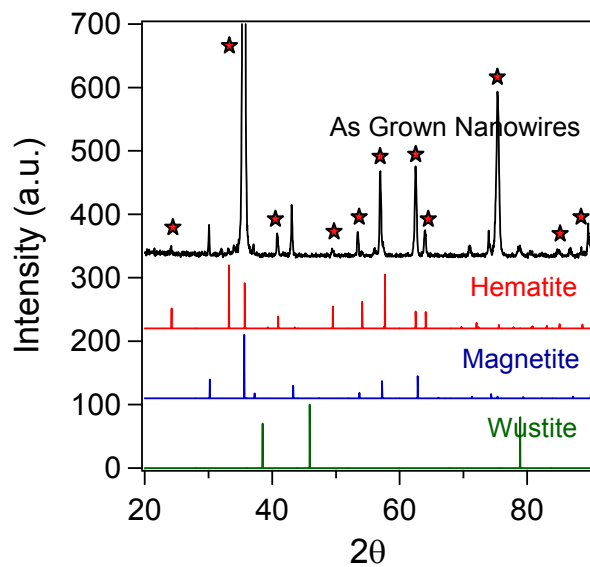


**Figure 5.3.** Powder X-ray diffraction of NWs taken on the as-grown substrates. All peaks can be indexed to  $\alpha$ - $\text{Fe}_2\text{O}_3$  or  $\text{Fe}_3\text{O}_4$ , which is consequently present from the thermal oxidation process.

The crystalline phase of the synthesized NWs is further confirmed using high resolution transmission electron microscopy (HRTEM) and convergent beam electron diffraction (CBED). All NWs examined can be indexed as the  $\alpha$ -Fe<sub>2</sub>O<sub>3</sub> phase. A representative HRTEM image (Figure 4A) shows the continuous, single-crystal lattice of a typical  $\alpha$ -Fe<sub>2</sub>O<sub>3</sub> NW with a diameter of ~50 nm. A higher magnification image (Figure 4B) highlights the 0.251 nm spacing expected for the (110) planes, while the fast Fourier Transform (FFT) (Figure 4C) shows the reciprocal lattice peaks corresponding to the HRTEM image. The FFT is along the  $[\bar{1}11]$  zone axis of  $\alpha$ -Fe<sub>2</sub>O<sub>3</sub>, without possible matches to other iron oxide phases. All NWs examined in the TEM exhibit the same  $[110]$  growth direction, which is consistent with previous reports.<sup>32-34,36</sup>

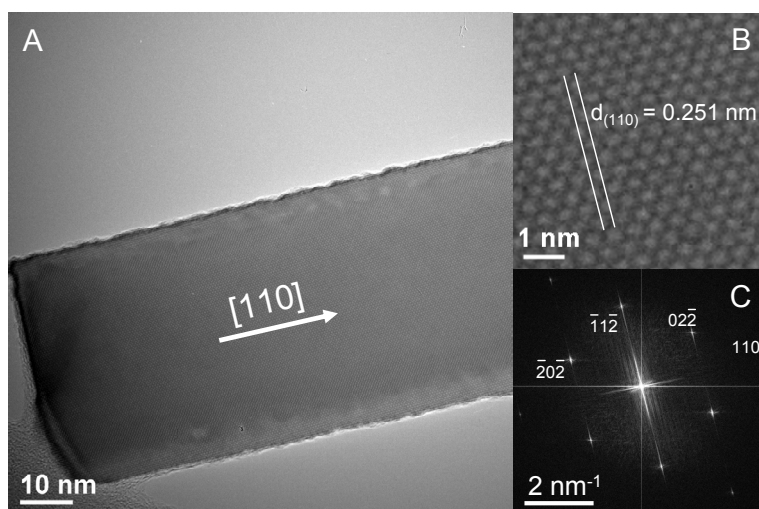


**Figure 5.4.** HRTEM images confirming the  $\alpha$ - $\text{Fe}_2\text{O}_3$  phase of the NWs. A) HRTEM image showing the continuous, single-crystal lattice and the  $[110]$  growth direction of a  $\alpha$ - $\text{Fe}_2\text{O}_3$  NW; B) lattice-resolved HRTEM micrograph highlighting the 0.251 nm spacing of the  $(110)$  planes; C) Indexed fast Fourier Transform of the HRTEM image shown in panel A, along the  $[\bar{1}11]$  zone axis of  $\alpha$ - $\text{Fe}_2\text{O}_3$ .

### 5.4.3 Electrical Properties

Electrical conductivity data from single NW devices are used to assess the efficacy of the doping efforts. Hematite is generally considered a “poor” semiconductor, typically exhibiting a high electrical resistivity of about  $10^3 \Omega \cdot \text{m}$ .<sup>8,14,52</sup> Using the  $I$ - $V$  curve collected at room temperature, and the NW dimensions measured using SEM, the observed resistivity of the single NW can be calculated. Four-probe single NW devices defined by e-beam lithography using the undoped, as-grown  $\alpha$ - $\text{Fe}_2\text{O}_3$  NWs exhibit the poor electrical conductivity generally associated with undoped hematite (Figure 5A). In contrast, the Si-doped NWs show significantly improved conductivity (Figure 5B). Although there is some contact resistance, as shown by the differences between the two- and four-probe measurements on the same NW, such contact resistance does not significantly affect the observed two-probe resistivity of the NW, and it modifies the resistivity of both samples in a consistent way such that its presence does not affect the interpretation of the data. The Si-doped NWs are significantly more electrically conductive. While some four-terminal NW devices defined by e-beam lithography were fabricated and measured, many more two-terminal devices were fabricated using photolithography, affording higher data throughput to provide a large statistical survey of the properties. With 75 independent measurements, the undoped, as-grown  $\alpha$ - $\text{Fe}_2\text{O}_3$  NWs exhibit an average resistivity of  $4 \times 10^2 \Omega \cdot \text{m}$  with a statistical standard deviation of  $\pm 4 \times 10^2 \Omega \cdot \text{m}$ . These results are derived from the histogram showing the distribution of observed resistivities for each type of NW, Si-doped  $\alpha$ - $\text{Fe}_2\text{O}_3$  NWs in red and the undoped, as-grown  $\alpha$ - $\text{Fe}_2\text{O}_3$  NWs in black (Figure 5C). This average resistivity of  $4 \times 10^2 \Omega \cdot \text{m}$  is consistent with past reports of high-purity, undoped thin films and bulk samples of hematite.<sup>8,52,53</sup> In contrast, 55 measurements on the Si-doped  $\alpha$ - $\text{Fe}_2\text{O}_3$  NWs yield an average resistivity of  $4 \times 10^{-3} \Omega \cdot \text{m}$  with a statistical standard deviation of  $\pm 6 \times 10^{-3}$

$\Omega\cdot\text{m}$ , a 5 orders of magnitude improvement in electrical conductivity over the undoped NWs.

Depending on the reported dopant concentration, these Si-doped NWs are on-par or more conductive than other silicon (or analogously, germanium) doped hematite thin films.<sup>8,54,55</sup>

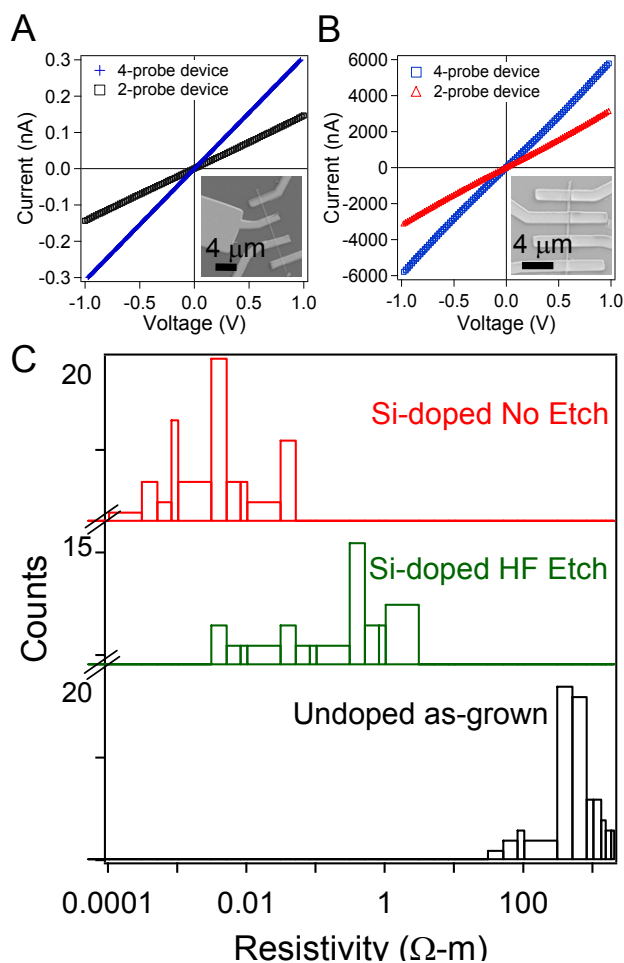


**Figure 5.5.** Electrical properties of as-synthesized and Si-doped  $\alpha$ - $\text{Fe}_2\text{O}_3$  nanowires. A) Representative 2- and 4-probe  $I$ - $V$  curve and SEM image of an undoped, as-grown  $\alpha$ - $\text{Fe}_2\text{O}_3$  NW device; B) Representative 2- and 4-probe  $I$ - $V$  curve and SEM image of a Si-doped  $\alpha$ - $\text{Fe}_2\text{O}_3$  NW device; C) Histogram showing the electrical resistivity data collected for the undoped (75 devices) and Si-doped NWs (55 devices for the Si-doped NWs, and another 52 devices for the HF etched Si-doped NWs).

It is a reasonable concern that the dramatic improvement in conductivity can be attributed to a persistent overcoat of amorphous Si resulting from the CVD process. It is important to note that the as-grown and Si-doped NWs discussed above have not been exposed to any chemical etch during the fabrication process of the devices. To determine the origin of the improved conductivity, some Si-doped  $\alpha$ -Fe<sub>2</sub>O<sub>3</sub> NWs are exposed to a brief buffered HF etch before the device fabrication process. With an estimated etch rate of 80 nm/min, the 5 sec buffered HF exposure will etch through any thin amorphous silicon (or its oxide) coating that would otherwise yield an artificially improved electrical conductivity measurement. It is important to note, however, that the buffered HF will also etch  $\alpha$ -Fe<sub>2</sub>O<sub>3</sub>; given the diameter of the average NW, this dictates that the exposure time must be kept relatively short. Based on 52 measurements, these etched Si-doped  $\alpha$ -Fe<sub>2</sub>O<sub>3</sub> NWs exhibit an average resistivity of  $3 \times 10^{-1}$  with a statistical standard deviation of  $\pm 3 \times 10^{-1}$   $\Omega$ -m, an intermediate value relative to their undoped and Si-doped counterparts. The distribution of these calculated resistivities are also shown in the histogram (Figure 5C). These results suggest that lattice doping is occurring, at least to some extent. If the observed increase in electrical conductivity were due to a simple surface coating of amorphous silicon, a buffered HF etch would have removed this coating, leaving freshly exposed undoped  $\alpha$ -Fe<sub>2</sub>O<sub>3</sub>. Accordingly, the measured electrical resistivity would have more resembled the undoped value ( $\sim 3$  orders of magnitude more resistive than observed). Instead, the intermediate resistivity suggests a probable concentration gradient of silicon within the  $\alpha$ -Fe<sub>2</sub>O<sub>3</sub> NW, i.e. the highest concentration of Si near the surface of the NW and lowest concentration at the core. This likely arises from the nature of the doping process, which starts with a surface coating of silicon that diffuses into the lattice with a high temperature anneal. Recent reports

have shown that substitutional dopants enhancing water-splitting photoactivity require a high annealing temperature ( $\sim 800$  °C) to facilitate their lattice incorporation.<sup>24,25</sup>

Even without the supporting evidence yielded by the NWs exposed to the buffered HF etch, it is very unlikely that a coating comprised of silicon or its oxide ever existed on the outside of the wires. The device fabrication procedure includes a harsh oxygen plasma descum step used to oxidize any residual organics remaining on the NWs after the photoresist has been exposed. This oxygen plasma descum step would have oxidized an amorphous silicon coating to insulating silicon oxide, and resulted in a systematic tunneling barrier to the electrical contact. However, even without a buffered HF etch, ohmic contact is routinely observed (Figure 5B). Considered together, these observations strongly suggest that Si-doping has occurred, and resulted in the observed decrease in electrical resistivity.

The relatively large statistical variations within the data sets are likely attributable to inconsistencies in electrical contact and dopant concentration variability from wire to wire. It is well known that hematite exhibits very anisotropic conductivity, with the close-packed basal planes displaying much higher conductivity.<sup>56</sup> Therefore, depending on the local orientation of the wire and electrode contact, it is plausible that otherwise indistinguishable NWs give rise to large variations in observed electrical resistivity. Despite the large variations within the dataset, the increase in electrical conductivity for the Si-doped  $\alpha$ -Fe<sub>2</sub>O<sub>3</sub> NWs is clear and statistically significant.

#### ***5.4.4 Structural Analysis of Doped NWs***

Careful structural analysis of the doped NW samples further supports that Si-doping of the  $\alpha$ -Fe<sub>2</sub>O<sub>3</sub> NWs has occurred (Figure 6). For  $\alpha$ -Fe<sub>2</sub>O<sub>3</sub> NWs exposed to silane, but never

annealed (Figure 6A, 6B), there is a clear amorphous coating around the entire wire, although they still give weak single-crystal diffraction. The TEM images for NWs exposed to silane and further annealed for 30 mins at 700 °C are shown in Figures 6C and 6D. Although the FFT corresponding to the HRTEM image in panel D (Figure 6C inset) is slightly diffuse because of the real-space disorder, it is uniquely and unequivocally indexed to the  $[010]$  zone axis of  $\alpha$ - $\text{Fe}_2\text{O}_3$ , confirming that the phase of the NWs is preserved through the doping process. It is important to note that we have never observed  $\text{Fe}_3\text{O}_4$  (magnetite) or any other phases during TEM analysis of the as-grown or Si-doped  $\alpha$ - $\text{Fe}_2\text{O}_3$  NWs. Yet there are distinct differences compared to the non-annealed sample. The slightly disordered  $\alpha$ - $\text{Fe}_2\text{O}_3$  lattice can be observed near the surface of the NW, which suggests the substitutional doping of Si atoms within the hematite lattice, and further supports the concentration gradient argument made earlier. The lattice is noticeably less disordered in regions farther inside of the NW, perhaps indicative of the lower concentration of impurity atoms near the core of the  $\alpha$ - $\text{Fe}_2\text{O}_3$  NW. For annealed NWs exposed to the buffered HF solution, the effects of the etching process are easily observed (Figure 6E, 6F). Although the wire is clearly damaged, a continuous lattice is still observed, with some slight disorder noticeable.

It is also a reasonable concern that the increased electrical conductivity is due to the introduction of additional charge carriers in the form of oxygen vacancies. While hematite's *n*-type character is generally attributed to oxygen vacancies, and other past reports have claimed an *n*- to *p*-type transition<sup>37</sup> in  $\alpha$ - $\text{Fe}_2\text{O}_3$  based on specific oxygen vacancy ordering induced by exposure to a reductive atmosphere, we have never observed ordered oxygen vacancies in our TEM experiments. These observations confirm that the buffered HF solution indeed etches the NWs, and also help to explain the relatively large deviations in the electrical properties. The

localized differences in structure observed in these high resolution micrographs are likely attributable to the local variations in dopant concentration, which may result in different etch rates.

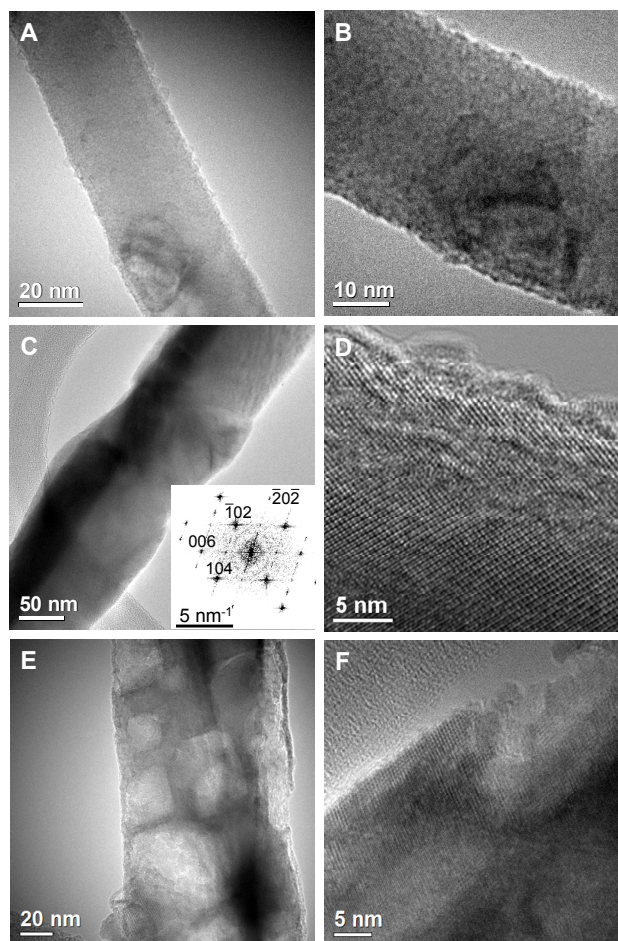


**Figure 5.6.** Representative TEM images showing further evidence of Si-doping in  $\alpha$ - $\text{Fe}_2\text{O}_3$  NWs. A, B)  $\alpha$ - $\text{Fe}_2\text{O}_3$  NWs exposed to 1 sccm  $\text{SiH}_4$  for 30 sec at 500 °C with no further anneal, showing completely amorphous coating; C, D)  $\alpha$ - $\text{Fe}_2\text{O}_3$  NWs exposed to 1 sccm  $\text{SiH}_4$  for 30 sec at 500 °C  $\text{SiH}_4$  treatment followed by 700 °C anneal. The slightly disordered lattice observed is indicative of Si atoms substitutionally doping in the hematite lattice. The inset in panel C is the FFT corresponding to the HRTEM shown in panel D, which is uniquely indexed to the [010] zone axis of  $\alpha$ - $\text{Fe}_2\text{O}_3$ ; E, F)  $\alpha$ - $\text{Fe}_2\text{O}_3$  NWs exposed to 1 sccm  $\text{SiH}_4$  for 30 sec at 500 °C followed by 800 °C anneal, then buffered HF etch for 5 sec. Even though the NW is clearly damaged from the etch, good crystallinity with some disorder is still observed.

#### ***5.4.5 Elemental Mapping of Doped NWs using STEM***

In order to further confirm that the silicon was actually doping into the  $\alpha$ -Fe<sub>2</sub>O<sub>3</sub> NW lattice, we carried elemental mapping experiments using energy dispersive x-ray spectroscopy (EDS) inside the scanning transmission electron microscopy (STEM). Although the electrical measurements suggest that the surface of the doped NW is not amorphous silicon, the Si-doped  $\alpha$ -Fe<sub>2</sub>O<sub>3</sub> NWs are further annealed in air to convert any amorphous silicon on the outside surface of the NW into silicon oxide. These NWs are then subjected to a brief buffered HF etch, which would remove the newly formed silicon oxide. Any silicon detected in the NWs must be located within the  $\alpha$ -Fe<sub>2</sub>O<sub>3</sub> lattice as a dopant. The elemental maps confirm the presence of silicon after the annealing and etching process (Figure 7), and the distribution of silicon seems to be reasonably homogeneous within the  $\alpha$ -Fe<sub>2</sub>O<sub>3</sub> NW. Along with the observed increase in electrical conductivity after the doping process, the confirmed phase identity, the real-space structural evidence, and the EDS elemental maps all firmly establish the conclusion that Si is effectively doped into the  $\alpha$ -Fe<sub>2</sub>O<sub>3</sub> NWs.

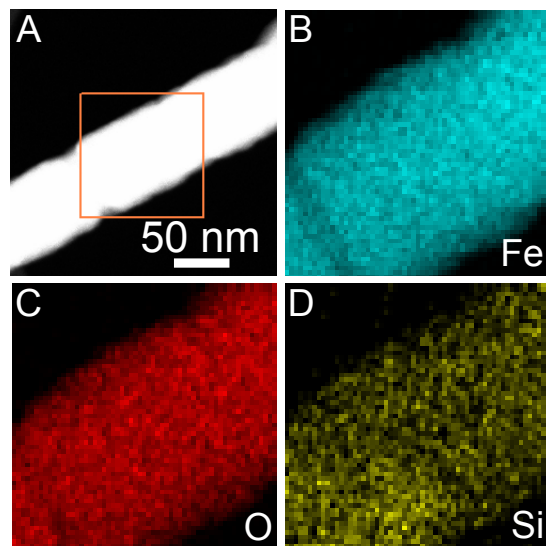


**Figure 5.7.** STEM elemental maps of a Si-doped  $\alpha$ -Fe<sub>2</sub>O<sub>3</sub> NW using the  $L_1$  edges for Fe, O, and Si taken by EDS. A) STEM HAADF image of a Si-doped  $\alpha$ -Fe<sub>2</sub>O<sub>3</sub> NW after additional anneal and buffered HF etch; B–D) EDS elemental maps for iron (B); oxygen (C); and silicon (D).

## 5.5 Conclusion

In summary,  $\alpha$ -Fe<sub>2</sub>O<sub>3</sub> NWs have been synthesized by an improved thermal oxidation method, accomplished by using shot-peened steel foils as the growth substrate and the controlled addition of water vapor to the oxidation conditions. This approach significantly reduces reaction times while improving nanowire density and uniformity. Although the details of the growth mechanism are still under investigation, defects in the steel substrate and stress relief seem to play an important role in promoting nanostructure growth. Exposing the highly resistive undoped, as-grown hematite NWs to silane, followed by an annealing step, produces Si-doped  $\alpha$ -Fe<sub>2</sub>O<sub>3</sub> NWs exhibiting a significantly improved average electrical resistivity of  $4 \times 10^{-3} \pm 6 \times 10^{-3}$   $\Omega$ -m. High resolution electron microscopy, EDS elemental maps, and further study of their electrical properties show the origin of the increased conductivity to be due to lattice doping, and not just a simple amorphous silicon shell surrounding the NW. This doping method is expected to be general and should be widely implementable to  $\alpha$ -Fe<sub>2</sub>O<sub>3</sub> NWs grown by a variety of methods, or even different materials. Such hematite NW arrays with improved conductivity are promising for PEC application. Investigation into using these nanostructures as PEC photoanodes is currently under way.

## 5.6 References

- (1) Gilbert, B.; Frandsen, C.; Maxey, E. R.; Sherman, D. M. *Phys. Rev. B* **2009**, *79*, 035108.
- (2) Sivula, K.; Le Formal, F.; Gratzel, M. *ChemSusChem* **2011**, *4*, 432.
- (3) Gratzel, M. *Nature* **2001**, *414*, 338.
- (4) Bak, T.; Nowotny, J.; Rekas, M.; Sorrell, C. C. *Int. J. Hydrogen Energ.* **2002**, *27*, 991.
- (5) Rajeshwar, K. *J. Appl. Electrochem.* **2007**, *37*, 765.

- (6) Kudo, A.; Miseki, Y. *Chem. Soc. Rev.* **2009**, *38*, 253.
- (7) van de Krol, R.; Liang, Y.; Schoonman, J. *J. Mater. Chem.* **2008**, *18*, 2311.
- (8) Glasscock, J. A.; Barnes, P. R. F.; Plumb, I. C.; Savvides, N. *J. Phys. Chem. C* **2007**, *111*, 16477.
- (9) Cesar, I.; Kay, A.; Gonzalez Martinez, J. A.; Gratzel, M. *J. Am. Chem. Soc.* **2006**, *128*, 4582.
- (10) Hu, X.; Yu, J. C.; Gong, J.; Li, Q.; Li, G. *Adv. Mater.* **2007**, *19*, 2324.
- (11) Zhu, Y. W.; Yu, T.; Sow, C. H.; Liu, Y. J.; Wee, A. T. S.; Xu, X. J.; Lim, C. T.; Thong, J. T. L. *Appl. Phys. Lett.* **2005**, *87*, 023103.
- (12) Weiss, W.; Ranke, W. *Prog. Surf. Sci.* **2002**, *70*, 1.
- (13) Wu, C.; Yin, P.; Zhu, X.; OuYang, C.; Xie, Y. *J. Phys. Chem. B* **2006**, *110*, 17806.
- (14) Morin, F. J. *Phys. Rev. JI - PR* **1951**, *83*, 1005.
- (15) Kennedy, J. H.; Karl W. Frese, J. *J. Electrochem. Soc.* **1978**, *125*, 709.
- (16) Klahr, B. M.; Martinson, A. B. F.; Hamann, T. W. *Langmuir* **2010**, *27*, 461.
- (17) Tian, B.; Zheng, X.; Kempa, T. J.; Fang, Y.; Yu, N.; Yu, G.; Huang, J.; Lieber, C. M. *Nature* **2007**, *449*, 885.
- (18) Bierman, M. J.; Jin, S. *Energy Environ. Sci.* **2009**, *2*, 1050.
- (19) Kayes, B. M.; Atwater, H. A.; Lewis, N. S. *J. Appl. Phys.* **2005**, *97*, 114302.
- (20) Lewis, N. S. *Science* **2007**, *315*, 798.
- (21) Lin, Y.; Zhou, S.; Sheehan, S. W.; Wang, D. *J. Am. Chem. Soc.* **2011**, *133*, 2398.
- (22) Kay, A.; Cesar, I.; Gratzel, M. *J. Am. Chem. Soc.* **2006**, *128*, 15714.
- (23) Zhong, D. K.; Gamelin, D. R. *J. Am. Chem. Soc.* **2010**, *132*, 4202.

- (24) Ling, Y.; Wang, G.; Wheeler, D. A.; Zhang, J. Z.; Li, Y. *Nano Lett.* **2011**, DOI: 10.1021/nl200708y.
- (25) Brilliet, J.; Gratzel, M.; Sivula, K. *Nano Lett.* **2010**, *10*, 4155.
- (26) Hagedorn, K.; Forgacs, C.; Collins, S.; Maldonado, S. *J. Phys. Chem. C* **2010**, *114*, 12010.
- (27) Vayssieres, L.; Sathe, C.; Butorin, S. M.; Shuh, D. K.; Nordgren, J.; Guo, J. *Adv. Mater.* **2005**, *17*, 2320.
- (28) Sivula, K.; Formal, F. L.; Gratzel, M. *Chemistry of Materials* **2009**, *21*, 2862.
- (29) Saremi-Yarahmadi, S.; Wijayantha, K. G. U.; Tahir, A. A.; Vaidhyanathan, B. *The Journal of Physical Chemistry C* **2009**, *113*, 4768.
- (30) Hu, Y.-S.; Kleiman-Shwarsctein, A.; Forman, A. J.; Hazen, D.; Park, J.-N.; McFarland, E. W. *Chem. Mater.* **2008**, *20*, 3803.
- (31) Takagi, R. *J. Phys. Soc. Jpn.* **1957**, *12*, 1212.
- (32) Fu, Y. Y.; Wang, R. M.; Xu, J.; Chen, J.; Yan, A.; Narlikar, A.; Zhang, H. *Chem. Phys. Lett.* **2003**, *379*, 373.
- (33) Hiralal, P.; Unalan, H. E.; Wijayantha, K. G. U.; Kursumovic, A.; Jefferson, D.; MacManus-Driscoll, J. L.; Amaratunga, G. A. J. *Nanotechnology* **2008**, *19*, 455608.
- (34) Wen, X. G.; Wang, S. H.; Ding, Y.; Wang, Z. L.; Yang, S. H. *J. Phys. Chem. B* **2005**, *109*, 215.
- (35) Nasibulin, A.; Rackauskas, S.; Jiang, H.; Tian, Y.; Mudimela, P.; Shandakov, S.; Nasibulina, L.; Jani, S.; Kauppinen, E. *Nano Res.* **2009**, *2*, 373.
- (36) Rao, P. M.; Zheng, X. *Nano Lett.* **2009**, *9*, 3001.

- (37) Lee, Y. C.; Chueh, Y. L.; Hsieh, H.; Chang, M. T.; Chou, L. J.; Wang, Y. W.; Lan, C.; Chen, D.; Kurata, H.; Isoda, S. *Small* **2007**, *3*, 1356.
- (38) Fan, Z.; Wen, X.; Yang, S.; Lu, J. G. *Appl. Phys. Lett.* **2005**, *87*, 013113.
- (39) Meng, F.; Morin, S. A.; Jin, S. *J. Am. Chem. Soc.* **2011**, *133*, 8408-8411
- (40) Kuo, K. K. *Principles of Combustion*; John Wiley & Sons: New York, 1986.
- (41) Tollman, R. L.; Gulbransen, E. A. *J. Electrochem. Soc.* **1967**, *114*, 1227.
- (42) Altenberger, I.; Scholtes, B.; Martin, U.; Oettel, H. *Mat. Sci. Eng. A-Struct.* **1999**, *264*, 1.
- (43) Morin, S. A.; Jin, S. *Nano Lett.* **2010**, *10*, 3459.
- (44) Jin, S.; Bierman, M. J.; Morin, S. A. *J. Phys. Chem. Lett.* **2010**, *1*, 1472.
- (45) Saunders, S. R. J.; Monteiro, M.; Rizzo, F. *Prog. Mater. Sci.* **2008**, *53*, 775.
- (46) Tollman, R. L.; Gulbransen, E. A. *J. Electrochem. Soc.* **1968**, *115*, 770.
- (47) Birks, N. *Introduction to the High Temperature Oxidation of Metals*; University Press: Cambridge, 2006.
- (48) Wagner, R. S.; Ellis, W. C. *Appl. Phys. Lett.* **1964**, *4*, 89.
- (49) Persson, A. I.; Larsson, M. W.; Stenstrom, S.; Ohlsson, B. J.; Samuelson, L.; Wallenberg, L. R. *Nat. Mater.* **2004**, *3*, 677.
- (50) Dong, Z.; Kashkarov, P.; Zhang, H. *Nanoscale* **2010**, *2*, 524.
- (51) Zhang, W.; Yang, S. *Acc. Chem. Res.* **2009**, *42*, 1617.
- (52) Warnes, B. M.; Aplan, F. F.; Simkovich, G. *Solid State Ionics* **1984**, *12*, 271.
- (53) Miller, E. L.; Paluselli, D.; Marsen, B.; Rocheleau, R. E. *Thin Solid Films* **2004**, *466*, 307.
- (54) Sieber, K. D.; Sanchez, C.; Turner, J. E.; Somorjai, G. A. *J. Chem. Soc. Faraday Trans.* **1985**, *81*, 1263.

- (55) Sanchez, H. L.; Steinfink, H.; White, H. S. *J. Solid State Chem.* **1982**, *41*, 90.
- (56) Benjelloun, D.; Bonnet, J.-P.; Doumerc, J.-P.; Launay, J.-C.; Onillon, M.; Hagenmuller, P. *Mater. Chem. Phys.* **1984**, *10*, 503.

**Appendix 1**

**Supporting Information for**

**Chapter 2**

**Enhanced Hydrogen Evolution Catalysis from Chemically**

**Exfoliated Metallic MoS<sub>2</sub> Nanosheets\***

**A1.1 Current-Sensing Atomic Force Microscopy**

We characterized the as-grown and chemically exfoliated MoS<sub>2</sub> nanosheets synthesized directly on highly ordered pyrolytic graphite (HOPG, purchased from Ted Pella) substrates using an Agilent 5500 series AFM with current-sensing capabilities using a symmetric Pt coated tip (30 nm, Miikro Masch) with a force constant of 2.7 N/m. All of the data were collected in the trace, with no significant hysteresis in the data for the retrace, since the current-sensing capability requires the AFM to be operated in contact mode. A clean area of the HOPG substrate was also imaged for comparison. HOPG substrates were used for the AFM imaging experiments because it is smoother and cleaner than the polished graphite disc substrates typically used for the rest of experiments. The topography (Figure A1.1a, e, i), deflection (Figure A1.1b, f, j), and friction (Figure A1.1c, g, k) images were collected in parallel with their corresponding conductivity maps (Figure A1.1d, h, l). All of the data are taken in contact mode with the sample held at a constant +50 mV and all images are 3 μm by 3 μm. The presence of MoS<sub>2</sub> on the HOPG substrates for the as-grown and exfoliated samples is confirmed by the topology,

---

\* This appendix was published online as the supporting information for Lukowski, M. A.; Daniel, A. S.; Meng, F.; Forticaux, A.; Li, L.; Jin, S. *J. Am. Chem. Soc.* **2013**, *135*, 10274. before being adapted here.

deflection, and friction images which show a clear texture especially at the substrate step-edges, in comparison to the smoother HOPG control. Note that the original 3D nanostructures are crumpled to the substrate surface under the contact mode AFM scanning. The striations in the 2H- and 1T-MoS<sub>2</sub> images arise from coming into contact with these structures. The current-sensing maps illustrate the striking difference in material conductivity: the 1T-MoS<sub>2</sub> sample is uniformly conducting, in fact nearly indistinguishable from the bare HOPG control, but the inhomogeneous (speckled) appearance of the 2H sample reflects the more insulating nature of 2H-MoS<sub>2</sub>. This further confirms that the lithium intercalation and exfoliation treatment results in a semiconducting to metallic phase transition, and also there is effective electrical connection between the exfoliated 1T-MoS<sub>2</sub> nanosheets and the conductive substrate.

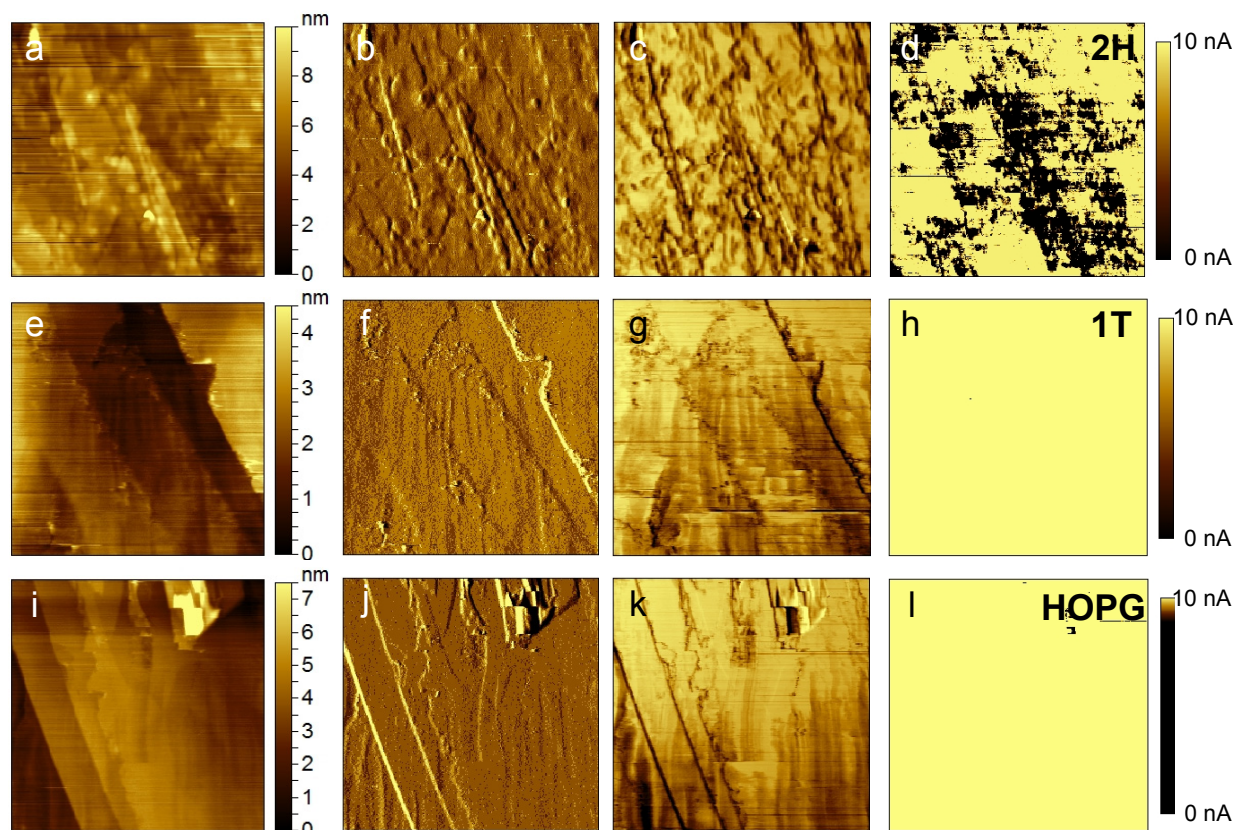


**Figure A1.1.** Topography, deflection, friction, and conductivity AFM maps of (a-d) as-synthesized MoS<sub>2</sub> nanosheets grown on HOPG, (e-h) chemically exfoliated MoS<sub>2</sub> nanosheets on HOPG, and (i-l) clean area of the HOPG control substrate. All images are 3  $\mu\text{m}$  x 3  $\mu\text{m}$ . Deflection and friction images have arbitrary relative scales.

## A1.2 Discussion of the electron diffraction pattern for 1T-MoS<sub>2</sub>

Since 1T-MoS<sub>2</sub> is not found naturally in bulk, the complete crystallographic information for its crystal structure is not available. However, since its structure is described by a single S-Mo-S layer with Mo atoms coordinated by six S atoms in an octahedral environment, its 2D crystal structure can be described using the simple structural basis of:

Mo (0,0); S (1/3, 2/3) and (2/3, 1/3).

Using fundamental diffraction theory, we can calculate the structural factors and predict the diffraction patterns for single layer 1T-MoS<sub>2</sub>. The structure factor of the basis can be written as:

$$S_{hk} = \sum_j f_j \exp\left[-i2\pi\left(h \cdot \vec{a}^* + k \cdot \vec{b}^*\right)\right]$$

$$S_{hk} = f_{Mo} + f_S \exp\left[-i2\pi\left(\frac{1}{3}h + \frac{2}{3}k\right)\right] + f_S \exp\left[-i2\pi\left(\frac{2}{3}h + \frac{1}{3}k\right)\right]$$

$$S_{hk} = f_{Mo} + f_S \left\{ \exp\left[-i2\pi\left(\frac{1}{3}h + \frac{2}{3}k\right)\right] + \exp\left[-i2\pi\left(\frac{2}{3}h + \frac{1}{3}k\right)\right] \right\}$$

Where  $f_{Mo}$  and  $f_S$  are the scattering factors for Mo and S atoms, respectively, and the  $h, k$  are the 2D miller indices.

When  $h = 1, k = 0$ , i.e. for {100} reflections:

$$S_{hk} = f_{Mo} + f_S \left[ \exp\left(\frac{-2}{3}\pi i\right) + \exp\left(\frac{-4}{3}\pi i\right) \right]$$

$$S_{hk} = f_{Mo} - f_S$$

Therefore, we expect to observed weak diffraction intensity for this family of reflections. This explains the absence of the {100} spots in the observed electron diffraction pattern (Figure 3e and also Figure S3b).

In contrast, when  $h = 1, k = 1$ , i.e. for {110} reflections:

$$S_{hk} = f_{Mo} + f_S [\exp(-2\pi i) + \exp(-2\pi i)]$$

$$S_{hk} = f_{Mo} + 2f_S$$

Therefore, we expect to observe strong diffraction intensity for this family of reflections. This explains the prominent  $\{110\}$  reflections in the observed electron diffraction pattern (Figure 3e and Figure S3b). Due to the trigonal prismatic configuration of the  $\text{MoS}_6$  in 2H- $\text{MoS}_2$ , the electron diffraction patterns are different for 2H- $\text{MoS}_2$  but it can be readily predicted using the available crystal structure information, as was done in Figure 1e (displayed again as Figure S3a).

To further illustrate the distinct differences in reciprocal space reflections, we juxtapose the fast Fourier transform (FFT) pattern corresponding to the 2H- $\text{MoS}_2$  nanostructures (Figure S4a, also shown in main text as Figure 1e) and the electron diffraction pattern for the exfoliated 1T- $\text{MoS}_2$  nanosheets (Figure S4b, also shown in main text as Figure 3e) at the same scale of reciprocal spacing. The  $\{100\}$  family of spots in the 2H pattern appear at the expected reciprocal spacing of  $3.56 \text{ nm}^{-1}$ , in contrast, the closest reflections in the 1T pattern appear at  $5.61 \text{ nm}^{-1}$ . The dotted blue circle in the 1T pattern represents the radial distance expected for the  $\{100\}$  spots for 2H- $\text{MoS}_2$ , if they would have appeared. The observed electron diffraction pattern from the exfoliated  $\text{MoS}_2$  nanosheets (Figure S4b) shows the symmetry and lattice expansion expected for the 1T- $\text{MoS}_2$  polymorph.

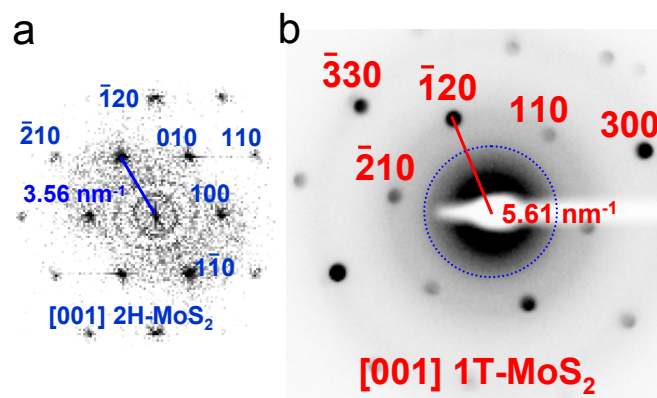


**Figure A1.2.** Comparison of (a) fast Fourier transform pattern indexed unequivocally to 2H-MoS<sub>2</sub> and (b) the observed electron diffraction pattern indexed to 1T-MoS<sub>2</sub>, at the same scale of reciprocal spacing. These are the same patterns shown in the Figure 2.3e and Figure 2.5e in the main text, respectively.

### A1.3 *iR*-corrected catalytic activity

Correcting for Ohmic losses throughout the system, including solution resistance, allows us to better evaluate the true catalytic activity of the 1T-MoS<sub>2</sub> nanosheets and compare it to the catalytic activity displayed by other MoS<sub>2</sub> catalysts. Using the measured current and the series resistance ( $R_s = 3.77 \Omega$  for 1T-MoS<sub>2</sub>;  $R_s = 4.22 \Omega$  for 2H-MoS<sub>2</sub>) determined from electrochemical impedance spectroscopy experiments, we correct the voltages in the polarization measurements and subsequent Tafel analysis for these *iR* losses (Figure A1.3). After the *iR* correction, the 1T-MoS<sub>2</sub> nanosheets achieve an electrocatalytic current density of 10 mA/cm<sup>2</sup> at overpotentials as low as -187 mV vs. RHE (Figure A1.3a, b) and the corresponding Tafel slope is reduced to 43 mV/decade (Figure A1.3c), making 1T-MoS<sub>2</sub> nanosheets one of the most catalytic MoS<sub>2</sub> materials reported.

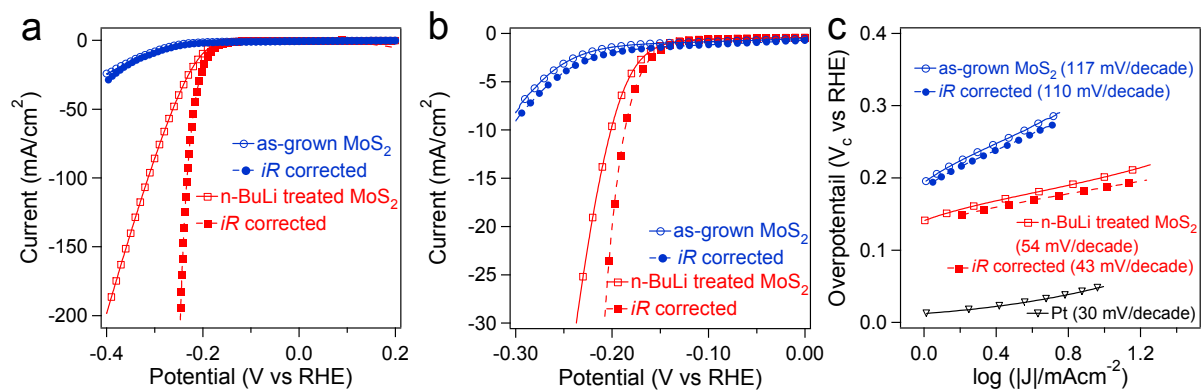


**Figure A1.3.** Polarization curves showing the raw and *iR*-corrected catalytic activity of 1T-MoS<sub>2</sub> nanosheets at (a) higher and (b) lower overpotentials, and (c) the corresponding Tafel plot. The uncorrected (hollow symbols) and corrected (filled symbols) data are also displayed in Figure 2.6 of the main text.

## **A1.4 Capacitance measurements and the relative comparison of active surface areas**

In addition to causing the semiconducting to metallic transition, chemical exfoliation of MoS<sub>2</sub> nanosheets should also proliferate the density of catalytically active edge sites. Using a simple cyclic voltammetry (CV) method, we can determine the double layer capacitance ( $C_{dl}$ ) which is expected to be linearly proportional to the effective active surface area. Determining the exact electrochemical active surface area is difficult due to the unknown capacitive behavior of the MoS<sub>2</sub> electrode and substrate (always graphite), but relative surface areas can be safely estimated. The current response in the cyclic voltammograms for the 1T- and 2H-MoS<sub>2</sub> electrodes in the overpotential region of 0.1–0.2 V vs. RHE should be mostly due to the charging of the double layer (Figure A1.4a, b). The double layer capacitance ( $C_{dl}$ ) is estimated by plotting the  $\Delta J$  ( $J_a - J_c$ ) at 0.15 V vs. RHE against the scan rate (Figure A1.4c). The slopes of these plots are extracted and are equal to the  $C_{dl}$  multiplied by a factor of 2. This analysis shows the electrode of 1T-MoS<sub>2</sub> nanosheets has a more than one order of magnitude larger  $C_{dl}$  (22  $\mu\text{F}$ ) than the electrode of as-grown 2H-MoS<sub>2</sub> nanostructures (1.3  $\mu\text{F}$ ). Assuming that  $C_{dl}$  is directly proportional to the electrochemically active surface area, these results strongly suggest that chemical exfoliation dramatically increases the electrochemical surface area of MoS<sub>2</sub> nanostructures by increasing the density of catalytically active sites for hydrogen evolution.

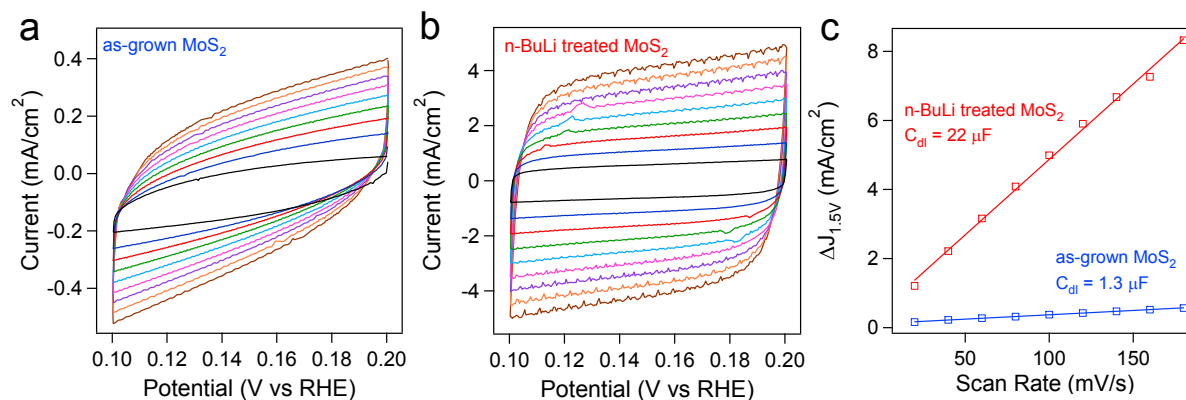


**Figure A1.4.** Cyclic voltammograms collected under different scan rates in the overpotential region of 0.1–0.2 V vs. RHE for the (a) as-grown 2H- and (b) n-BuLi treated and exfoliated 1T-MoS<sub>2</sub> nanostructures. (c) The differences in current density ( $\Delta J = J_a - J_c$ ) at 0.15 V vs. RHE plotted against the scan rate fitted to a linear regression allows for the estimation of  $C_{dl}$ .

**Appendix 2**

**Supporting Information for**

**Chapter 3**

**High-Performance Catalytic Hydrogen Evolution from Metallic**

**WS<sub>2</sub> Nanosheets \***

**A2.1 X-ray photoelectron spectroscopy (XPS)**

We use XPS to illustrate the chemical differences between the as-grown and chemically exfoliated WS<sub>2</sub> nanosheets. These samples were prepared by drop-casting harvested 1T and 2H-WS<sub>2</sub> material directly onto gold coated silicon substrates. Special care was taken to limit their exposure to atmosphere due to concerns of surface oxidation or contamination. Electron transfer from intercalated lithium favours the octahedral coordination of the metal atoms, and therefore causes the structural transition. The electronic structure modifications that accompany the phase change should be detectable by XPS. As shown in the main text, the presence of new chemical species with lower binding energies can be readily attributed to the 1T polymorph. Here, all XPS data are aligned by defining the observed Au4*f* peak as 84.0 eV (Figure A2.1). We also use the C1*s* peak (Figure S3b) to make sure the data are still aligned and the samples are not experiencing differential charging effects that may convolute the data. These data confirm XPS is a powerful tool for the characterization of the 1T polymorph.

---

\* This appendix was originally prepared as the supporting information to be made available online upon publication of the manuscript.

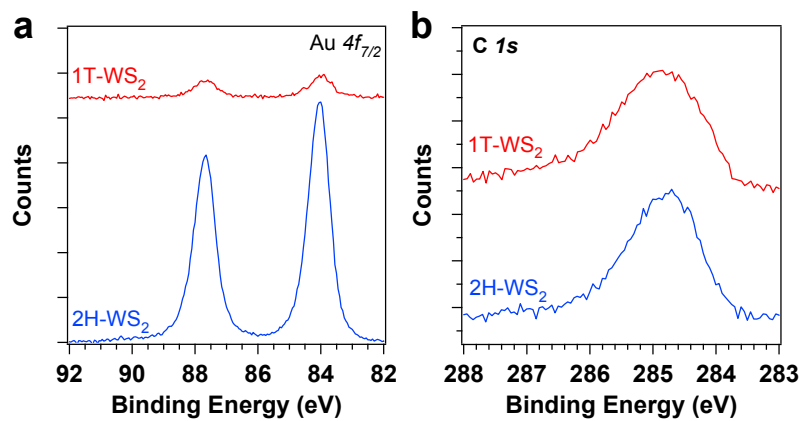


**Figure A2.1.** X-ray photoelectron spectra of the Au $4f$  and C $1s$  edges used for the alignment of all XPS data.

## A2.2 Current-sensing atomic force microscopy (CSAFM)

We characterized the as-grown and chemically exfoliated WS<sub>2</sub> nanosheets cast on evaporated gold (50 nm) film on silicon (100) substrates using an Agilent 5500 series AFM with current-sensing capabilities using a symmetric Pt coated tip (30 nm, Miikro Masch) with a force constant of 2.7 N/m. All of the data are collected in the trace, with no significant hysteresis in the data for the retrace since the current-sensing capability requires the AFM to be operated in contact mode. The topography (Figure A2.2a, e), deflection (Figure A2.2b, f), and friction (Figure A2.2c, g) images were collected in parallel with their corresponding conductivity maps (Figure A2.2d, h). All of the data were taken in contact mode with the sample held at a constant +20 mV and all images are 2 μm by 2 μm. The presence of WS<sub>2</sub> on the substrates for the 2H- and 1T samples is confirmed by the topography, deflection, and friction images which show a clear texture. The current-sensing maps illustrate the striking difference in material conductivity: the 1T-WS<sub>2</sub> sample is uniformly conducting, but the inhomogeneous (speckled) appearance of the 2H sample reflects the more insulating nature of 2H-WS<sub>2</sub>. This further confirms that the lithium intercalation and exfoliation treatment results in a semiconducting to metallic phase transition, and also there is effective electrical connection between the exfoliated metallic 1T-WS<sub>2</sub> nanosheets and the conducting substrate.

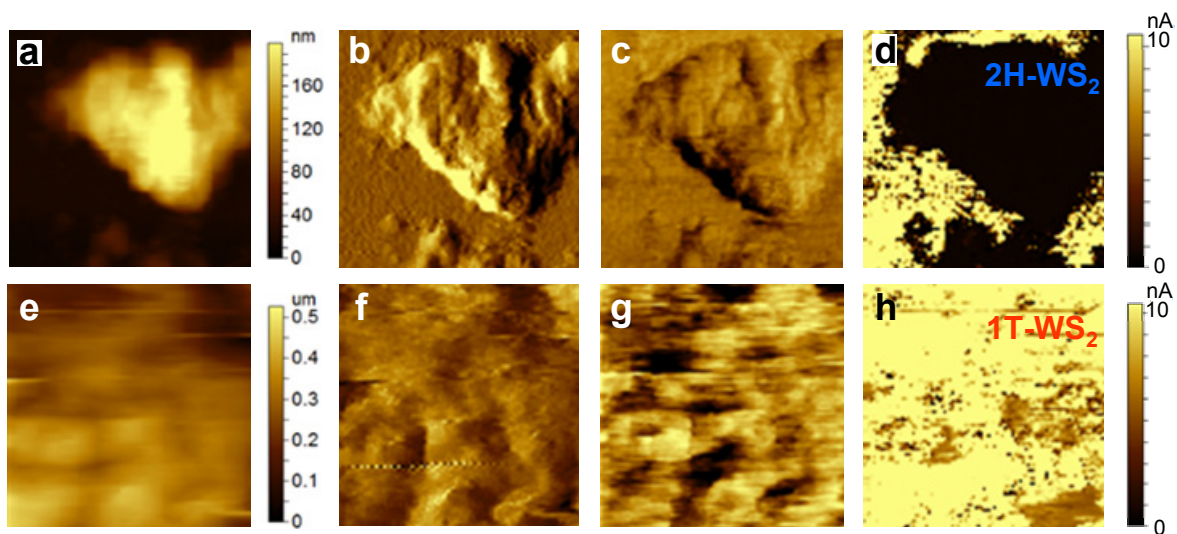


**Figure A2.2.** Topography, deflection, friction, and conductivity AFM maps of (a-d) 2H-WS<sub>2</sub> nanostructures and (e-h) chemically exfoliated WS<sub>2</sub> nanosheets both cast onto evaporated gold on silicon (100) substrates. All images are 2 μm x 2 μm. Deflection and friction images have arbitrary relative scales.

### **A2.3 Chemical exfoliation of WS<sub>2</sub> nanostructures synthesized directly on graphite**

Following the success of our recent 1T-MoS<sub>2</sub> work, we initially tried the analogous approach where we chemically exfoliated as-grown WS<sub>2</sub> nanostructures synthesized directly on graphite disks. However, the violent H<sub>2</sub> generation actually caused the nanosheets to delaminate from the substrate entirely. This was observed visually, and confirmed by their very poor electrocatalytic performance as contrasted with our optimized harvest and dropcast approach which exhibits outstanding catalytic activity (Figure A2.3).

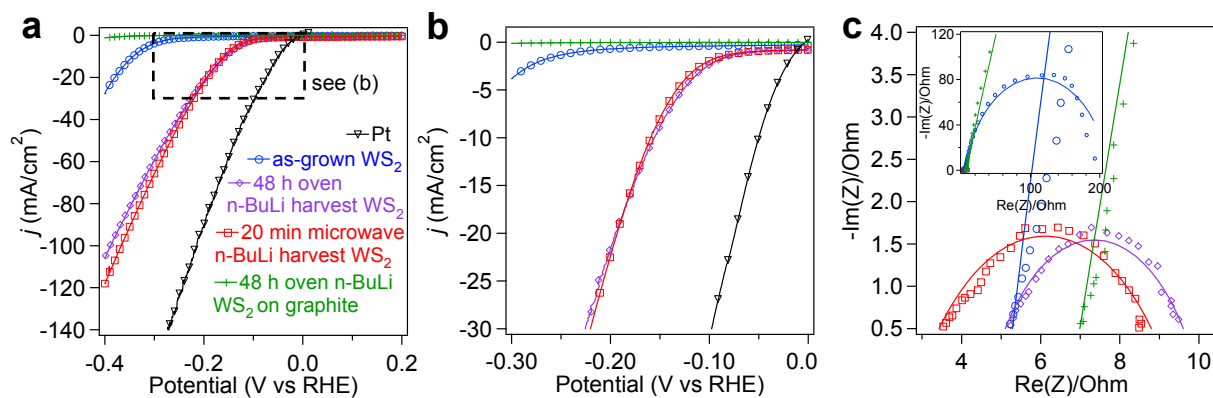


**Figure A2.3.** Polarization curves comparing the (a) overall catalytic activity and (b) performance at lower potentials for chemically exfoliated WS<sub>2</sub> nanosheets obtained by various approaches. (c) Nyquist plots show the corresponding trends in electrode kinetics.

## Appendix 3

# Preliminary Results for the Application of CoS<sub>2</sub> for Hydrogen Evolution Catalysis

### A3.1 Introduction

Although cobalt disulfide (CoS<sub>2</sub>) is not within the layered MX<sub>2</sub> family of materials (actually a pyrite structure-type), it is an interesting earth-abundant material that has been shown to be a promising catalyst for polysulfide reduction.<sup>1</sup> Additionally, CoS<sub>2</sub> has also found applications in the oxygen reduction reaction (ORR),<sup>2</sup> and has been used as a constitutive component of a cobalt-substituted RuS<sub>2</sub> material in a high-throughput study for hydrobromic acid electrolysis.<sup>3</sup> In contrast to other pyrite structure-type materials (e.g. FeS<sub>2</sub>, NiS<sub>2</sub>), CoS<sub>2</sub> is a metallic material, similar to our exfoliated MX<sub>2</sub> nanosheets. At first, CoS<sub>2</sub> was actually envisioned as another metallic nanostructured material used as a high surface-area growth substrate for other more well-known HER catalysts. However, we unexpectedly found promising HER catalytic activity from these simple nanostructured CoS<sub>2</sub> films.

### A3.2 Synthesis of CoS<sub>2</sub> nanostructured thin film (Matt Faber)

100 nm of cobalt metal is evaporated onto cleaned graphite substrates. These thin films were thermally sulfidized in a home-built reactor consisting of a 1 inch fused silica tube equipped with pressure and gas flow controls placed in a single-zone tube furnace. An alumina combustion boat charged with elemental sulfur (99.5 %) was placed just inside tube furnace upstream of the evaporated cobalt on graphite substrates. The reactor was evacuated and flushed

three times with argon before it was back filled to the set-point pressure of 770 Torr under an argon flow of 50 sccm and heated to 500 °C. Reactions lasted 1 h to ensure complete sulfidation, and then the furnace was cooled naturally under argon flow.

### **A3.3 Structural characterization methods**

SEM was performed using a LEO Supra55 VP microscope operating at 3 kV. PXRD data were collected using a Bruker D8 advanced powder diffractometer (Cu K $\alpha$  radiation) on as-sulfidized thin films on their growth substrates (graphite or glass). Background from the glass substrate was subtracted where appropriate. Raman spectra were taken using a Thermo Scientific DXR confocal Raman microscope using a 532 nm excitation laser.

### **A3.4 Electrochemical characterization methods**

Electrochemical measurements were performed using a rotating disk electrode (BASi, RDE-2) in a three-electrode electrochemical cell using a Bio-Logic SP-200 potentiostat. All measurements were performed in 50 mL of 0.5 M H<sub>2</sub>SO<sub>4(aq)</sub> electrolyte (pH = 0.16) prepared using 18 M $\Omega$  deionized water purged with H<sub>2</sub> gas (99.999%), using CoS<sub>2</sub> on graphite disks as the working electrode, a graphite rod as a counter electrode, and a saturated calomel (SCE) reference electrode (CH Instruments). The CoS<sub>2</sub> on graphite disks were mounted on top of the embedded glassy carbon RDE electrodes using colloidal silver paint (Ted Pella). As a comparison, a standard Pt disc (4 mm diameter, Ted Pella) was mounted to the glassy carbon RDE electrode using the same method. The reversible hydrogen electrode (RHE) was calibrated using platinum as both working and counter electrodes to +0.260 V vs. the SCE reference. The performance of the hydrogen evolution catalyst is measured using linear sweep voltammetry beginning at +0.30

V and ending at  $-0.45$  V vs. RHE with a scan rate of  $3$  mV/s when the working electrode is rotated at  $2000$  rpm. Electrochemical impedance spectroscopy was performed when the working electrode was biased at a constant  $-0.250$  V vs. RHE while sweeping the frequency from  $5$  MHz to  $10$  mHz with a  $10$  mV AC dither. The impedance data were fit to a simplified Randles circuit to extract the series and charge transfer resistances.

### **A3.5 Characterization of CoS<sub>2</sub> nanostructured thin film**

Although the CoS<sub>2</sub> films are not synthesized from a true vapor phase reaction by CVD, the nanostructured film is highly conductive and can be mechanically robust.<sup>1</sup> The thickness of the evaporated cobalt, and therefore the final thickness of the CoS<sub>2</sub> film, is an important parameter that contributes to its mechanical stability, especially with respect to its operation as a HER catalyst. SEM imaging shows a uniform nanostructured film with grain sizes on the order of  $20$  nm (Figure S3.1a). The material appears to be phase-pure by PXRD (Figure S3.2b), which shows no evidence of lower-sulfides, un-reacted cobalt, or significant oxide. Furthermore, only the characteristic peaks at  $287$ ,  $389$ , and  $410$  cm<sup>-1</sup> are observed in the Raman spectrum (Figure 3.1c).

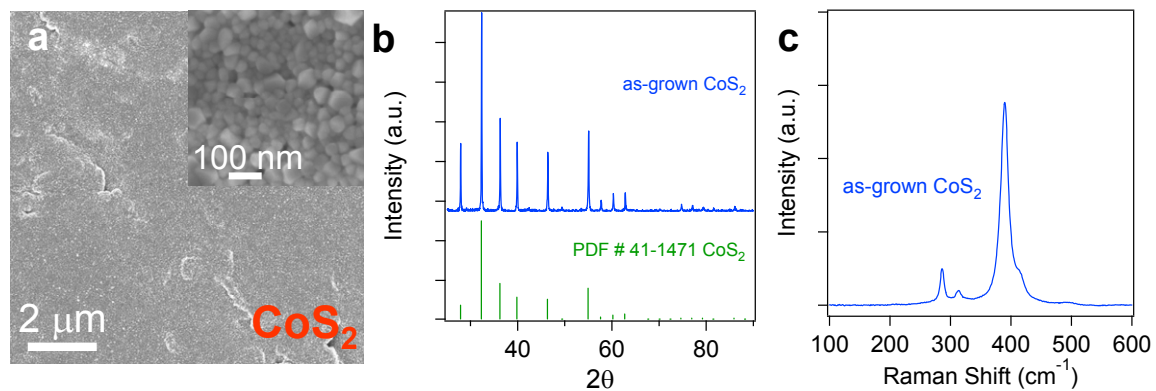


**Figure S3.1.** (a) SEM image of the as-sulfidized  $\text{CoS}_2$  film on graphite exhibiting approximately 20 nm grain size. Phase purity of the material is illustrated by (b) PXRD and (c) Raman spectroscopy.

### A3.6 Electrocatalytic performance of CoS<sub>2</sub> nanostructured thin film

Initially, we used these CoS<sub>2</sub> nanostructured films as a substrate for the CVD growth MoS<sub>2</sub>, but there was only marginal improvement in the HER activity of the heterostructure material as compared to pure 2H-MoS<sub>2</sub> grown directly on graphite. However, the control experiments using CoS<sub>2</sub> only showed unexpectedly promising activity for the HER (Figure S3.2a, b). It is important to note that although the approximately 100 nm thick CoS<sub>2</sub> films shown here were mostly mechanically stable, other experiments (not shown here) using a thin 25 nm layer of cobalt delaminated from the graphite substrate during the violent evolution of hydrogen. The nanostructured film is likely to be somewhat porous, which likely contributes to the loss of material due to hydrogen evolution within the film. The performance from the as-synthesized CoS<sub>2</sub> film is actually better than any of the as-grown MX<sub>2</sub> materials, with meaningful electrocatalytic current densities ( $j = 10 \text{ mA/cm}^2$ ) reached at  $-250 \text{ mV vs. RHE}$  (c.f. 2H-MoS<sub>2</sub> requires  $-320 \text{ mV vs. RHE}$ ). The Nyquist plots (Figure S3.2c) confirm the excellent electrode kinetics exhibited by the nanostructured CoS<sub>2</sub> film ( $R_s = 6 \text{ } \Omega$ ;  $R_{ct} = 11 \text{ } \Omega$ ). This is especially interesting and promising, as the HER activity of CoS<sub>2</sub> has not been well characterized.

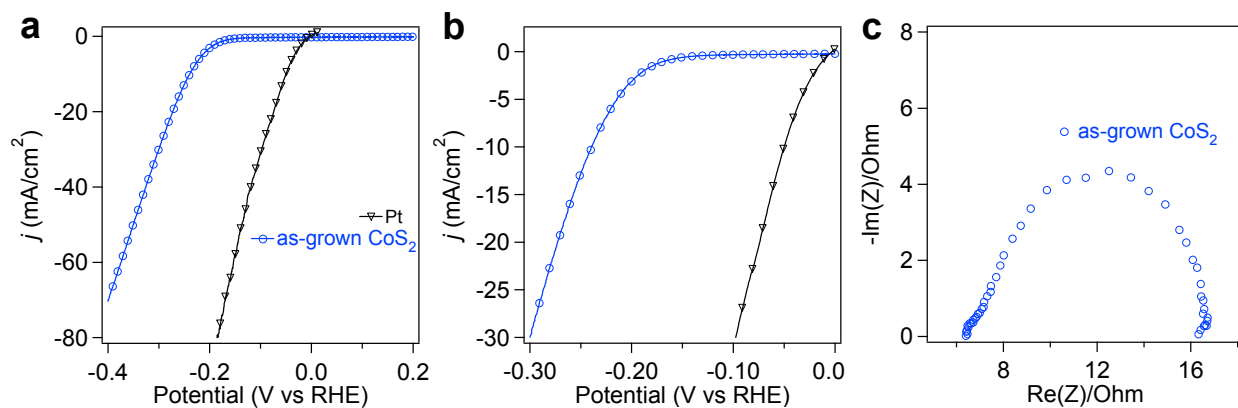


**Figure S3.2.** Polarization curves showing the electrocatalytic performance of as-synthesized CoS<sub>2</sub> nanostructured film at (a) higher and (b) lower potentials. (c) Nyquist plots from EIS reflect the relatively high activity for the HER in as-synthesized CoS<sub>2</sub> nanostructured film.

### A3.7 Future work and preliminary conclusions

To further optimize this system, we are currently exploring a number of synthetic methods to further enhance the surface area, and additionally, we are also investigating other metal pyrite materials, such as NiS<sub>2</sub>, for the electrocatalytic HER. In conclusion, we show unexpected but promising catalytic HER activity from a nanostructured CoS<sub>2</sub> thin film, opening a whole new class of materials for the next generation of earth-abundant catalysts.

### A3.8 References

- (1) Faber, M. S.; Park, K.; Cabán-Acevedo, M.; Santra, P. K.; Jin, S. *J. Phys. Chem. Lett.* **2013**, *4*, 1843.
- (2) Jirkovský, J. S.; Björling, A.; Ahlberg, E. *J. Phys. Chem. C* **2012**, *116*, 24436.
- (3) Ivanovskaya, A.; Singh, N.; Liu, R.-F.; Kreutzer, H.; Baltrusaitis, J.; Van Nguyen, T.; Metiu, H.; McFarland, E. *Langmuir* **2012**, *29*, 480.